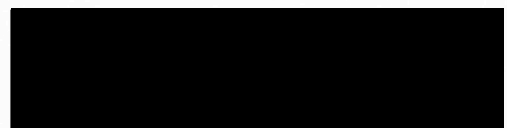


OU
THESIS
CAS
Cop. 1

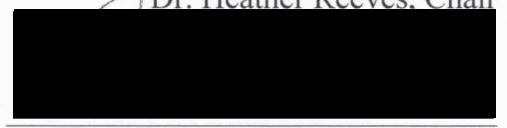
A COMPARISON OF MICROPHYSICAL PARAMETERIZATION SENSITIVITIES
IN THREE COMMA-HEAD SNOW EVENTS AND EVALUATION OF SCHEME
SOLUTIONS WITH PIREPS

A THESIS APPROVED FOR THE
SCHOOL OF METEOROLOGY

BY



Dr. Heather Reeves, Chair



Dr. David Parsons



Dr. Steven Cavallo

UNIVERSITY OF OKLAHOMA

GRADUATE COLLEGE

A COMPARISON OF MICROPHYSICAL PARAMETERIZATION SENSITIVITIES
IN THREE COMMA-HEAD SNOW EVENTS AND EVALUATION OF SCHEME
SOLUTIONS WITH PIREPS

A THESIS

SUBMITTED TO THE GRADUATE FACULTY

in partial fulfillment of the requirements for the

Degree of

MASTER OF SCIENCE IN METEOROLOGY

By

KRISTEN CASSADY

Norman, Oklahoma

2013

Acknowledgements

Since the beginning of my graduate studies, I have developed many relationships, both personal and professional, which have enhanced my growth and development, both as a student, and as a person. Firstly, I would like to thank Dr. Heather D. Reeves, my advisor, for all of her guidance, support, and enthusiasm for my work and my success. She has been a tremendous mentor and has spent countless hours guiding me and pushing me towards a goal of excellence. Through her guidance, I have learned a set of indispensable skills that I can use both now, and in the future. I also extend my gratitude to Dr. David Parsons and Dr. Steven Cavallo for their guidance, support, time, and effort. Both Dr. Parsons and Dr. Cavallo have provided encouragement and enthusiasm for my work since day one, and have been great mentors to me. I would also like to thank Dr. Edward Mansell and Dr. Gregory Thompson for their help and willingness to answer any inquiries regarding the experiments presented in this paper.

Secondly, I would like to thank my family. My mom, dad, and twin brother Andy have supported my decision to pursue a meteorology career since I was a kid. They have dealt with me hogging the TV, which is usually set to the weather channel, and have dragged me inside from both raging thunderstorms and snowstorms. But most importantly, each member of my family has dedicated numerous hours and a great deal of effort to my wellbeing and my success. They are the reason that I have been able to continue my studies, even from 900 miles away. They are the reason this paper has been possible.

I have developed many close relationships over my time thus far at OU. I would also like to thank Ariel Cohen, Yunsung Hwang, Eric Jacobsen, and Carly Kovacik for their support, and most importantly, their friendship. It is their friendship that has made Norman a second home for me.

I consider myself to be the most blessed person in the world. I have always had a team of friends and family surrounding me, constantly offering their support and guidance. My success is their success. I wouldn't have made it to where I am today without all of you!

Contents

Acknowledgements	iv.
List of Tables	vii.
List of Figures	viii.
Abstract	xiii.
1 Introduction	1
1.1 Motivation for Research	1
1.2 Overview of Control Parameters and Forecasting of Icing	3
1.3 Icing in Comma-Head Snowstorms.....	7
1.4 Research Objectives	9
2 Background	11
2.1 Precipitation Generation in Comma-Head Portions of Mid-Latitude Storms.....	11
2.1.1 Formation of Comma-Head Snowstorms	11
2.1.2 Cloud and Precipitation Patterns in the Comma-Head Region.....	14
2.2 Forecasting of SLW.....	16
2.3 Icing Reports for Each Event	20
2.4 Synoptic and Mesoscale Overview	25
3 Comparison of Partially- and Fully-Double Moment Microphysical Parameterizations and Evaluation With PIREPs	27
3.1 Experimental Design.....	27
3.2 Control Experiments and Comparison of Partially- and Fully-Double Moment Forecasts	31
3.3 Evaluation of Parameterization Forecasts with PIREPs.....	37
4 Thompson Microphysical Parameterization Sensitivity Tests	49
4.1 Thompson Microphysics Processes.....	49
4.2 Collection Efficiency of Snow From Cloud Water	52
4.3 Snow Parameter Sensitivities	54
4.3.1 Effective Snow Density	54
4.3.2 Snow Sphericity	56
4.3.3 Capacitance of Spheres and Plates/Aggregates	58
4.4 Prescribed Cloud Droplet Concentration.....	60
5 Conclusions	65

Figures	70
Reference List	121

List of Tables

2.1	PIREPs breakdown per vertical layer for each event investigated. The highest percentage of icing reports occurred with the 6 Feb 2010 case, while the lowest percentage of icing reports occurred with the 15 Feb 2010 event.....	24
3.1	Bulk microphysical parameterization descriptions for the schemes investigated in this paper. Vapor is denoted by v , cloud water by c , ice by i , snow by s , rain by r , graupel by g , and hail by h . [Note that TSON and MORR are only partially-double moment scheme, while MY and NSSL are all fully-double moment schemes]	30
3.2	Skill Score tally format. A scheme forecast maximum q_c value above set threshold indicates a “yes” forecast, while a scheme forecast maximum q_c value that fails to meet such threshold indicates a “no” forecast. The observed statistics are the individual PIREPs reports, which are assumed to be truth.....	39
3.3	Number of hits, misses, false alarms (FAs), and correct nulls (CNs) for each event. For 6 Feb, there are 224 reports between 0000 UTC and 0600 UTC, which include flight paths across central and southern Illinois, central and southern Indiana, and central and southern Ohio. For 26 Jan, there are 72 reports between 0000 UTC and 0600 UTC, which include flight paths across northern Mississippi, western and central Tennessee, and western and central Kentucky. For 15 Feb, there are 250 reports between 1200 UTC and 1800 UTC, which include flight paths across central and southern Indiana, central and southern Ohio, and northern Kentucky	40
3.4	Confusion matrix normalized to total number of reports per case. Each number represents the percentage of forecasts per report	42
3.5	Skill statistics for each event and microphysical parameterization. A perfect POD score, and accuracy score is 1, while an “unbiased” forecast also receives a score of 1. Bias scores over 1 indicate an over-forecast, while scores below 1 indicate an under-forecast. A perfect FAR score is 0	43
3.6	Skill Scores for 6-h periods for each event and each microphysical parameterization scheme. For each skill score considered, a score of 0 indicates a forecast that is equal to a reference forecast, while a score of 1 indicates a perfect forecast. However, Heidke’s skill and TSS scores of -1, and a GSS score of -1/3 indicates a poor forecast	47
4.1	Changes in summations of mixing ratios across comma-head precipitation systems for each of the 3 events considered, compared to CTRL.....	63

List of Figures

- 1.1 Conveyor belts associated with mid-latitude extratropical cyclogenesis. [Taken from Moore et al. (2004)]. The three conveyor belts identified here (warm, cold, dry) have long been established during cyclogenesis, using relative-wind analysis (Harold 1973; Carlson 1980; Danielsen 1964). A conveyor belt refers specifically to an ensemble of parcels with similar thermodynamic characteristics and narrow ranges of potential temperature and wet-bulb temperatures (Browning 1990; Carlson 1991) 70
- 2.1 Cyclone model showing the warm conveyor belt (red), cold conveyor belt (blue), and dry airstream (yellow): (a) before and (b) after occlusion. [Taken from Schultz and Vaughan (2011)]. Conveyor belt schematic stems from the findings by Danielsen (1964), Harold (1973), and Carlson (1980), who first identified conveyor belts as ensembles of parcels with similar thermodynamic characteristics 71
- 2.2 GOES infrared satellite image (degrees C; shaded) and approximate surface-low position for (a) 0000 UTC 7 Apr 2008, (b) 0000 UTC 12 Dec 2010, (c) 0000 UTC 31 Dec 2010, and (d) 0000 UTC 2 Feb 2011. In (d), colder cloud tops, identified in green and blue, are collocated along or ahead the surface fronts and to the north-northwest of the approximate surface-low positions 72
- 2.3 Mosaics of Weather Surveillance Radar-1988 Doppler (WSR-88D) composite reflectivity and RUC- (a,c) and NAM-analyzed (b) mean sea-level pressure (mb; solid) and 2-m temperatures (K; dashed) for (a) 2 Feb 2011, (b) 11 Dec 2010, and (c) 27 Dec 2010. The mosaics are derived from the National Mosaic and Multisensor Quantitative Precipitation (NMQ-2013; Vasiloff et al. 2007) Estimation project. Approximate surface-low positions indicated by L and the reflectivity scale is beneath the panels 73
- 2.4 Figure 2.4: OU Prime observations showing 3 examples of radar reflectivity (dBZ; left), differential reflectivity (dB; center), and cross-correlation coefficient (right). [Taken from Dr. Heather Reeves, NSSL]. The dual-polarized radar data could be useful for nowcasting of potential icing environments..... 74
- 2.5 AMDAR PIREPs icing reports indicating ice detected (red) and no ice detected (blue) for the 6-h time periods indicated 75
- 2.6 250-hPa geopotential heights (dam; solid) and potential vorticity (PVU; shaded) for the times indicated above each panel. Enhanced areas of potential vorticity (greater than 4 PVU) are noted coincident along axes of the distinct shortwave troughs for each event 76
- 2.7 NAM-analyzed mean sea-level pressure (mb; solid) and 2-m temperatures (K; dashed) for each event. The pressure contours are in 4-mb intervals, while the temperature contours are in 2-K intervals 77
- 2.8 NAM-analyzed 500-hPa geopotential heights (m; solid) for each event. Pronounced shortwave troughs are evident for each of the cases 78
- 2.9 Mosaics of Weather Surveillance Radar-1988 Doppler (WSR-88D) composite reflectivity and RUC-analyzed mean sea-level pressure for (a)-(c) 6 Feb 2010, (d)-(f) 15 Feb 2010, and (g)-(i) 26 Jan 2010. The mosaics are derived from the

	NMQ (Vasiloff et al. 2007) Estimation project. Approximate surface-low positions indicated by L and the reflectivity scale is beneath the panels	79
2.10	Vertical cross-sections (indicated in Fig. 3.3 (b), (e), and (h)) of temperature (K; solid), including dendrite growth zone temperature (K; heavy label), RH > 95% (%; dashed), and vertical velocities (Pa/s; shaded)	80
3.1	Mean sea-level pressure (mb; solid) and 2-m temperatures (K) for (a) NAM-analyzed, (b) Thompson, (c), NSSL, (d) Milbrandt-Yau, and (e) Morrison for 0000 UTC 6 Feb 2010. Mean sea-level pressure is plotted in 4-mb intervals. Temperatures are plotted in 2-K intervals, below (blue), at (purple), and above (red) 273 K	81
3.2	Mean sea-level pressure (mb; solid) and 2-m temperatures (K) for (a) NAM-analyzed, (b) Thompson, (c), NSSL, (d) Milbrandt-Yau, and (e) Morrison for 0000 UTC 26 Jan 2011. Mean sea-level pressure is plotted in 4-mb intervals. Temperatures are plotted in 2-K intervals, below (blue), at (purple), and above (red) 273 K	82
3.3	Mean sea-level pressure (mb; solid) and 2-m temperatures (K) for (a) NAM-analyzed, (b) Thompson, (c), NSSL, (d) Milbrandt-Yau, and (e) Morrison for 1200 UTC 15 Feb 2010. Mean sea-level pressure is plotted in 4-mb intervals. Temperatures are plotted in 2-K intervals, below (blue), at (purple), and above (red) 273 K	83
3.4	500-hPa geopotential heights (m; solid) for (a) NAM-analyzed, (b) Thompson, (c), NSSL, (d) Milbrandt-Yau, and (e) Morrison for 0000 UTC 6 Feb 2010. Geopotential height field is plotted in 60-m intervals	84
3.5	500-hPa geopotential heights (m; solid) for (a) NAM-analyzed, (b) Thompson, (c), NSSL, (d) Milbrandt-Yau, and (e) Morrison for 0000 UTC 26 Jan 2011. Geopotential height field is plotted in 60-m intervals	85
3.6	500-hPa geopotential heights (m; solid) for (a) NAM-analyzed, (b) Thompson, (c), NSSL, (d) Milbrandt-Yau, and (e) Morrison for 1200 UTC 15 Feb 2010. Geopotential height field is plotted in 60-m intervals	86
3.7	Maximum column reflectivities (shaded) and sea-level pressure (hPa; solid) at 0300 UTC on 6 Feb 2010 for (a) Thompson, (b) NSSL, (c) Milbrandt-Yau, and (d) Morrison. The pressure contours are in intervals of 4 hPa and the reflectivity scale is shown on the right. The dashed parallelogram indicates the volume-integrated area for individual hydrometeor mixing ratios	87
3.8	Maximum column reflectivities (shaded) and sea-level pressure (hPa; solid) at 0300 UTC on 26 Jan 2011 for (a) Thompson, (b) NSSL, (c) Milbrandt-Yau, and (d) Morrison. The pressure contours are in intervals of 4 hPa and the reflectivity scale is shown on the right. The dashed parallelogram indicates the volume-integrated area for individual hydrometeor mixing ratios	88
3.9	Maximum column reflectivities (shaded) and sea-level pressure (hPa; solid) at 1500 UTC on 15 Feb 2010 for (a) Thompson, (b) NSSL, (c) Milbrandt-Yau, and (d) Morrison. The pressure contours are in intervals of 4 hPa and the reflectivity scale is shown on the right. The dashed parallelogram indicates the volume-integrated area for individual hydrometeor mixing ratios	89

3.10	Column-integrated precipitation mass (mm; shaded) at 0300 6 Feb 2010 for (a) Thompson, (b) NSSL, (c) Milbrandt-Yau, and (d) Morrison.....	90
3.11	Column-integrated precipitation mass (mm; shaded) at 0300 26 Jan 2011 for (a) Thompson, (b) NSSL, (c) Milbrandt-Yau, and (d) Morrison.....	91
3.12	Column-integrated precipitation mass (mm; shaded) at 1500 15 Feb 2010 for (a) Thompson, (b) NSSL, (c) Milbrandt-Yau, and (d) Morrison.....	92
3.13	Total 6-h accumulated liquid equivalent precipitation (in; shaded) ending at 0600 6 Feb 2010 for (a) Thompson, (b) NSSL, (c) Milbrandt-Yau, and (d) Morrison. Local maxima in comma-head region is indicated for each scheme.....	93
3.14	Total 6-h accumulated liquid equivalent precipitation (in; shaded) ending at 0600 26 Jan 2011 for (a) Thompson, (b) NSSL, (c) Milbrandt-Yau, and (d) Morrison. Local maxima in comma-head region is indicated for each scheme.....	94
3.15	Total 6-h accumulated liquid equivalent precipitation (in; shaded) ending at 1800 15 Feb 2010 for (a) Thompson, (b) NSSL, (c) Milbrandt-Yau, and (d) Morrison. Local maxima in comma-head region is indicated for each scheme.....	95
3.16	Vertical velocities (cm/s; shaded), temperature ranging from 264.5 to 269 (K; solid), and RH > 95% (%; dashed) at the 700-hPa geopotential level at 0300 UTC 6 Feb 2010 for (a) Thompson, (b) NSSL, (c) Milbrandt-Yau, and (d) Morrison. Temperature range between 264.5 and 269 K (1.5 K interval) is prime for hazardous icing conditions.....	96
3.17	As in Fig. 3.16, but for 0300 UTC 26 Jan 2011	97
3.18	As in Fig. 3.16, but for 1500 UTC 15 Feb 2010	98
3.19	Vertical cross-sections (indicated in Fig 3.1a) of theta-e (K; solid) and cloud water mixing ratio (g/kg; shaded) at 0300 UTC on 6 Feb 2010 for (a) Thompson, (b) NSSL, (c) Milbrandt-Yau, and (d) Morrison.....	99
3.20	Vertical cross-sections (indicated in Fig 3.2a) of theta-e (K; solid) and cloud water mixing ratio (g/kg; shaded) at 0300 UTC on 26 Jan 2011 for (a) Thompson, (b) NSSL, (c) Milbrandt-Yau, and (d) Morrison.....	100
3.21	Vertical cross-sections (indicated in Fig 3.3a) of theta-e (K; solid) and cloud water mixing ratio (g/kg; shaded) at 1500 UTC on 15 Feb 2010 for (a) Thompson, (b) NSSL, (c) Milbrandt-Yau, and (d) Morrison.....	101
3.22	Sums of (a) cloud water, (b) snow, and (c) total hydrometeor mixing ratios (kg/kg) in the comma-head region for February 6, 2010 for the times indicated (in UTC)	102
3.23	Sums of (a) cloud water, (b) snow, and (c) total hydrometeor mixing ratios (kg/kg) in the comma-head region for January 26, 2011 for the times indicated (in UTC)	103
3.24	Sums of (a) cloud water, (b) snow, and (c) total hydrometeor mixing ratios (kg/kg) in the comma-head region for February 15, 2010 for the times indicated (in UTC)	104
3.25	Aircraft envelope dimensions, per specifications from the FAA Airport and Aircraft Safety / Research and Development Icing Design Envelope Specification Final Report (April 2002).....	105
4.1	Maximum column reflectivities (shaded) and sea-level pressure (hPa; solid) at 0300 UTC 6 Feb 2010 for (a) CTRL, and (b) EFSW, at 0300 UTC 26 Jan 2011	

	for (c) CTRL, and (d) EFSW, and at 1500 UTC Feb 15 2010 for (e) CTRL, and (f) EFSW	106
4.2	Column-integrated precipitation hydrometeors (mm; shaded) at 0300 UTC 6 Feb 2010 for (a) CTRL, and (b) EFSW, at 0300 UTC 26 Jan 2011 for (c) CTRL, and (d) EFSW, and at 1500 UTC Feb 15 2010 for (e) CTRL, and (f) EFSW	107
4.3	Total 6-h accumulated liquid equivalent precipitation (in; shaded) ending at 0600 UTC 6 Feb 2010 for (a) CTRL, and (b) EFSW, at 0600 UTC 26 Jan 2011 for (c) CTRL, and (d) EFSW, and at 1800 UTC Feb 15 2010 for (e) CTRL, and (f) EFSW	108
4.4	Vertical cross-sections of θ_e (K; solid) and cloud water mixing ratio (g/kg; shaded) at 0300 UTC 6 Feb 2010 for (a) CTRL, and (b) EFSW, at 0300 UTC 26 Jan 2011 for (c) CTRL, and (d) EFSW, and at 1500 UTC Feb 15 2010 for (e) CTRL, and (f) EFSW	109
4.5	Column-integrated precipitation hydrometeors (mm; shaded) at 0300 UTC 6 Feb 2010 for (a) CTRL, and (b) ESD, at 0300 UTC 26 Jan 2011 for (c) CTRL, and (d) ESD, and at 1500 UTC Feb 15 2010 for (e) CTRL, and (f) ESD.....	110
4.6	Vertical cross-sections of θ_e (K; solid) and cloud water mixing ratio (g/kg; shaded) at 0300 UTC 6 Feb 2010 for (a) CTRL, and (b) ESD, at 0300 UTC 26 Jan 2011 for (c) CTRL, and (d) ESD, and at 1500 UTC Feb 15 2010 for (e) CTRL, and (f) ESD.....	111
4.7	Column-integrated precipitation hydrometeors (mm; shaded) at 0300 UTC 6 Feb 2010 for (a) CTRL, and (b) SPSS, at 0300 UTC 26 Jan 2011 for (c) CTRL, and (d) SPSS, and at 1500 UTC Feb 15 2010 for (e) CTRL, and (f) SPSS.....	112
4.8	Vertical cross-sections of θ_e (K; solid) and cloud water mixing ratio (g/kg; shaded) at 0300 UTC 6 Feb 2010 for (a) CTRL, and (b) SPSS, at 0300 UTC 26 Jan 2011 for (c) CTRL, and (d) SPSS, and at 1500 UTC Feb 15 2010 for (e) CTRL, and (f) SPSS	113
4.9	Column-integrated precipitation hydrometeors (mm; shaded) at 0300 UTC 6 Feb 2010 for (a) CTRL, and (b) CAP, at 0300 UTC 26 Jan 2011 for (c) CTRL, and (d) CAP, and at 1500 UTC Feb 15 2010 for (e) CTRL, and (f) CAP	114
4.10	Vertical cross-sections of θ_e (K; solid) and cloud water mixing ratio (g/kg; shaded) at 0300 UTC 6 Feb 2010 for (a) CTRL, and (b) CAP, at 0300 UTC 26 Jan 2011 for (c) CTRL, and (d) CAP, and at 1500 UTC Feb 15 2010 for (e) CTRL, and (f) CAP	115
4.11	Column-integrated precipitation hydrometeors (mm; shaded) at 0300 UTC 6 Feb 2010 for (a) CTRL, and (b) COCD, at 0300 UTC 26 Jan 2011 for (c) CTRL, and (d) COCD, and at 1500 UTC Feb 15 2010 for (e) CTRL, and (f) COCD	116
4.12	Vertical cross-sections of θ_e (K; solid) and cloud water mixing ratio (g/kg; shaded) at 0300 UTC 6 Feb 2010 for (a) CTRL, and (b) COCD, at 0300 UTC 26 Jan 2011 for (c) CTRL, and (d) COCD, and at 1500 UTC Feb 15 2010 for (e) CTRL, and (f) COCD.....	117
4.13	Sums of (a) cloud water, (b) snow, and (c) total hydrometeor mixing ratios (kg/kg) in the comma-head region for February 6, 2010 for the times indicated (in UTC)	118
4.14	Sums of (a) cloud water, (b) snow, and (c) total hydrometeor mixing ratios	

	(kg/kg) in the comma-head region for January 26, 2011 for the times indicated (in UTC)	119
4.15	Sums of (a) cloud water, (b) snow, and (c) total hydrometeor mixing ratios (kg/kg) in the comma-head region for February 15, 2010 for the times indicated (in UTC)	120

Abstract

Numerical model experiments are conducted to assess how aircraft icing forecasts are affected by the choice of microphysical parameterization, with respect to the presence of supercooled liquid water (SLW). Select winter storms are investigated that are observed to have elevated regions of SLW, a condition for hazardous icing environments. The schemes considered include the Thompson, Milbrandt-Yau, Morrison, and National Severe Storms Laboratory (NSSL) microphysics parameterizations. The Thompson scheme routinely produces less SLW than the other three schemes. Sensitivity experiments reveal this difference is in large part a consequence of scavenging of cloud water from snow. In some environments, the Morrison scheme produces considerably more SLW than the other parameterization schemes. The output from each experiment is compared to aviation pilot reports of aircraft icing to determine which scheme yields the most accurate results. According to all statistical measures that we explored, the predictability of SLW seems to be best represented by Morrison. However, the results are not drastically different between the schemes.

Chapter 1

Introduction

This chapter will explore the motivation for our research, including a discussion on the threat for airframe icing accidents in the United States, as well as a brief overview of the history of aviation weather and icing forecasts. In Section 1.2, the ingredients for airframe icing are investigated and the techniques for forecasting of such hazards are explored. Section 1.3 discusses the threat for icing environments to collocate with comma-head precipitation systems, and, lastly, the objectives of this project are laid out in Section 1.4.

1.1 Motivation for Research

One of the most significant dangers in aviation weather is the accumulation of in-flight ice on the surface of aircraft (Lewis 1947; Thompson 1955; Air Weather Service 1980; Cooper et al. 1984; Politovich 1988; Sand 1991; Rasmussen et al. 1992; Bragg 1996; Tremblay et al. et al. 1996; Bernstein et. al. 1997; Bernstein et. al. 2005; Schultz and Politovich 1992; Politovich 2000; Politovich 2003; Czernkovich 2004; Petty and Floyd 2007). Icing reduces lift and thrust and increases the weight and drag of the aircraft (Air Weather Service 1980; Rasmussen et al. 1992; Petty and Floyd 2007; Politovich 2003). Icing also inhibits the function of any moving mechanical parts on the aircraft, such as those used to increase the airspeed and pitch, which are often utilized to counteract the effects of increased drag (Air Weather Service 1980). Icing can affect

aircraft of all types and sizes, but is particularly hazardous for small aircraft that are often not equipped with the deicing equipment and propulsion power that accompany commercial aircraft (Tafferner et al. 2003). Nevertheless, airframe icing still poses a danger for commercial aircraft and is thought to have been the primary cause of the crash of American Eagle Flight 4184 near Roselawn, Indiana in 1994, which took 68 lives (Cober et al. 2001). More than 80% of all icing-related aircraft incidents occur between the beginning of October and the end of March. In fact, in the 18-year span between 1982 and 2000, more than 800 fatalities have been attributed to airframe icing accidents in the United State alone. Despite the inherent danger, there was a decrease in the number of icing-related accidents in the U.S. during this period, from a high of 49 in 1982 to 17 in 2000. This decline is presumably due to improved forecasting techniques and pilot awareness/training (Petty and Floyd 2007). Improved forecasting techniques include the employment of numerical weather prediction (NWP) models. Uncertainties introduced via NWP model parameterization schemes can potentially affect icing forecasts. Of particular interest is the uncertainty due to the microphysical parameterization scheme. Such an investigation is the topic of this paper, which aims to characterize the sensitivities of aircraft icing forecasts among four microphysical parameterizations. The scheme forecasts are explored to qualitatively assess whether icing forecasts may be improved on the bases of the choice of microphysical parameterization. The operational employment of such schemes is explored, with regards to the forecasting of hazardous icing environments. The goals of this research are consistent with recommendations made by the National Transportation Safety Board (NTSB) to “continue to sponsor the development of methods to produce weather

forecasts that both define specific locations of atmospheric icing conditions... and produce short-range forecasts that identify icing conditions for [a] specific geographic location” (Bernstein et al. 2005).

1.2 Overview of Control Parameters and Forecasting of Icing

There are a number of factors that affect the existence and severity of aircraft icing. Some of these factors are nonmeteorological, including the type and speed of the aircraft, the pitch of the aircraft, and whether de-icing fluids were applied before takeoff. Meteorological factors include the type of precipitation, the type, location, altitude, thickness, and temperature of clouds, vertical velocity, temperature, relative humidity, and the size of supercooled liquid water droplets (Cooper et al. 1984; Sand 1985; Cole and Sand 1991; Schultz and Politovich 1992; Bragg; 1996; Politovich 2003; McDonough et al. 2003; Bernstein et. al. 2005).

While these ingredients are used to establish the threat for icing, the methods used to assess the atmosphere for the aviation industry has changed since the birth of aviation. Within a decade of the Wright brothers’ 1903 flight, aviation weather became a staple of weather forecasting. In 1918, the Weather Bureau began issuing bulletins and forecasts for domestic military flights and air mail routes, relying heavily on ground and kite station observations. Since as early as the 1930s, aviation has provided vital atmospheric data to both civilians and forecasters; although, initially, a greater emphasis was placed on what *was* happening and not what *would* happen. Nevertheless, until the 1940s employment of weather balloons and radiosondes, aircraft instruments were the

main method for assessing the state of the atmosphere. Early forecasting techniques of aircraft icing relied heavily on such measurements, using the temperature and low dewpoint depression (D_d) as the primary parameters for assessing in-flight icing hazards (Lewis 1947; Lewis 1951; Thompson 1955). This approach, although somewhat primitive, was based on statistical studies from research flights that linked the number of airframe icing reports to low D_d (Thompson 1955). However, lack of observations, both on a horizontal and vertical scale, limited the forecasting capabilities for several decades.

Along with radiosonde observations, radar data came into play as early as the 1940s, marking the start of a weather radar system across the U.S. The new radar data, while not directly used to detect hazardous icing conditions, did provide forecasters with a more complete perspective of the precipitation occurring, which has been shown to have an effect on icing environments (Cooper et al. 1984; Hansman 1989; Rasmussen et al. 1992; Czernkovich 2004, Bernstein et al. 2005). A second indicator that has historically been used to forecast icing is the environmental temperature as icing preferentially occurs in regions where the temperature ranges from 258 to 263 K (Sand 1985; Schultz and Politovich 1992; Politovich 2000; Politovich 2003; Bernstein et al. 2005). In fact, early aircraft icing forecasting techniques utilized primarily the ideal temperature range and high relative humidity (Thompson 1955), but were subjective and quite time consuming (Modica et al. 1994) and were shown to be inadequate to control the icing threat (Green 1997; Tafferner et al. 2003). However, with the introduction of mainstream satellite data in the 1960s, forecasters were able to view cloud cover from an entirely new perspective. This data, which was vital for assessing

where extensive cloud cover was positioned, combined with a network of radars and radiosonde launch sites, provided forecasters with an unprecedented comprehensive detail of the atmosphere. Despite this, even though other parameters such as droplet diameter and liquid-water content had been recognized as being important for airframe icing since the 1940s, the prediction of such ingredients was still fairly limited (Heymsfield and Parrish 1978; Cooper et al. 1984; Sand 1985). It was not until the advent of research aircraft cloud particle probes in the late 1970s that better observations and forecasting of cloud particles became possible.

Although the first computer model weather forecast was first introduced in 1950, widespread use of computer capacities occurred many years later. As technology has advanced, so too has the ability for models to be used as a tool for forecasting aircraft icing. Before the 1990s, NWP models only determined the effects of the ingredients for icing, but forecasts of icing were still mainly based on statistically-derived algorithms that used model forecasts of temperature and relative humidity to derive a field for potential icing. Many algorithms were based on statistical evaluation of Pilot Reports (PIREPs) of icing, and the majority of research on the topic had been performed on orographically-enhanced environments and ideal setups, such as in wind tunnels. However, in the early 1990s, the Winter Icing and Storms Project (WISP) aimed to study the processes leading to the formation and depletion of supercooled liquid water in winter storms and improve forecasts of aircraft icing (Rasmussen et al. 1992). In order to address the need for improved icing forecasts and a renewed attention to the hazard, WISP explored both the basic and applied topics in winter storm research in a manner that had never been done before. Many of the aircraft paths for WISP were

taken near cloud tops to establish whether ice crystal concentrations could be correlated with temperature in the Front Range (Rasmussen et al. 1992). More recently, as numerical weather prediction (NWP) models have become more advanced, the most widely-utilized techniques have evolved to make use of more variables, including the precipitation rate, cloud top temperatures, cloud depth, and the amount of supercooled liquid water (SLW). In an NWP model, these variables are strongly influenced by the microphysical parameterization scheme.

Today, the Aviation Weather Center (AWC) in Kansas City, MO issues warnings that cover the United States and large portions of the northern Pacific and Atlantic airspaces for altitudes below 45,000 ft. The AWC, along with more than 120 National Weather Service (NWS) forecast offices, serve over 575 airports with almost 25,000 daily aviation weather forecasts and 1,300 in-flight forecasts. These organizations use a variety of icing products, derived from a variety of data. Previous studies have investigated icing environments using satellite data (Rosenfeld and Lensky 1998; Smith et al. 2000; Ellrod and Bailey 2007; Smith et al. 2012), Special Sensor Microwave data (SSM/I; Tremblay et al. 1996); model, lightning, (PIREPs), METAR, and radar data (CIP; Bernstein et al. 2005), and model parameter output (Modica et al. 1994; Guan et al. 2001; McDonough et al. 2003; Thompson et al. 2008; Nygaard et al. 2011). The Forecasting Icing Potential (FIP; McDonough et al. 2003) uses model forecasts of cloud-top temperatures, cloud depth, environmental temperature, and vertical velocity (McDonough et al. 2003; McDonough et al. 2004). However, explicit predictions of SLW are not considered important in the FIP product. Surprisingly, model predictions of both cloud-top height and temperature and presence of SLW have been found to be

an unreliable, presumably due to uncertainties in the microphysical parameterization schemes (Reisner et al. 1998; Tafferner et al. 2003; Thompson et al. 2004; Thompson et al. 2008).

1.3 Icing in Comma-Head Snowstorms

The preference for icing to occur in environments whose temperatures range from 258 to 263 K has been a point of interest, since in this range, both liquid water and ice may co-exist, leading to the rapid growth of dendrites (Hobbs 1975; Sienkiewicz et al. 1989; Stark et al. 2013). Dendrite growth zones are not restricted to certain storms or locales, but they are commonly observed in the comma-head portion of midlatitude storms (Sienkiewicz et al. 1989; Stoelinga et al. 2007; Stark et al. 2013). The comma-head portion of extratropical cyclones refers to the cloud and precipitation structures that form to the north or northwest of the cyclone centers near occlusion. The location of the dendrite zone is often in the comma-heads of storms, where a high frequency of PIREPs icing reports are often observed (Bernstein 1997). In the typical midlatitude cyclone (Fig. 1.1), warm, moist air is transported northward over the surface warm front and then north and west of the surface low-pressure center, thus providing an influx of liquid water into the comma-head portion of the storm (Rasmussen et al. 1992). This liquid water is a primary indicator of icing conditions (Brown et al. 1997). Previous research of PIREPs indicates that icing is most prevalent in the comma-head portions of midlatitude cyclones relative to other regions within the cyclone (Bernstein 1997). Many of the favorable ingredients for aircraft icing collocate in the comma-head regions

of extratropical cyclones. Reisner et al. (1998) found in their investigation of a comma-head cloud system that there were high SLW concentrations within the comma-head region. They additionally found from aircraft observations that SLW values were the highest at lower altitudes and decreased downstream from the cyclone center. Conversely, Rauber and Tokay (1991) and Rasmussen et al. (1992) have found high SLW values near the cold cloud tops. These conclusions are consistent with the findings of Hobbs and Rangno (1985), who examined a database of research aircraft data and found that a layer of SLW at the tops of cold cloud tops was common. Moreover, Solomon et al. (2011) found that cloud liquid water is maintained near cloud tops and that the liquid water is generated in the updraft portions of the cloud beneath the cloud tops. Additionally, Solomon et al. (2011) found that in the presence of a mixed-layer entrainment zone, a humidity inversion can be the only provider for water vapor for the cloud system.

Despite the preference for icing to occur in the comma-head region of midlatitude storms, very little research has been done to determine the sensitivity of icing forecasts to the choice of NWP microphysical scheme. Given that icing can only occur in the presence of SLW, it is reasonable to question to what extent a forecast of SLW may be dependent on the choice of microphysical parameterization. Of particular interest are the effects of using a double-moment parameterization scheme, which allow for a more robust treatment of the particle size distributions (in comparison to single-moment schemes), which are a key for calculating the microphysical process rates and cloud and precipitation evolution (Skamarock et al. 2008). The literature is not forthcoming with research that addresses this subject, but one may reason that double-

moment schemes may improve forecasts of SLW because they allow for size sorting (Walko et al. 1995; Reisner et al. 1998; Thompson et al. 2004; Nygaard et al. 2011). Size sorting allows large particles to exist at lower levels more so than upper levels by virtue of their large terminal fall speeds. Without permission of size sorting, the mean size of the particles would decrease with height (Milbrandt and Yau 2005). Hence, double-moment schemes may more accurately capture the tendency for SLW to be located at lower altitudes within the cloud. Previous studies addressing the differences between single- and double-moment schemes in winter storms show there is improvement in the representation of key microphysical processes when one uses a double-moment scheme (Reisner et al. 1998; Morrison and Pinto 2006; Milbrandt and Yau 2005; Seifert and Beheng 2006; Thompson et al. 2008; Milbrandt et al. 2010; Nygaard et al. 2011; Molthan and Colle 2012). Further study is warranted. However, there is some evidence that the prediction of cloud water aloft may be underestimated in some double-moment schemes (Milbrandt et al. 2010) or that increasing the number of moments has little effect on the precipitation (Reeves and Dawson 2013).

1.4 Research Objectives

The aim of this study is to assess how icing forecasts are impacted by changes to the microphysical parameterization scheme in the comma-head region of midlatitude cyclones. To accomplish this, three particular cases of comma-head cyclones are chosen to perform multiphysics sensitivity experiments using a suite of sophisticated microphysical parameterizations. The remainder of this paper presents a comprehensive

overview on the evolution of comma-head snow events and the accompanying cloud and precipitation patterns associated with such systems. Issues with NWP aircraft icing forecasts are explored and a method for evaluation of scheme solutions with PIREPs is described for each event. The prevailing synoptic and mesoscale flows are also investigated for each cyclone. In Chapter 3, the experimental design for the simulations is presented, followed by a comprehensive comparison of partially- and fully-double moment scheme forecasts, which are validated with PIREPs. Chapter 4 presents forecasts from several sensitivity tests on the partially-double moment scheme, which are consequently compared with the control experiments described in Chapter 3. In Chapter 5, conclusions are made regarding the interchange of microphysical parameterization and the associated effects on NWP modeling of icing and speculations on aircraft icing forecasts are explored for future research and operational use.

Chapter 2

Background

Chapter 2 explores the formation and evolution of typical cold-season mid-latitude cyclones that lead to comma-head cloud and precipitation systems. The ingredients for precipitation development, and their relationship to aircraft icing in this sector of the cyclone are discussed in Section 2.1.1. Typical satellite patterns of comma-head events are examined in Section 2.1.2, while a thorough exploration of forecasting of SLW is assessed in Section 2.2. Previous studies on the modeling and production of SLW, and the link to aircraft icing forecasts, are considered in Section 2.2. Meanwhile, Section 2.3 discusses the icing reports for our storm investigations, and Section 2.4 explores the overall synoptic- and meso-scale overviews for the cyclones considered for this research.

2.1 Precipitation Generation in Comma-Head Portions of Mid-Latitude Storms

2.1.1 Formation of Comma-Head Snowstorms

The formation of a comma-head cloud system occurs coincident with the occlusion of a midlatitude cyclone. The occlusion process is depicted in Fig. 2.1. Before occlusion, the cold conveyor belt approaches the low-pressure center from the east

(assuming a northern hemisphere rotation) and wraps cyclonically around the north side of the low (Fig. 2.1a). Here, the term “conveyor belt” refers to an ensemble of parcels having approximately the same thermodynamic characteristics (Moore et al. 2004). These airstreams have been noted to contain narrow ranges of potential temperature or wet-bulb temperature according to the airstream’s origin (Browning 1990; Carlson 1991). A conveyor belt can be thought of as an ensemble of air parcels that originate from similar source regions and track over synoptic-scale time periods (Moore et al. 2004). The warm conveyor belt extends northward ahead of the surface cold front and ascends over the surface warm front and turns anticyclonically, traveling downstream away from the low-pressure center. After occlusion, a bifurcation of the warm conveyor belt is observed to the north of the warm front, just to the east-northeast of the low-pressure center (Fig. 2.1b). The cyclonic curving around the upper-level low has long been recognized (e.g. Bjercknes 1932; Namias 1939; Golding 1984; Browning 1990; Martin 1999) and this airstream is sometimes referred to as a trough of warm air aloft, or TROWAL (Iskenderian 1988; Martin 1998). Also shown in Fig 2.1b is the dry airstream, which initially descends as it approaches from the west, but then ascends as it nears the low-pressure center. The three conveyor belts identified in a typical mid-latitude cyclone (warm, cold, dry) have long been established to evolve during cyclogenesis, and were first established using relative-wind analysis (Danielsen 1964; Harold 1973; Carlson 1980). The superposition of the dry airstream (Danielsen 1964) overtop of the warm conveyor belt introduces a potential for some form of instability to exist, which can lead to convection within the comma-head region. The overrunning of high θ_e air associated with the warm conveyor belt by the low θ_e air associated with the

dry conveyor belt provides instability due to differential moisture advection. The three-dimensional interaction of these airstreams in the vicinity of the extratropical cyclone can promote an environment conducive to banded precipitation in the comma-head region due to increased instability (Nicosia and Grumm 1999).

There are several types of stability to be considered when investigating the probability of convection in the comma-head portion of midlatitude cyclones, including conditional instability (CI), moist symmetric instability (MSI), and conditional symmetric instability (CSI). The term symmetric instability is sometimes used interchangeably with slantwise convection, because the release of instability occurs as a result of slantwise motions, such as one would observe in the warm conveyor belt as it ascends over the warm front and curves around the low (Bennetts and Hoskins 1979; Dunn 1987; Schultz and Schumacher 1999). In fact, it has been well established that slantwise motions can lead to formation of SLW at higher levels in the troposphere, between 500 – 600 hPa (Modica et al. 1994).

Moist symmetric instability occurs in an environment where the saturation equivalent potential temperature (θ_{es}) decreases with height and the moist potential vorticity (MPV) is less than 0, where

$$\text{MPV} = g\boldsymbol{\eta} \cdot \boldsymbol{\nabla}\theta_{es} \quad . \quad (2.1)$$

In (2.1), g is gravity, $\boldsymbol{\eta}$ is the three-dimensional absolute vorticity vector, and $\boldsymbol{\nabla}$ is the three-dimensional gradient operator (Schultz and Schumacher 1999). As has been found by previous investigators, multiple forms of instability may simultaneously be present in the comma-head region (Hoskins 1974; Bennetts and Hoskins 1979; Dunn 1987;

Rasmussen et al. 1992; Schultz and Knox 2007; Novak et. al. 2010; Schumacher et. al. 2010). The convective motions stimulated by the release of instability may act to transport SLW drops to higher altitudes within the cloud. The transport of SLW is consistent with previous observations taken from within comma-head storms (Molthan and Colle 2012; Stark et al. 2013).

2.1.2 Cloud and Precipitation Patterns in the Comma-Head Region

Examples of satellite images from midlatitude cyclones with comma-head clouds are shown in Fig. 2.2. In these examples, there are regions of cold cloud tops that are parallel to the surface cold fronts and arching over the surface low-pressure center (indicated in Fig. 2.2d). These cold temperatures correspond to high cloud tops. Farther west in the comma-head region, the cloud top heights decrease, as is the case in most extratropical cyclones. There is support of occasional convective motions (see Fig. 2.2c), evidenced by north-south bands of alternating higher and lower cloud tops. However, convection is not always evident. In Fig. 2.3 the composite mosaic radar reflectivities for three different comma-head snow events is shown, along with North American Mesoscale model (NAM; Janjić 2005) analyzed mean sea-level pressure. It is clear from Fig. 2.3a,b that a transition occurs between the precipitation shield associated with the cold front and the comma-head region. In all three cases, the comma-head precipitation extends to the north and northwest of the surface low and is often banded and convective in nature.

While traditional radars have not been useful for diagnosing icing conditions,

observations from dual polarized radar are useful for detecting electrification, which can be used to infer presence of SLW or LWC (Vivekanandan et al. 1996a; Vivekanandan et al. 2001; Ryzhkov and Zrnić 2007). Although the NEXRAD radars have only recently been upgraded with this technology, observations of winter storms taken by the OU Prime C-Band radar show clear signatures that indicate the presence of SLW in comma-head snowstorms, and show promise for future icing assessments. Consider Fig. 2.4, which shows radar reflectivity, differential reflectivity (Z_{dr}), and the correlation coefficient (ρ_{hv}) for three different comma-head events over central Oklahoma. Although the reflectivity and ρ_{hv} are inconclusive, the Z_{dr} plots have regions of alternating high and low values at the peripheries of the domains. This pattern is the so-called depolarization signature and indicates the presence of electrification (Ryzhkov and Zrnić 2007), which is a sign that there is liquid present in the cloud (Ryzhkov et al. 1998; Vivekanandan et al. 1996a; Vivekanandan et al. 2001). Another common dual polarized signature indicative of SLW is the high Z_{dr} turret, which are vertical columns of high Z_{dr} that indicate the upward transport of SLW (Vivekanandan et al. 2001). These patterns have also been observed in comma-head snowstorms over central Oklahoma. This new radar data, which has just become operationally and nationally available, may be extremely helpful in the nowcasting of icing environments in winter precipitation bands. The radar data offers a method for assessing the current threat for icing and could be used for an effective icing warning system. An investigation should be considered for future utilization of dual polarized data; however, such a discussion is not explored here.

2.2 Forecasting of SLW

Prior to the establishment of NWP models, aircraft icing predictions were entirely based on statistical or empirical techniques (Modica et al. 1994; Tremblay et al. 1996). However, more recently, NWP forecasts have been used to predict icing (Schultz and Politovich 1992; Modica et al. 1994; Tremblay et al. 1996; Reisner et al. 1998; Guan et al. 2001; Thompson et al. 2004; Nygaard et al. 2011). Bulk microphysical parameterizations incorporate a size distribution that follows a preset functional form. Additionally, they allow for explicit predictions of cloud/precipitation species, which can then be used to infer the likelihood of icing (Thompson et al. 2004; Morrison and Grabowski 2008). Yet, simulations of cold cloud systems reveal some schemes have an overabundance of snow and ice that inhibits the scheme's ability to produce SLW (Thompson et al. 2004). In fact, it has been well established by Cooper and Marwitz (1980) that ice (snow) crystals can deplete liquid water within the cloud. Sensitivity tests show that subtle alterations of thresholds and constants used by a scheme are critical in predicting whether SLW exists or not (Thompson et al. 2004). These subtle sensitivities involve an intricate balance between cloud water, cloud ice, snow, and graupel. In cases where the clouds are dominated by snow, as in the comma-head region, simulations have revealed that the SLW tends to be underpredicted, resulting in a misleading forecast of aircraft icing probability (Thompson et al. 2004).

While the literature on microphysical parameterization scheme effects on airframe icing has not been forthcoming, there have been investigations on scheme forecasts of SLW in comparison to aircraft observations. The WISP investigations in the early

1990s, which involved two research aircraft that were equipped for cloud physics, thermodynamic, and air-motion measurements, was one of the first studies aimed to improve forecasts of aircraft icing in winter storms specifically. The project used research aircraft, radar, radiometer, sounding, profile, and satellite data to investigate winter storms along the Front Range of the Rocky Mountains between 1990 and 1991. WISP also used several computer models, such as the PSU/NCAR Mesoscale Model (MM4; Anthes et al. 1987), the RAMS model (Tripoli and Cotton 1982; Wesley 1991), and the NCAR Clark model (Clark 1977) for 24- and 48-h forecasts with a 30-km horizontal resolution. These forecasts provided meteorologists with experience in utilizing experimental data, advanced objective analysis techniques, and model output. However, 24-h forecasts of the NMC nested-grid model (NGM) were often mediocre or even poor. In fact, only 50-75% of the RH was verified by the aircraft measurements. The forecasts were also used for 1- and 3-hr nowcasts for the Denver Stapleton Airport. In research aircraft measurements, however, many of the encounters of large SLW droplets took place near the tops of stratiform clouds in the presence of strong wind shear and a sharp increase in potential temperature through the sheared layer. In these environments, the temperature was found to be warmer than 255 K, with severe icing occurring with liquid water contents as low as 0.14 gm^{-3} . WISP proposed several decision trees, both for icing outlook and icing nowcasts, which can be used both diagnostically and prognostically by aviation forecasters (Rasmussen et al. 1992).

The WISP Real-Time Icing Prediction and Evaluation Program (WRIPEP) investigated real-time displays and evaluation of icing forecasts based on several algorithms and NWP models. The output and verification data was collected and

archived to evaluate the forecasts and algorithms. However, the data showed a large trade-off between the predicted extent of icing forecast and the ability to detect icing. As one might expect, the probability of detection (POD) increased as the forecast area of icing increased, and vice versa. However, it was emphasized that relying on one forecast characteristic, such as just temperature, can lead to mistaken conclusions about the forecast ability. However, verification results for explicit cloud liquid water in the Eta Model suggested usefulness and forecast skill for using liquid water content as an icing predictor (Brown et al. 1996).

Additional studies involving NWP model output and algorithms were conducted by Schultz and Politovich (1992). The investigation used the Nested Grid Model (NGM) to formulate and evaluate algorithms with icing levels. The study showed that the manual procedures employed by the National Aviation Weather Advisory Unit (NAWAU), now AWC, captured 75% of PIREP icing reports. However, NGM output icing products showed only slight improvement over traditional analysis of graphical model outputs. Icing algorithms (products) were also investigated by Forbes et al. (1993), who used verification results to optimize icing forecasts from the 80-km Eta Model. However, all of these algorithms were based on strict grid point temperature and humidity criteria.

A comparison study of NWP forecasts of SLW to aircraft observations was performed by Guan et al. (2001). Their model forecasts agreed well with observations of temperature, wind speed, and dewpoint. Yet, comparisons of forecast SLW to aircraft observations showed that forecasts underestimated the total water content. The significant horizontal variability in vertical velocity contributed to the underforecast of SLW. Nevertheless, Guan et al. found that there is a non-negligible control on the

production of SLW imposed by the microphysical parameterization scheme.

A similar study involving comparisons of NWP model parameters to aircraft observations was conducted by Vaillancourt et al. (2002). The investigation concluded NWP models generally overpredict ice water content, while simultaneously underpredicting the supercooled liquid water content (SLWC). Vaillancourt et al. also found that for mixed-phase clouds, the ice phase represents a large fraction of the total water content, which was not consistent with aircraft observations. Additionally, like in Guan et al. (2001), results showed that it was more difficult to predict water content variables than dynamic variables. The study concluded that the NWP model overpredicted the frequency of glaciated clouds and underpredicted supercooled clouds, as well as the total supercooled liquid water content.

Reisner et al. (1998) performed several forecasts of a shallow midlatitude cyclone each with a different microphysical parameterization scheme. Like Guan et al. (2001), they found that a model's ability to accurately capture the SLW field is limited by its ability to accurately capture the kinematic (i.e. vertical velocity) and thermodynamic fields. But, their results also show that when the number of moments is increased from one to two, more accurate forecasts of SLW (as compared to aircraft observations) are obtained. However, like Guan et al. (2001), Reisner et al. found that NWP models often underforecast SLW, when compared to aircraft observations.

A similar experiment by Nygaard et al. (2011) studied in-cloud icing using the Weather Research and Forecasting (WRF; Skamarock et al. 2008) model to explicitly predict the amount of supercooled liquid water content (SLWC) at different horizontal

resolutions using several microphysics schemes, including the Thompson (TSON; Thompson 2004, 2008), the Morrison (MORR; Morrison and Pinto 2006), and the Eta Grid-Scale Cloud and Precipitation scheme (EGCP01; Rogers et al. 2001). The investigation concluded that not only does the quality of SLWC predictions decrease dramatically with decreasing model resolution, but systematic differences exist in the predictive skill between microphysics schemes, despite similar predictions of the synoptic-scale weather setup. The TSON scheme was shown to underpredict the SLWC, in comparison to both the measurements and MORR for a 3-km grid spacing. While the TSON did show improved forecasts for a 0.33-km grid spacing, such a horizontal resolution is not currently realistic for operational utilization. Moreover, forecasts were evaluated with measurements atop Mount Ylläs in Northern Finland, and were not directly compared with pilot reports. Additionally, the criteria for the events studied did not include any condition of precipitation or temperature profile, and the environments had a strong orographic-dependency.

2.3 Icing Reports For Each Event

Ice reports via PIREPs can be a tool for evaluation of NWP solutions, and remain a vital part in a movement to improve the forecasting of icing conditions for the aviation industry. Even though PIREPs have their usefulness, their limitations, including sparse spatial and temporal coverage, are well documented. PIREPs icing reports have known errors in the reports of time, altitude, and location (Brown 1993; Brown et. al. 1997; Brown 1996; Kelsch and Wharton 1996) and are often criticized for their non-

uniformity (Bernstein et. al. 1997; Bernstein et. al. 2005). It has been postulated that verification data that are systematically associated with the forecasts would be preferable to the incongruity sometimes found with PIREPs (Brown et al. 1997). However, with the advancement of aircraft measurements and employment by commercial airliners, PIREPs are currently more systematic today than 15 years ago. Moreover, PIREPs data is useful in providing forecast guidance during winter weather events (Bernstein et. al. 1997; Politovich 2003; Bernstein et. al. 2005).

To assess the dependence of the presence of SLW on the choice of microphysical parameterization, forecasts of three events are considered. These events occurred on 6 Feb 2010, 15 Feb 2010, and 26 Jan 2011, and are chosen on the basis of relatively high frequency of airframe icing accidents in the Great Lakes area (Petty and Floyd 2007). Additionally, the number of PIREPs icing reports through the comma-head region of each event near the time of maximum intensity allowed for a complete evaluation of scheme forecasts. We focus our attention on 6-hr periods from each case during the time when the most icing was reported. The PIREPs are acquired from the Earth System Research Laboratory/ Global Systems Division (GSD) aircraft database. The data is retrieved from the Aircraft Meteorological Data Relay (AMDAR; Grooters et al. 2003). The AMDAR data comes from seven domestic commercial airlines that work in collaboration with GSD. The data is decoded and is quality-controlled at GSD in a method similar to the processing of data from other aeronautical reporting systems, such as ACARS, which are critical for the Rapid-Update-Cycle (RUC; Benjamin 1989) model. The PIREPs include the aircraft's latitude, longitude, altitude, and time. Other parameters frequently included are the air temperature, wind direction and speed, as

well as presence of potentially hazardous conditions, such as turbulence or icing. Because these are automated reports, errors in time and location are not a factor.

For this paper, only flight information from aircraft that reported either icing or no icing is considered. The icing or no icing report is generated from one of two sensors. The measurements are taken either from a thin film capacitive sensor attached to the airfoil, or a mechanical (vibrating transducer) sensor exposed to the airstream in a probe adjacent to the relevant flying surface. The output from these sensors produces an ice/no ice signal. Ice intensity measurements from such sensors are not possible, and, thus, are not considered in this paper.

Statistics from individual events are summarized in Table 2.1. The 6 Feb case had the highest percentage of ice reports, while the 15 Feb event had the lowest. Table 2.1 also shows the distribution of reports for each case per 100-hPa vertical layer. All three events had the highest percentage of total reports and ice reports in the 600 – 700-hPa layer, with fewer than 22% of all reports being ice reports above the 600-hPa level (compared with over 40% below). Fig. 2.5 shows the AMDAR icing reports for each case. In each event, the majority of icing reports occur very close to airports, suggesting that the SLW exists at lower altitudes within the cloud systems, consistent with the findings of Reisner et al. (1998). We also see a mix of icing and non-icing reports within individual flight tracks and across the same geographical areas, suggesting that SLW is not evenly distributed in time and space, consistent with the findings of Guan et al. (2001). This could be a consequence of convective motions within the systems, which may result in a transport of SLW to higher altitudes within the cloud. Observational studies of precipitation within the convective part of comma head

snowstorms show moderate to heavy riming (Stark et al. 2013), but further information regarding the distribution of SLW due to convective motions cannot be determined using only this dataset.

6-Feb					
TOTAL		ICING		NO ICING	
900 - 1000 hPa	16	900 - 1000 hPa	11	900 - 1000 hPa	5
800 - 900 hPa	41	800 - 900 hPa	24	800 - 900 hPa	17
700 - 800 hPa	32	700 - 800 hPa	25	700 - 800 hPa	7
600 - 700 hPa	57	600 - 700 hPa	40	600 - 700 hPa	17
500 - 600 hPa	44	500 - 600 hPa	13	500 - 600 hPa	31
400 - 500 hPa	34	400 - 500 hPa	10	400 - 500 hPa	24
400 - 1000 hPa	224	400-1000 hPa	123	400 - 1000 hPa	101
15-Feb					
TOTAL		ICING		NO ICING	
900 - 1000 hPa	16	900- 1000 hPa	3	900 - 1000 hPa	13
800 - 900 hPa	49	800 - 900 hPa	10	800 - 900 hPa	39
700 - 800 hPa	37	700 - 800 hPa	5	700 - 800 hPa	32
600 - 700 hPa	83	600 - 700 hPa	16	600 - 700 hPa	67
500 - 600 hPa	40	500 - 600 hPa	6	500 - 600 hPa	34
400 - 500 hPa	19	400 - 500 hPa	2	400 - 500 hPa	17
300 - 400 hPa	6	300 - 400 hPa	4	300 - 400 hPa	2
300 - 1000 hPa	250	300-1000 hPa	46	300 - 1000 hPa	204
26-Jan					
TOTAL		ICING		NO ICING	
900 - 1000 hPa	9	900 - 1000 hPa	1	900 - 1000 hPa	8
800 - 900 hPa	9	800 - 900 hPa	5	800 - 900 hPa	4
700 - 800 hPa	14	700 - 800 hPa	4	700 - 800 hPa	10
600 - 700 hPa	19	600 - 700 hPa	11	600 - 700 hPa	8
500 - 600 hPa	10	500 - 600 hPa	2	500 - 600 hPa	8
400 - 500 hPa	11	400 - 500 hPa	1	400 - 500 hPa	10
400 - 1000 hPa	72	400 - 1000 hPa	24	400 - 1000 hPa	48

Table 2.1: PIREPs breakdown per vertical layer for each event investigated. A no icing report indicated that there was a report that icing was not present. Reports that did not include whether there was icing present are not included in this dataset. The highest percentage of icing reports occurred with the 6 Feb 2010 case, while the lowest percentage of icing reports occurred with the 15 Feb 2010 event.

2.4 Synoptic and Mesoscale Overview

We now consider the synoptic and mesoscale flow and precipitation patterns for the three events. Unless otherwise noted, all analyses are from the RUC, which have a 13-km grid spacing and are updated hourly.

The upper-level flow patterns at the midpoints of the events are provided in Fig. 2.6. All events have a deep trough over the eastern United States accompanied by a potential vorticity maximum aloft. In all cases, the trough is confluent, suggesting the systems are mature (Bluestein 1993). Considerations of the NAM-analyzed lower-level temperature fields show all systems are near occlusion (Fig. 2.7) – a favorable condition for the formation of a comma-head cloud. Additionally, each system tilts westward with height, from surface to 500-hPa geopotential level (c.f. Figs. 2.7 and 2.8).

The evolution of the precipitation systems according to the observed composite radar reflectivity mosaics is provided in Fig. 2.9. The 6 Feb event is characterized by the development of a coastal low over North Carolina while the primary low remains west of the Appalachian Mountains, even retrograding somewhat during the time frame shown (Fig. 2.9a-c). The 15 Feb event is more mobile, moving eastward about 100 km during the six hours shown (Fig. 2.9d-f). The surface low in the 26 Jan event is over Mississippi at 0000 UTC 26 Jan and moves northeast (Fig. 2.9g-i). By 0600 UTC 26 Jan, the low is over the Georgia/Alabama border. But, despite differences in the position and speed of the surface low in each event, all have broad comma-head precipitation zones whose highest reflectivities coincide with the areas of icing (Fig. 2.5). Also notice that the comma-head portions of the precipitation zones are stationary over Ohio (6 Feb), Indiana/Ohio (15 Feb), Kentucky/Tennessee (26 Jan). Additionally,

in Fig. 2.9, one sees clear examples of the transition from deep convection with heavy precipitation along the cold fronts to the relatively modest reflectivities in the comma-head regions. The reduced reflectivities in this part of the cloud system are not necessarily due to lessened precipitation rates, but are thought to be largely due to reduced radar returns for snowfall (Matrosov 1992).

All three events have many of the characteristics that have been found in conjunction with icing. More specifically, they all have regions of moderate to strong lifting, are close to saturation (as inferred from the $RH > 95\%$ contour), have cloud top temperatures ranging from 248 to 268 K, and have some portion of the cloud within the dendrite-growth zone (Fig. 2.10). The cross sections provided in Fig. 2.10 are parallel to the long axis of the comma-head precipitation systems. There are rather strong horizontal variations in the vertical velocity and in the height of the region of $RH > 95\%$ that are not evident via consideration of just one cross-sectional area (not shown). However, the above ingredients are present across most of the comma-head region.

Chapter 3

Comparison of Partially- and Fully-Double Moment Microphysical Parameterizations and Evaluation with PIREPs

Chapter 3 discusses the design of our experiments, including model specifications, lead times, and microphysical parameterizations employed in our investigations. Section 3.1 examines the microphysical parameterization specifics for each scheme considered in this research. Section 3.2, meanwhile, explores forecast differences between each of the microphysical parameterizations, both on a synoptic- and meso-scale, as well as individual hydrometeor fields. A comprehensive discussion on our evaluation techniques with PIREPs, and corresponding scoring methods, are included in Section 3.3.

3.1 Experimental Design

The experiments presented in this paper are conducted using the Advanced Research Weather and Forecasting Model (WRF-ARW), version 3.4 (Skamarock et al. 2008). The state-of-the-art WRF-ARW model was selected for our experiments because of its research and operational applications. Consistent with some of the goals of this paper, the WRF was designed to advance the understanding and prediction of mesoscale weather (in our case, microphysics scheme and relationship with aircraft icing) and accelerate the transfer of research advances into operational use. Additionally, the

WRF-ARW allows for prognostic calculations of cloud water and ice mixing ratios and permits both “simplified physics suitable for idealized studies to sophisticated mixed-phase physics suitable for process studies and NWP” (Skamarock et al. 2008). The model accommodates any number of mass mixing-ratio variables, and other quantities such as number concentrations, which was vital for our experiments.

For our experiments, the horizontal grid spacing is 4 km, with 51 vertical levels and 450 grid points in both the x and y directions. All parameterizations are similar to those used by the Rapid Refresh model, with the exception of the microphysical parameterizations and boundary layer parameterizations. The Rapid Refresh is the model that the FAA uses for their icing guidance. The parameterizations are the ‘Noah’ land surface model (Ek et al. 2003), the Mellor-Yamada-Janjić boundary layer (Janjić 2002), the Dudhia shortwave radiation scheme (Dudhia 1989), and the Rapid Radiative Transfer Model (RRTM; Mlawer et al. 1997) longwave radiation scheme. No convective parameterization is employed. The initial and boundary conditions are given by the 12-km NAM analyses and forecasts, respectively. The model runs are initialized at 1800 UTC 5 Feb 2010, 0600 UTC 15 Feb 2010, and 1800 UTC 25 Jan 2011, for each case. This gives each experiment a 6-h period to spin up precipitation. Our attention will be focused on the 6-h periods cited in section 2.3.

The Rapid Refresh model uses the Thompson microphysical parameterization scheme. The TSON was originally developed with the intent to improve explicit prediction of aviation icing, and, therefore, it applies sophisticated formulations of mixed-phase processes. This scheme is known to sustained SLW at temperatures less than 253 K than other schemes (Thompson, personal contact). However, the scheme is

also known to be overly efficient at scavenging out SLW by snow in convective winter weather (Thompson, personal contact). The depletion of SLW by snow may be a consequence of the assumed size distribution of snow, which is strongly weighted toward small particles. A scheme that is double moment with respect to snow may not have this bias because it allows for a variable drop size distribution at each grid point. Hence, in those parts of the cloud that are dominated by large snowflakes, such as in the dendrite growth zone, the scavenging of SLW may be more conservative. The relation between snow and cloud water has been shown to be particularly sensitive with TSON (Thompson et al. 2004, 2008; Nygaard et al. 2011), and, as such, further investigation into the codependency will be explored.

Four different microphysical parameterizations are compared. The schemes considered in this investigation are the Thompson, the Morrison (MORR; Morrison et al. 2008), Milbrandt-Yau (MY; Milbrandt and Yau 2005), and the National Severe Storms Laboratory (NSSL; Mansell et al. 2010) schemes. The parameterizations included in this study are chosen because they provide a variety of calculated mass and number categories, which represent many schemes being operationally employed or researched at this time. Additionally, all the schemes considered account for mixed-phase processes, which are those that result from the interaction of ice and water particles, such as riming that produces graupel or hail. With the grid spacing set at 4-km, mixed-phase schemes should be used for convective or icing situations (Skamarock et al. 2008), both of which are common in the comma-head regions of extratropical cyclones.

Table 3.1 shows the hydrometeor categories and number of moments for each parameterization.

MP Scheme	Core	Mass Categories	Number Categories	No. of Moments
TSON	ARW/NMM	<i>c, i, s, r, g</i>	<i>i, r</i>	2 for <i>r</i> and <i>i</i> , 1 all else
MORR	ARW (Chem)	<i>c, i, s, r, g</i>	<i>i, r, s, g</i>	2 for <i>i, r, s</i> , and <i>g</i> , 1 for <i>c</i>
MY	ARW	<i>v, c, i, s, r, g, h</i>	<i>v, c, i, s, r, g, h</i>	2
NSSL	ARW	<i>v, c, i, s, r, g, h</i>	<i>v, c, i, s, r, g, h</i>	2

Table 3.1: Bulk microphysical parameterization descriptions for the schemes investigated in this paper. Vapor is denoted by *v*, cloud water by *c*, ice by *i*, snow by *s*, rain by *r*, graupel by *g*, and hail by *h*. [Note that TSON and MORR are only partially-double moment scheme, while MY and NSSL are all fully-double moment schemes.]

In TSON, for the cloud water, vapor, snow and graupel, only the mixing ratios of hydrometeors are predicted. For those categories that are double-moment, both mixing ratios and number concentrations of species are predicted. The advantage of a double-moment scheme is that the size distribution is not fixed; this allows for size sorting and the differential transport of large versus small hydrometeors.

The NSSL scheme was designed to perform optimally for convection-permitting experiments, in part through predicting the average graupel density at each grid point. This approach allows for a range of graupel densities, which, in turn, may lead to a greater scavenging of SLW in some parts of the cloud. The MY microphysical parameterization, like NSSL, has a category for hail and, hence, is a seven-class microphysics scheme. The number concentrations are predicted for all seven water and ice species, which is important for parameterization of the individual microphysical interactions and processes. Additionally, MY employs a variable shape parameter

utilized in the three-parameter gamma distribution function that is diagnosed based on the number of predicted moments. This variable spectral shape parameter is based off observations by Uijlenhoet (2003), who showed that for a squall line, the raindrop spectra can vary significantly between the stratiform and convective phases. We speculate that this variable spectral width may allow for notable gradients in the size spectra of the hydrometeors between the convective and non-convective portions of the comma-head, which may result in more highly-localized hydrometeor mixing ratios. Meanwhile, MORR has prognostic variables for graupel mixing ratio and the number concentrations are predicted for ice, snow, rain, and graupel, and cloud water. However, the WRF version utilized in these experiments does not employ two-moment cloud liquid water. Not having the number concentration predicted for cloud water, as in TSON, may limit the differentiation between large and small cloud droplets, and, thus, cause a more conservative representation of cloud water. However, MORR is included in this study because the scheme has been extensively tested in both idealized and real cases that cover a wide range of conditions, which can be present in environments conducive to hazardous aircraft icing.

3.2 Control Experiments and Comparison of Partially- and Fully-Double Moment Forecasts

There are no notable differences in the forecasts of synoptic-scale flow patterns among the different experiments for each event. The mean sea-level pressure fields and 2-m temperature fields are nearly identical for each event on a scheme-to-scheme basis. (Figs. 3.1 - 3.3). Additionally, scheme-to-scheme comparisons of the 500-hPa

geopotential fields are similar as well (Figs. 3.4 – 3.6), but analysis of the forecasts for the 15 Feb event shows discrepancies. In comparing Fig. 3.6a to Fig. 3.6b-e, differences are present in the depth and intensity of the 500-hPa closed low. This inconsistency leads to questions of model initialization errors, but the differences appear to be relatively minor. Therefore, such a discussion is not included in this paper, and, hence, our comparison begins with consideration of the precipitation patterns (comparisons of precipitation patterns and microphysics processes would be meaningless if synoptic-scale forecasts varied on a scheme-to-scheme basis). The maximum column reflectivities for each experiment at 0300 UTC 6 Feb 2010 are seen in Fig. 3.7. These figures can be compared to Fig. 2.7b. All of the schemes have higher reflectivities in the comma-head region than is observed. The forecasts also extend the radar returns farther west into central Missouri, whereas in the observations, this area has no precipitation. The tendency for the experiments to overpredict the reflectivities is also seen in the other case studies. For example, the 26 Jan event forecasts overpredict the reflectivity by 10 to 15 dBZ. (c.f. Fig. 3.8, Fig. 2.7h). Similarly, the 15 Feb event forecasts have maximum reflectivities ranging from 25 to 35 dBZ (Fig. 3.9) in the comma-head region, while the observations show reflectivities from 15 to 25 dBZ (Fig. 2.7e). The apparent overprediction of reflectivity may be partly a consequence of poor sampling by radars in winter storms. Precipitation systems in winter tend to be shallower than their warm-season counterparts (Bluestein 1993). Hence, the farther away from a radar one gets within a storm, the more likely the radar beam is to overshoot the level of maximum hydrometeor growth. As all experiments are similar in regards to overpredicting reflectivity, we will examine it no further.

There are some noteworthy scheme-to-scheme differences. In all of the events, the region of reflectivity exceeding 20 dBZ is considerably smaller in the NSSL experiment than in the others. Because snow is the primary form of precipitation in all three events, and the NSSL scheme tends to produce less snow than other parameterizations (Mansell¹, personal contact), the weaker reflectivities noted in NSSL may be attributed to the fact that NSSL employs a volume-based assumed snow size distribution gamma function (opposed to diameter-based). Even though NSSL does not produce snow via ice crystal aggregation, snow growth from aggregation is not considered to be a reason for the discrepancies. These differences are even more apparent in the column-integrated precipitation mass (P_i) and are seen in Figs. 3.10 – 3.12. This quantity is based on the model predictions of rain water (q_r), snow (q_s), and graupel (q_g) at each level. The area with P_i greater than 0.3 mm is significantly smaller in NSSL for the 6 Feb event (Fig. 3.10). The same is true on 26 Jan (Fig. 3.11). In the 15 Feb event, the spatial coverage is similar, but the maxima are not (Fig. 3.12). The NSSL scheme has maxima ranging from 1.2 to 1.5 mm, while the other schemes have maxima ranging from 2.1 to 2.4 mm. These discrepancies may be attributed to the NSSL scheme's ice nucleation parameterization utilized by NSSL (from Ferrier 1994). Changing this parameterization to an approach similar to that used in TSON produces similar reflectivities and P_i as the other parameterizations.

Despite the differences in reflectivity and P_i , the 6-h liquid equivalent precipitation distributions are remarkably similar. The event on 6 Feb has the heaviest precipitation over Ohio and West Virginia with a secondary maximum over southeastern Missouri (Fig. 3.13). The maximum values are indicated and are similar in

magnitude in all experiments. The 26 Jan event has nearly uniform accumulations with maxima ranging from 6 to 7 mm over west central Tennessee and Kentucky (Fig. 3.14). Lastly, on 15 Feb the distributions in maxima are again very similar in all experiments (Fig. 3.15). Even though accumulations from NSSL are lower than in the other experiments, differences are very subtle. Again, this appears to be due to the choice to use a volume-based snow distribution in the NSSL scheme, but further investigation is not considered here.

Before investigation of the partitioning of hydrometeors from scheme to scheme, it is reasonable to first consider individual meso- and cloud- scale processes responsible for precipitation production. One kinematic parameter worth investigating is vertical motion within the comma-head portion of the cyclones. Fig. 3.16 shows vertical velocity, temperature (only the 265 to 269 K ranges contoured), and $RH > 95\%$ at 700-hPa at 0300 UTC 6 Feb. The superposition of upward vertical motion, in the region between 265 K and 269 K and $RH > 95\%$, is conducive to hazardous icing conditions (McDonough and Wolff, 2004). It can be seen that the largest vertical motions correlate well with the regions of highest forecasted liquid equivalent precipitation (c.f. Fig. 3.16, Fig. 3.13). This collocation of favorable upward motion, thermal, and moisture parameters in the comma-head region are also noted in Fig 3.17 for 26 Jan 2011. However, in Fig. 3.18, for the 15 Feb event, the temperature profile near the 700-mb level fell below the range considered to be a high threat for icing (McDonough and Wolff, 2004). However, it is important to note that temperatures below this range (not contoured in Fig. 3.18), in conjunction with other parameters, may still produce a hazardous icing environment. However, there are very little scheme-to-scheme

differences in the thermodynamic and kinematic fields shown across the comma-head portions of each of the cyclones.

Let us now consider cloud water mixing ratio (q_c). Because each event's vertical extent is all almost entirely below 273 K (with the exception of 26 Jan at low altitudes), q_c directly corresponds to the amount of supercooled liquid water (SLW). Vertical cross-sections taken parallel to the long axis of the comma-head precipitation system (as indicated in Figs. 3.7a, 3.8a, and 3.9a) for 6 Feb, 26 Jan, and 15 Feb, respectively, are seen in Figs 3.19 - 3.21. The cross-sections show q_c (g/kg) and the θ_e (K) field. For the 6 Feb event (Fig. 3.19), clearly considerable differences exist from scheme to scheme. The TSON scheme forecasts less SLW in the comma-head region, with maxima in the mixing ratio near 0.16 g/kg, compared to 0.20 g/kg for NSSL, 0.27 g/kg for MY, and 0.21 g/kg for MORR for one localization of SLW. There is a secondary area of enhanced q_c with maxima of 0.14g/kg, 0.20 g/kg, 0.26g/kg, and 0.21 g/kg for TSON, NSSL, MY and MORR, respectively. This difference in q_c between the schemes is apparent for each event. For example, in Fig. 3.20, there is a significant discrepancy not only between the local q_c maxima, but also the spatial coverage of the SLW. All schemes, except TSON, have an extensive area of q_c across the middle of the cross-section through the comma-head. Forecast q_c maxima in this area range from 0.06 g/kg in TSON, to 0.16 g/kg, greater than 0.28 g/kg, and 0.18 g/kg for NSSL, MY, and MORR, respectively. A similar spatial discrepancy is seen in Fig. 3.21 for 15 Feb. The TSON maximum (0.14 g/kg) is again much lower than those forecast by NSSL, MY, and MORR. It is evident that the forecasts of q_c in many of our investigations have a cellular nature, suggesting convection may be a factor in the production and

maintenance of cloud water within the comma-head region. Such an observation leads to questions on the choice and employment of cumulus parameterizations, but such an exploration is not included in this study.

While it is clear that differences are present between the forecasts of q_c through the long axis of the comma-head, the discrepancies in local maxima for TSON are not quite as apparent when summed through the entire comma-head precipitation system. Fig. 3.22 shows the forecast time series of volume-integrated q_c , q_s , and the total hydrometeor mixing ratio, the sums of q_c , q_r , q_g , q_i , and q_s , for the comma-head precipitation system for 6 Feb. The volume used is given by the dashed parallelogram in Fig. 3.7a. The extent of influence of q_s on q_c , and their codependency is described at length in Chapter 4. However, in Fig. 3.22a, the sum of q_c for TSON, while low, is very comparable to that of NSSL and MY. While the forecast q_s for TSON is higher than NSSL and MORR (Fig. 3.22b), the total hydrometeor mixing ratio (q_t) is also very comparable (3.22c). This relationship also holds true for 26 Jan (Fig. 3.23), which is given by the area dashed in Fig. 3.2a. For the 15 Feb event (see Fig. 3.9a), despite a higher q_c than the other parameterizations (Fig. 3.24a), NSSL shows a discrepancy in q_s (Fig. 3.24b). This discrepancy may be a consequence of the fact that NSSL does not produce snow via ice crystal aggregation, and is known to produce less snow than other parameterizations (Mansell, personal contact). However, for TSON, despite the apparent deficiencies in q_c along the cross-section through the comma-head (c.f. Figs. 3.19a 3.20a and 3.21a), the summations of q_c for all three events are not as distinct. This could be attributed to more widespread, but lower maxima q_c across the comma-head region for TSON. However, high values of q_c has been shown to be more hazardous for

aircraft icing than low-magnitude widespread SLW (Politovich 1988; Schultz and Politovich 1992; Reisner et al. 1998; Bernstein et al. 2005).

3.3 Evaluation of Parameterization Forecasts With PIREPs

To fully assess the forecasts of each microphysical parameterization, it is vital to evaluate the solutions against some known measurement, which we chose to be PIREPs. It has been well established that not only are icing conditions a major hazard to the aviation industry, but that PIREPs can be useful tools to evaluating NWP model forecasts (Guan et al. 2001; Politovich 2003; Bernstein et al. 2005). Through the years, there have been many proposed parameters for diagnosing icing conditions, such as SLW, cloud top temperature, median droplet diameter, and relative humidity. There exists a spread in these commonly-accepted parameters predominantly because each parameter threshold is applicable to different aircraft types, altitudes, and individual pilot practices. Despite these discrepancies, the most common threshold used for assessing conditions favorable for icing is the amount of SLW (from q_c) present in the cloud. The presence of SLW is controlled by the temperature profile, moisture advection, uplift strength, duration over which upward vertical motion occurs, aerosol and precipitation particles, and ambient moisture (Taffermer et al. 2003). Such a method for evaluation is employed here and is described below.

The latitudes, longitudes, altitude and times for each icing/no icing report are recorded for 6-h periods (cited in section 2.3) for each event. The latitudes, longitudes, and altitude are directed to the nearest horizontal and vertical grid point, respectively.

Surrounding this assigned grid point, a hypothetical envelope is created for each aircraft location at the time of the report. This envelope extends 50 hPa above and below the aircraft altitude, as well as 16.11 km on each of the four sides of the aircraft. The horizontal extent of the envelope was specified by the FAA Airport and Aircraft Safety / Research and Development Icing Design Envelope Specification Final Report in April, 2002. A visual representation of the dimensions of each envelope is provided in Fig. 3.25.

Within each envelope, a maximum value for cloud water mixing ratio is found and recorded. If the maximum value exceeds the given threshold, then the particular aircraft is deemed to be flying in forecasted conditions favorable for icing. If the maximum value fails to meet the given threshold, then the scheme forecast is not favorable for aircraft icing. These envelopes are then compared to the aircraft report (observed), which is assumed to be truth. Because each envelope corresponds to each icing/no icing report, this process is repeated for each report time, for each of the three events. The statistics are then tallied and are compared to each corresponding icing/no icing report.

The evaluation of the microphysical parameterization scheme forecasts are performed using multiple skill score parameters. These parameters have been well-established in giving each forecast a number score, based on the format described in Table 3.2.

Microphysical Parameterization Scheme		Observed	
		Yes	No
Forecasted	Yes	Hit	False Alarm
	No	Miss	Correct Null

Table 3.2: Skill Score tally format. A scheme forecast maximum q_c value above set threshold indicates a “yes” forecast, while a scheme forecast maximum q_c value that fails to meet such threshold indicates a “no” forecast. The observed statistics are the individual PIREPs reports, which are assumed to be truth.

From Table 3.2, we see that the highest scores will be computed from higher tallies along the diagonal (i.e. more “hits” than “misses” and more “false alarms” (FAs) than “correct nulls” (CNs).) The first q_c threshold is set to 0.025 g/kg. Thus, any q_c value higher than 0.025 g/kg within an particular envelope is given a “yes” forecast. Any envelope void of a maximum value above 0.025 g/kg is given a “no” forecast. The threshold of 0.025 g/kg was not chosen arbitrarily. The threshold was lowered and raised several times to test the sensitivity of the scores to the threshold. While threshold changes did affect some skill parameters, the overall skill scores were not greatly affected. Additionally, the same scheme-to-scheme tendencies were still evident. The skill score statistics for each of the events are summarized in Table 3.3.

6-Feb-10				26-Jan-11				15-Feb-10			
TSON		Observed		TSON		Observed		TSON		Observed	
		Yes	No			Yes	No			Yes	No
Forecast	Yes	56	31	Forecast	Yes	16	12	Forecast	Yes	6	22
	No	67	70		No	8	36		No	40	182
NSSL		Observed		NSSL		Observed		NSSL		Observed	
		Yes	No			Yes	No			Yes	No
Forecast	Yes	63	38	Forecast	Yes	18	23	Forecast	Yes	9	39
	No	60	63		No	6	25		No	37	165
MY		Observed		MY		Observed		MY		Observed	
		Yes	No			Yes	No			Yes	No
Forecast	Yes	78	43	Forecast	Yes	17	23	Forecast	Yes	10	51
	No	45	58		No	7	25		No	36	153
MORR		Observed		MORR		Observed		MORR		Observed	
		Yes	No			Yes	No			Yes	No
Forecast	Yes	72	42	Forecast	Yes	18	23	Forecast	Yes	11	35
	No	51	59		No	6	25		No	35	169

Table 3.3: Number of hits, misses, false alarms (FAs), and correct nulls (CNs) for each event. For 6 Feb, there are 224 reports between 0000 UTC and 0600 UTC, which include flight paths across central and southern Illinois, central and southern Indiana, and central and southern Ohio. For 26 Jan, there are 72 reports between 0000 UTC and 0600 UTC, which include flight paths across northern Mississippi, western and central Tennessee, and western and central Kentucky. For 15 Feb, there are 250 reports between 1200 UTC and 1800 UTC, which include flight paths across central and southern Indiana, central and southern Ohio, and northern Kentucky.

In Table 3.3, the forecasts of NSSL, MY, and MORR are markedly better than those of TSON for 6 Feb. Even though TSON had more correct nulls (CNs), the absence of

prediction of cloud water has been shown to not be conclusively indicative of an environment void of icing (Reisner 1998; Thompson et al. 2004). NSSL, MY, and MORR have more hits than misses, as well as more CNs than false alarms (FAs). While there are more FAs in MY and MORR, there are also more hits than misses for those parameterizations, when compared to those of NSSL. Meanwhile, TSON forecasts had the fewest hits and most misses of any microphysical parameterization, as well as more overall no forecasts, most likely attributed to the overall lower q_c fields. Meanwhile for 15 Feb, for all four microphysical parameterizations, there are more misses than hits. At first glance, it is evident that none of the four microphysical parameterizations evaluate well with the 15 Feb case. The number of no forecasts for each scheme is markedly higher than the number of yes forecasts. Because this trend is noted in a scheme-to-scheme comparison, we determine that perhaps such poor scores can be attributed to the event itself, and not necessarily parameterization performances. Each parameterization forecast of the 15 Feb event does differ slightly from the NAM-ANL (see Figs. 3.4 – 3.6), suggesting the storm was a difficult forecast. Nevertheless, once again, TSON had the fewest number of yes forecasts of any scheme. This trend is also seen in the forecasts for 26 Jan. However, for this event, the number of yes forecasts in TSON are not drastically lower than those of NSSL, MY, or MORR. It is noteworthy that all four microphysical parameterizations evaluated well with PIREPs for 26 Jan, especially in comparison to 15 Feb. Table 3.4 below shows the same statistics as Table 3.3, but normalized to the total number of reports.

6-Feb-10				26-Jan-11				15-Feb-10			
TSO		Observed		TSO		Observed		TSO		Observed	
		Yes	No			Yes	No			Yes	No
Forecast	Yes	0.25	0.14	Forecast	Yes	0.22	0.17	Forecast	Yes	0.02	0.09
	No	0.30	0.31		No	0.11	0.50		No	0.16	0.73
NSSL		Observed		NSSL		Observed		NSSL		Observed	
		Yes	No			Yes	No			Yes	No
Forecast	Yes	0.28	0.17	Forecast	Yes	0.25	0.32	Forecast	Yes	0.04	0.16
	No	0.27	0.28		No	0.08	0.35		No	0.15	0.66
MY		Observed		MY		Observed		MY		Observed	
		Yes	No			Yes	No			Yes	No
Forecast	Yes	0.35	0.19	Forecast	Yes	0.24	0.32	Forecast	Yes	0.04	0.20
	No	0.20	0.26		No	0.10	0.35		No	0.14	0.61
MORR		Observed		MORR		Observed		MORR		Observed	
		Yes	No			Yes	No			Yes	No
Forecast	Yes	0.32	0.19	Forecast	Yes	0.25	0.32	Forecast	Yes	0.04	0.14
	No	0.23	0.26		No	0.08	0.35		No	0.14	0.68

Table 3.4: Confusion matrix normalized to total number of reports per case. Each number represents the percentage of forecasts per report.

As indicated in Table 3.4, TSON did have the lowest number of false alarms of any scheme for both 26 Jan and 15 Feb. However, given the bias of PIREPs to report positive icing, the false alarms are not considered to be as important a parameter as the hits (Brown et al. 1997). Additional skill set parameters, such as probability of detection (POD), overall accuracy, bias, and false alarm ratio (FAR), are shown in Table 3.5.

Event	MP	POD: 1	Accuracy: 1	Bias: 1	FAR: 0
6-Feb	TSON	0.4553	0.5625	0.7073	0.3563
	NSSL	0.5122	0.5625	0.8211	0.3762
	MY	0.6341	0.6071	0.9873	0.3554
	MORR	0.5854	0.5848	0.9286	0.3684
26-Jan	TSON	0.6667	0.7222	1.1677	0.4286
	NSSL	0.7500	0.5972	1.7083	0.5610
	MY	0.7083	0.5833	1.6667	0.5750
	MORR	0.7500	0.5972	1.7083	0.5610
15-Feb	TSON	0.1304	0.7520	0.6087	0.7857
	NSSL	0.1957	0.6960	1.0435	0.8125
	MY	0.2174	0.6520	1.3261	0.8361
	MORR	0.2391	0.7200	1.0000	0.7609

Table 3.5: Skill statistics for each event and microphysical parameterization. A perfect POD score, and accuracy score is 1, while an “unbiased” forecast also receives a score of 1. Bias scores over 1 indicate an over-forecast, while scores below 1 indicate an under-forecast. A perfect FAR score is 0.

According to both Tables 3.4 and 3.5, the 26 Jan event was forecasted well by most parameterizations. However, parameterization forecast scores for 15 Feb are much weaker. It can be seen in Table 3.5 that for 6 Feb, the MY scheme forecasts received the highest scores for all parameters. Meanwhile, TSON received the poorest scores in POD, accuracy, and bias. However, for 26 Jan, TSON had the best accuracy, bias, and FAR. Like in the 6 Feb event, TSON received the lowest POD and worst bias for 15 Feb. MORR, on the other hand, had the highest POD and FAR and the best bias. However, given the bias of PIREPs to report positive icing, FA is not considered to be as important a parameter as the hits (Brown et al. 1997). In fact, icing forecasts that have a hit POD also have a correspondingly high FAR (Tafferner et al. 2003).

The score parameters described in Table 3.5 are not treated equally when evaluating the overall performance of a particular forecast. As mentioned, the FAR is not considered as important as the probability of detection, just as the accuracy is strongly weighted toward the number of icing or no icing reports. In order to quantify “how well” each microphysical parameterization forecast compared to PIREPs, specific skill scores are computed for each scheme and each case. The “skill” in these scores refers to a forecast that is superior to some reference forecast (i.e. random chance/guess). These three individual skill scores are frequently used to evaluate NWP solutions, as well as watch and warning verification for the National Weather Service (NWS). The NWS uses skill scores for watch and warning verification, specifically for rare events such as tornadoes, flash floods, and high wind events. Skill scores help assess the quality of the forecast by eliminating contributions to the scores that may be due to random chance. Many scores are derived so that a comparison of forecasts can be made across different environments (i.e. for tornado warning verification, scores are directly comparable whether a given region is prone to tornadoes, like Oklahoma, or not prone, like Alaska). Thus, forecasts are directly comparable for a given group of forecasters across different climates, and microphysical parameterization forecasts can be compared across regions whether icing is prone to occur or not. For these scores considered here, a perfect score is 1, while a reference/guess forecast score is 0.

The first skill score utilized to evaluate the parameterization forecasts is called Heidke’s Skill (Heidke 1926). In Heidke’s score, 0 indicates an anti-skill. Heidke’s skill is based on the Heidke hit proportion, which reflects discrimination, reliability, and resolution. The Heidke formulation is used commonly in meteorology since it uses all

elements in the confusion matrix and works well for rare event forecasting (i.e. tornadoes or aircraft icing conditions.) The TSS measures the fractional improvement over random chance and is usually used to score multi-category events. TSS is defined by

$$\text{Heidke's Skill} = \frac{2 * [(\text{Hits} * \text{CNs}) - (\text{FAs} * \text{Misses})]}{[(\text{Hits} + \text{FAs}) * (\text{Misses} + \text{CNs})] + [(\text{Hits} + \text{Misses}) * (\text{Misses} + \text{CNs})]} \quad (3.1)$$

and scores for each event and microphysical parameterization are summarized in table 3.6.

The second skill score employed to evaluation the microphysical parameterization forecasts is the Hanssen-Kuipers Skill Score (H-K / TSS Skill; Hanssen and Kuipers 1965). The H-K Skill is computed by

$$\text{H - K Skill} = \left[\frac{(\text{Hits} * \text{CNs}) - (\text{Misses} * \text{FAs})}{(\text{FAs} + \text{CNs}) * (\text{Hits} + \text{Misses})} \right] \quad (3.2)$$

H-K, or True Skill Score (TSS), measures the ability of a forecast to separate yes cases from no cases, with 0 indicating anti-skill. H-K Skill has an advantage over Heidke's because TSS has a contribution made to the score by a correct yes or no forecast that increases as the event is more or less likely, respectively. Therefore, in theoretical terms, a forecaster is not discouraged from forecasting a rare event on the basis of the rare event's low climatological probability. TSS incorporates random correct forecasts that are constrained to be unbiased. TSS has some desirable characteristics for evaluating rare event forecasts, such as aircraft icing. For example, both random forecasts and constant forecasts receive a score of 0. Additionally, the contribution to this score for a correct no forecast (correct null) increases as the event becomes more likely, while the contribution for a correct yes forecast (hit) increases as the event becomes less likely. On the contrary, TSS does express the hit rate relative to

the FAR, so it will remain positive as long as there are more hits than false alarms. The TSS are summarized in Table 3.6.

The last skill score utilized to evaluation the forecasts is the Gilbert Skill Score (GSS; Gilbert 1884), which is described by

$$GSS = \left[\frac{Hits - \frac{(Hits+Misses)(Hits+FA_s)}{n}}{Hits - \frac{(Hits+Misses)(Hits+FA_s)}{n} - Misses + FA_s} \right] . \quad (3.3)$$

GSS is often called the “Equitable Threat Score.” GSS is dependent on the sample size, n , so the score is a function of the number of no correct forecasts; a GSS score of $-1/3$ indicates no skill. This skill score measures the fraction of observed and/or forecasted events that are correctly predicted, adjusted for the frequency of hits that would be expected to occur simply by random chance (i.e. it is easier to forecast rain in a wet climate than in a dry climate). GSS is often used in the verification of rainfall in NWP models because its “equitability” allows scores to be compared more fairly across different regimes; however the score is not truly equitable. GSS is sensitive to hits, and because it penalizes both misses and false alarms in the same way, it does not distinguish the source of the forecast error. It should be used in combination with at least one other contingency table statistic (i.e. bias). The GSS for each event is summarized in Table 3.6.

Event	MP Scheme	Heidke's Skill: -1	Hanssen-Kuipers's Skill: -1	Gilbert's Skill: -1/3
6-Feb	TSON	0.1438	0.1484	0.5242
	NSSL	0.1334	0.1360	0.5937
	MY	0.2080	0.2084	0.7794
	MORR	0.1682	0.1695	0.6994
26-Jan	TSON	0.4000	0.4167	0.5903
	NSSL	0.2301	0.2708	0.5313
	MY	0.1964	0.2292	0.4965
	MORR	0.2301	0.2708	0.5313
15-Feb	TSON	0.0266	0.0226	0.0943
	NSSL	0.0044	0.0045	0.1168
	MY	-0.0290	-0.0326	0.1152
	MORR	0.0676	0.0676	0.1502

Table 3.6: Skill Scores for 6-h periods for each event and each microphysical parameterization scheme. For each skill score considered, a score of 0 indicates a forecast that is equal to a reference forecast, while a score of 1 indicates a perfect forecast. However, Heidke's skill and TSS scores of -1, and a GSS score of -1/3 indicates a poor forecast.

In Table 3.6, there are drastic differences in the final skill scores across events and schemes. For the 6 Feb event, MY scores the highest in all three skill scores, while NSSL scores the lowest for TSS and H-K, while TSON has the lowest GSS. However, the overall skill scores for all four microphysical parameterizations for the 6 Feb event are superior to those for 15 Feb. In fact, many of the scores for 15 Feb are either below 0 (worse than a reference forecast or guess), or very close to 0 (very little improvement over a reference forecast). These poor skill scores are parameterization independent; nevertheless, MORR forecasts, although poor, do appear to be better than those of the

other parameterizations. Meanwhile, the skill scores for 26 Jan are quite similar to those for 6 Feb. Each microphysical parameterization forecast shows a marked advantage over that of a reference forecast. However, it is noteworthy that TSON forecasts receives the highest Heidke's, TSS, and GSS for all three skills. However, MORR forecasts had the highest overall average of each of the three skill scores for the three cases.

Table 3.6 shows that perhaps the ability to accurately depict favorable icing conditions in a forecast is more event-driven than microphysical parameterization-dependent. This is particularly evident for the 15 Feb case. However, such a statement cannot be universally applied given the small dataset. Further investigation utilizing data from more comma-head snow events, as well as more parameters for icing, would be necessary to make an outright conclusion on the ability of microphysical parameterizations to accurately forecast aircraft icing conditions.

Chapter 4

Thompson Microphysical Parameterization Sensitivity Tests

Chapter 4 explores the specifics of individual microphysics processes utilized in the Thompson (TSON) partially-double moment scheme. Section 4.1 examines hydrometeor tendencies in TSON, including size distributions, and the corresponding hypothetical effects on forecasts of individual hydrometeor budgets. Section 4.2 explores a function in the TSON source code responsible for scavenging of cloud water by snow, while Section 4.3 considers individual snow parameters and their direct effects on the maintenance of cloud water within the scheme. Within Section 4.3, the effective bulk density, shape, and capacitance of snow are examined and forecasts of sensitivities are compared to forecasts of the control run. Meanwhile, Section 4.4 discusses the prescribed cloud droplet density utilized in BMPs, and the sensitivity of the concentration on the maintenance of cloud water.

4.1 Thompson Microphysics Processes

The TSON scheme, currently utilized in the Rapid Refresh model employed by the FAA, showed some discrepancies in forecasts of q_c from the other parameterizations considered. Because the TSON scheme is used to make aircraft icing forecasts, and there are established tendencies of TSON to under-produce SLW (Thompson et al. 2008; Nygaard et al. 2011), it is logical to inquire and investigate the individual microphysics processes for TSON specifically. Additionally, TSON, a partially double-

moment scheme, was designed specifically to improve aircraft icing forecasts (Thompson et al. 2008). Even though MORR is also partially-double moment, the scheme is not used operationally for aircraft icing and was not found to underpredict SLW.

The TSON forecasts of q_c were found to be unique from those of the fully-double moment parameterizations, particularly along the comma-head cross-sections. The volume-integrated time series of cloud water mixing ratio, while not an outlier in TSON, was still lower than the overall scheme averages for each event. Despite a high horizontal variability in both the kinematic fields and the SLW, the TSON solutions of q_c cannot be discounted. Because each parameterization is highly sensitive to the balance between cloud water, cloud ice, snow, and graupel, we hypothesize that perhaps a subtle change to this intricate balance would allow SLW to be sustained in TSON.

In TSON, the cloud water is handled via a gamma distribution with a shape factor that is dependent on droplet concentration. The cloud water is not allowed to sediment, and autoconverts to rain using a formulation described by Berry and Reinhardt (1974). Cloud water content is stored in lookup tables. The cloud ice, like cloud water, is also controlled by a gamma distribution, while the snow is managed by the sum of two gamma distributions from Field et al. (2005). According to Thompson et al. (2008), this combined function accounts for the frequently observed super-exponential number of small particles as well as the general slope of the large particles. In this combined function, the y-intercept parameter, which is often problematic for microphysics schemes, depends on both the snow mixing ratio and the temperature. The size distribution for snow depends on ice content and temperature, and maintains a non-

spherical geometry, unlike many other microphysical parameterizations. The density is variable and is inversely proportional to the diameter, which differs from many other schemes, which assume a constant snow density. TSON also employs a variable collection efficiency for rain-, snow-, and graupel-collecting cloud droplets. The growth of snow is governed by vapor depositional growth onto cloud ice particles until those ice crystals grow beyond the arbitrary threshold of 200 μm (Pruppacher and Klett 1997). This threshold is also utilized in MORR and is approximately the size threshold for known detectability limits of 2-D cloud probes (Thompson et al. 2008). Finally, terminal velocities of snow are constant, in line with vertically-pointing Doppler radar data and observations described by Mitchell and Heymsfield (2005).

The rain, cloud ice, and graupel mixing ratios in TSON for each of the events was found to be trivial in comparison to both the cloud water and snow fields. Sensitivity tests involving graupel and cloud ice were found to have nearly negligible effects on the cloud water field and snow field, suggesting a relatively minor contribution to the microphysics processes made by the Wegener-Bergeron-Findeisen effect (Wegener 1911; Bergeron 1935; Findeisen 1938). The minor role of the Wegener-Bergeron-Findeisen process in mixed phase clouds is consistent with the findings of Korolev (2006), which found that the process only occurs under a limited range of conditions and that ice particles and cloud water do not always evolve via the method described by the Wegener-Bergeron-Findeisen effect. As such, we hypothesize that in TSON, the cloud water and the ice particles are competing for water vapor, instead of ice particles growing at the expense of cloud water, via evaporation of the cloud water into vapor. However, due to the low cloud ice mixing ratios in TSON for

each event, further discussion on the effects of cloud ice and cloud water are not explored here.

4.2 Collection Efficiency of Snow From Cloud Water

To determine the q_c deficiencies seen in TSON, with respect to the fully-double moment schemes, a series of sensitivity tests are run to qualify such differences. It was quickly determined that the SLW was being scavenged by snow. This codependency between q_c and q_s is the foundation for the sensitivities explored here. From Thompson et al. (2008), the rate of snow collecting cloud water is defined by

$$\text{prs_scw}(k) = \rho f(k) * t1_qs_qc * Ef_sw * rc(k) * smoe(k) \quad , \quad (4.1)$$

where $\rho f(k)$ is a thermodynamic variable defined by

$$\rho f(k) = \sqrt{\frac{1.185}{\rho(k)}} \quad . \quad (4.2)$$

The rate is a function of $t1_qs_qc$ (a constant equal to $10*\pi$), the collection efficiency (Ef_sw), moisture tendency for cloud water (rc), and $smoe$, a variable used for riming. The collection efficiency of snow from cloud droplets in TSON, unlike most other BMPs, is a variable function, per the findings of Wang and Ji (2000). The collection efficiency is dependent upon the Stokes number and is derived from lookup tables of collections, but is based on the median volume diameter of snow and cloud water (Wang and Ji 2000) and is defined by

$$Ef_sw = \frac{(yc0+p)^2}{(1.+p)^2} \quad . \quad (4.3)$$

Here, Ef_{sw} is dependent upon the difference between the terminal fall speeds and fall speed power relations of snow and cloud water, which is crucial for the glaciation rates (Larson and Smith 2009). This variable function equates the melted snow diameter to their “effective collision cross-section” (Thompson et al. 2008). The collection efficiencies are precomputed based on broad-branched snow crystals at the start of the simulation and are stored in a lookup table (Thompson et al. 2008). We hypothesize that the collection efficiency in TSON, denoted by Ef_{sw} , is too efficient. This variable collection efficiency is reduced to 50% of the original variable function to test the effect of the collection efficiency on q_c . This test is referred to as EFSW. The control runs of TSON are hereby indicated by CTRL.

Forecasts of maximum column reflectivity are shown in Fig. 4.1 for each of the three events, for the CTRL and the sensitivity (EFSW). The EFSW forecasts of column reflectivity and mean-sea level pressure (Figs. 4.1b,d,f) are quite similar to the CTRL forecasts (Figs. 4.1a,c,e, respectively). Likewise, EFSW forecasts of P_i are also comparable for all events considered. Reducing the variable collection efficiency of cloud water from snow does not seem to have a significant effect on P_i , in comparison to CTRL (Fig. 4.2). Forecasts of liquid-equivalent precipitation between CTRL and EFSW are nearly identical (Fig. 4.3). These marked similarities of reflectivity, P_i , and liquid equivalent precipitation indicate that the scheme is still able to generate precipitation hydrometeors to the same extent despite the less efficient collection of q_c by snow. These trends in the precipitation fields suggest that the scheme is able to overcome the loss of growth of snow by q_c and is able to sustain the precipitating snow. Conversely, a comparison of the forecasts of SLW for 6 Feb in EFSW (Fig. 4.4b)

reveals an increase in the maxima across the comma-head region, from 0.16 g/kg in CTRL (Fig. 4.4a) to 0.20 g/kg. Likewise, for 26 Jan, CTRL (Fig. 4.4c) shows a maximum of 0.04 g/kg towards the southwestern portion of the comma-head, where EFSW has a maximum q_c value of 0.22 g/kg (Fig. 4.4d). A similar increase is seen for 15 Feb, where CTRL forecasts a maximum of 0.14 g/kg, compared to 0.19 g/kg for EFSW (c.f. Fig. 4.4e and Fig. 4.4f). The forecasts of the sensitivity test for all three events imply that the precipitation fields are maintained, even with a reduced collection efficiency of cloud water by snow. We speculate that the snow is able to overcome the reduced collection efficiency from cloud water in some capacity; however, volume-integrated time series of ice and graupel mixing ratios were very similar to CTRL, and, therefore, definitive conclusions cannot be made here.

4.3 Snow Parameter Sensitivities

4.3.1 Effective Snow Density

Many BMPs utilize a spherical snow shape with constant effective density. However, according to Thompson et al. (2008), observations have shown that the density varies inversely with size, according to the diameter. The spherical and constant-density assumption for all hydrometeors, except snow, is described through the mass-diameter relation. This relation is represented through the power law

$$m(D) = (\pi/6)\rho_h D^3 \quad , \quad (4.4)$$

where ρ_h is the assumed hydrometeor density and D is the particle diameter. In TSON, for snow only, the exponent is set to 2 instead of 3 in accordance with observational studies, both at the surface and aloft (from Cox 1988), and is described by the mass-diameter power law,

$$m(D) = am_s D^2 \quad , \quad (4.5)$$

where am_s (0.069 g/cm^3) is the effective density constant for snow. This proportionality of the mass of snow to D^2 implies a bulk density that is inversely related to the size. The effective density for snow, however, is frequently assumed to be 0.1 g/cm^3 (Morrison and Grabowski 2010). According to Thompson et al. (2008), such an approximation is not entirely realistic for small and large sizes. We suspect that a constant effective snow density, henceforth indicated by ESD, will inhibit the scavenging of cloud water if the snow size distribution is composed of more small than large snowflakes. Holding the density at a constant will tend to overestimate (underestimate) the density for large (small) snowflakes. To assess the dependence of q_c on the effective density of snow, in our experiment, am_s is set to the constant 0.1 g/cm^3 . Units of effective density are expressed in g/cm^3 , which is consistent with the TSON scheme code (Thompson et al. 2008).

In comparing the CTRL and ESD P_i forecasts, a slight increase in P_i is seen across central Indiana and southeastern Missouri for ESD fields on 6 Feb (c.f. Fig. 4.5a to 4.5b). Likewise, a comparison with the 26 Jan forecasts show a minor increase in P_i across west-central Tennessee (c.f. Fig. 4.5c to 4.5d). The trivial enhancement of P_i is also noted for 15 Feb, (c.f. Fig. 4.5e to 4.5f) with a similar enhancement of P_i across the comma-head region for ESD. The trends in these simulations imply that an increase in

effective snow density would increase the precipitation mass. However, as seen in Fig. 4.6, the higher effective snow density allows more SLW to be maintained in the cloud. Comparisons of Fig. 4.6b to Fig. 4.6a show a marked increase, both spatially and maximally, in q_c parallel to the comma-head for the 6 Feb event. Similarly, the constant snow density results in an increase in the magnitude of q_c across the comma-head for 26 Jan, where CTRL has a q_c maximum of 0.04 g/kg, compared to 0.16 g/kg for ESD. This enhancement trend is also evident for 15 Feb, where forecasts maximums of q_c range from 0.14 g/kg for CTRL (Fig. 4.6e) and 0.20 for ESD g/kg (Fig. 4.6f). While our results are consistent amongst the 3 experiments, the cases did not appear to have predominantly large snowflakes. If the environments had larger snow crystals, then we hypothesize that the experiments may yield different tendencies. However, such a conclusion can not be made here.

4.3.2 Snow Sphericity

We now examine the discrepancies between the method of calculation of the snow mass-volume power laws of most BMPs, indicated by (4.4), and the mass-diameter power law employed by CTRL in (4.5). In CTRL, the snow is primarily composed of fractal-like aggregated crystals, which captures the majority of snow reaching the surface (Thompson et al. 2008). Even though the non-spherical function is also utilized by MORR, some schemes employ a spherical shape parameter described by (4.4). Thompson et al. (2008) show that the shape parameter (4.4) and combined gamma distribution for snow tends to produce a larger mass-weighted mean size of the

snow than a spherical shape parameter. In consequence, if there is a change from a variable snow density of CTRL to a constant effective snow density, then the mass power law becomes volume-driven instead of diameter-based. Because the snow growth processes are governed by the particle number and surface area, which the sphericity assumption minimizes, a spherical snow should result in higher concentrations of SLW (due to lessened snow growth). Thus, it is hypothesized that this alteration may produce q_c similar to those seen by NSSL, and MY in Chapter 3. To determine the effects of the shape parameter on both q_c and q_s , (4.5) is replaced by (4.4), with ρ_h described by the constant density for snow ρ_s (100 g/m^3), and the exponent changed from a 2 to a 3. The density units employed here are consistent with the TSON parameterization code (Thompson et al. 2008). This test is denoted by SPSS.

Changing the snow shape from a two-dimensional function to a spherical function decreases P_i for all three events. For 6 Feb (c.f. Fig. 4.7a and 4.7b), there is a decrease in P_i across the westernmost portions of the comma-head, most notably across central Indiana and east central Illinois. A comparison of SPSS to CTRL for 26 Jan shows a similar decrease in P_i across the comma-head (c.f. Fig. 4.7c and 4.7d). This pattern is also noted in Fig. 4.7f, in comparison to Fig. 4.7e, for 15 Feb, where P_i is lessened across southern Indiana. These tendencies are all in line with what is expected from a spherical shape distribution. The smaller surface area of the snow crystals inhibits snow growth, which, in theory, may allow maintenance of q_c within the comma-head portions of the cyclones. However, trends in SLW forecasts between CTRL and SPSS are not consistent. For 6 Feb, Fig. 4.8a shows a maximum of 0.14 g/kg , compared to 0.18 g/kg for the sensitivity (Fig. 4.8b) for the same location.

Forecasts for 26 Jan also show a slight enhancement of q_c for the same location. This scheme experiment produces a maximum of 0.12 g/kg, compared to 0.06 g/kg for CTRL (c.f. Fig 4.8c and Fig 4.8d). However, a decrease in q_c between CTRL and SPSS is evident for 15 Feb (c.f. Fig. 4.8e and Fig. 4.8f). According to experiment results from Thompson et al. (2008) for a warm, shallow cloud, spherical snow produces less SLW and more snow than a non-spherical shape parameter. On the other hand, sedimentation of snow, which is directly related to mass-weighted mean size, also has an effect on “riming due to geometric sweepout and depositional growth due to ventilation” (Thompson et al. 2008). In this scenario, snow growth can be aided by not only vapor deposition, but also riming.

4.3.3 Capacitance of Spheres and Plates/Aggregates:

For TSON, the rate in which snow collects cloud water is directly proportional to the assigned constant capacitance values for corresponding snow shapes. Capacitance measures the ability of snow crystals (or any hydrometeor) to hold an electric charge. The capacitance is commonly defined in a parallel plate arrangement by the quotient of the object charge and voltage. For snow crystals, capacitance is key for accurate estimates of deposition and evaporation and sublimation rates in NWP models (Westbrook et al. 2008). The capacitance can vary depending on whether the predominant ice crystal shapes are columns and plates, dendrites, or aggregate snowflakes. Westbrook et al. (2008) stated that the capacitance for aggregate snowflakes is approximately 0.25, which is shown to be in close agreement with aircraft measurements of snowflake sublimation rates. This capacitance represents a fraction

that takes into account charge and voltage, and, is therefore independent of size. Because the capacitance is expressed as a fraction, it is unitless for our purposes. Additionally, it was demonstrated that the commonly-accepted capacitance of a sphere (0.5) can cause NWP models to over-estimate the evaporation rate of snowflakes by a factor of 2 (Westbrook et al. 2008). We postulate that changing the capacitance to 0.25 (from 0.5) will not overestimate the evaporation of snow, thus allowing more snow to be sustained, which, in turn, could allow for more q_c maintenance in the comma-head cloud system. For spheres, the capacitance in CTRL is set to the constant 0.5. To test the dependence of q_c forecasts on the capacitance of aggregate snowflakes, the capacitance is changed to 0.25. This test is referred to as CAP.

Comparisons of CTRL and CAP forecasts of P_i reveal nearly identical spatial and quantitative correlations for all three events. For 6 Feb, the CTRL forecast of P_i (Fig. 4.9a) is markedly similar to that of CAP (Fig. 4.9b). Trivial discrepancies are also noted for 26 Jan (c.f. Fig. 4.9c to 4.9d). The CAP P_i forecasts (Fig. 4.9f) remain nearly unchanged for a change in capacitance for 15 Feb, in comparison to the CTRL (Fig. 4.9e). Conversely, lowering the capacitance of the aggregate snowflakes appears to have some effect on the q_c along the long axis of the comma-heads. For example, for 6 Feb, there is approximately the same q_c area between 850 and 700 hPa as shown in between the CTRL (Fig. 4.10a) and the sensitivity (Fig. 4.10b). However, a second area of enhanced q_c near the 500-hPa geopotential level seen in Fig. 4.10b for CAP is not evident in CTRL (Fig. 4.10a). However, simulations for 26 Jan do not appear to show a similar increase in q_c with a change of capacitance. Comparisons of Fig. 4.10c to Fig. 4.10d show nearly identical forecasts of q_c along the long axis of the comma-head

precipitation system. However, an increase in q_c between CTRL (Fig. 4.10e) and CAP (Fig. 4.10f) is apparent for 15 Feb. Like the forecasts for the 6 Feb event, a secondary SLW enhancement occurs above the similar regions of q_c (c.f. Fig. 4.10e to 4.10f). While the maxima of q_c are nearly identical across all comma-heads, there are some minor differences between the CTRL and the lessened capacitance simulation.

4.4 Prescribed Cloud Droplet Concentration

In CTRL, the prescribed number of cloud droplets to be activated upon condensation was set to an approximate $100 \times 10^6 \text{ m}^{-3}$. The prescribed concentration is based on observations from clean air or maritime environments (Martin et al. 1994). This droplet concentration has direct dependencies on droplet mean size and autoconversions to rain, and has a strong effect on the median volume droplet diameter of cloud liquid. However, a prescribed cloud droplet concentration of $300 \times 10^6 \text{ m}^{-3}$, has been linked polluted, continental atmospheres (Miles et al. 2000; Thompson et al. 2008; Nygaard et al. 2011). We hypothesize that setting the prescribed cloud droplet density to a value representative of continental environments may enable more SLW to remain in the cloud (Miles et al. 2000). This change of the prescribed cloud droplet density has been shown to be in line with observations and have an effect on the overall predictability of cloud liquid water (Thompson et al. 2008; Nygaard et al. 2011). This test of changing the cloud droplet density to $300 \times 10^6 \text{ m}^{-3}$ is denoted by COCD. Perhaps a 3-fold increase in the number concentration of cloud droplets will result in more “leftover” cloud droplets after scavenging of the SLW from cloud ice, snow, etc.

It is plausible, however, to think that such an increase in the droplet concentration will only result in more snow scavenging, which may act to increase P_i and liquid equivalent precipitation accumulation, but not necessarily q_c . However, it should be noted that the cloud droplet concentration could vary significantly from event to event (Thompson et al. 2008; Nygaard et al. 2011).

Sensitivity simulations of P_i for the 6 Feb event are presented in Fig. 4.11. In comparison to CTRL (Fig. 4.11a), P_i for the COCD experiment is very similar. A comparable evaluation is evident for 26 Jan (c.f. Fig. 4.11c to 4.11d). Likewise, an analogous conclusion can be made for the 15 Feb event (c.f. Fig. 4.11e to 4.11f). Setting the prescribed cloud droplet density to a value that is commonly associated with continental environments did not have a significant effect on P_i . Because the increase in droplet concentration did not have an effect on the precipitation hydrometeors, it can be speculated that snow growth from cloud water was very similar to CTRL. Thus, we anticipate that an excess of cloud droplets is sustained in the cloud. For example, Fig. 4.12a shows a maximum q_c of 0.16 g/kg, compared to 0.20 g/kg in COCD (Fig. 4.12b) for the 6 Feb event. A similar increase is evident for 26 Jan, where the max q_c value increases from 0.04 g/kg in the CTRL, as seen in Fig. 4.12c, to 0.12 g/kg for COCD (Fig. 4.12d) for the same location. For 15 Feb, the increase in SLW is not quite as apparent as for 6 Feb and 26 Jan. Nevertheless, a small enhancement occurs in COCD, in comparison to CTRL (c.f. Fig. 4.12e to Fig. 4.12f). We speculate that the overall increase in the prescribed cloud droplet concentration does not have a significant effect on the hydrometeor production, allotment, or precipitation. However, there is a slight

enhancement in q_c parallel along the long axis of the comma-head portion of the cyclone.

In Fig. 4.13, there are time series of q_c , q_s , and q_t for the 6 Feb event for each of the sensitivity experiments across the comma-head precipitation system. In Fig. 4.13a, EFSW shows a marked increase in SLW across the comma-head region while changing the snow shape to a spherical function has very little impact. However, the spherical snow shape does have a detrimental effect on q_s , especially in comparison to the other simulations (see Fig. 4.13b). With the exception of the spherical snow sensitivity, the total hydrometeor mixing ratios are very comparable to the CTRL. For 26 Jan, seen in Fig. 4.14a, there are significant discrepancies between the CTRL and sensitivity experiments in the cloud water mixing ratio. However, the differences in q_s and q_t are less substantial. Once again, the spherical snow shape has much less q_s and q_t . In Fig. 4.15, the change in snow density has the greatest impact on cloud water, snow, and total hydrometeor mixing ratios in the Feb 15 case. However, the discrepancies for SLW are much more apparent between the sensitivities and the CTRL than for either q_s or q_t . These trends are also seen in Table 4.1. Many sensitivity runs had a major impact on q_c , but only a minor impact on snow or total hydrometeor mixing ratios.

Date	MP	Cloud Water (%)	Snow (%)	Total Hydrometeor (%)
6-Feb	EFSW	63.11%	-1.46%	5.97%
	ESD	40.63%	4.49%	8.66%
	SPSS	-13.18%	-26.35%	-25.11%
	COCD	36.62%	0.37%	4.42%
	CAP	0.06%	-0.42%	0.22%
26-Jan	EFSW	29.75%	1.53%	10.32%
	ESD	16.57%	5.58%	7.92%
	SPSS	-1.05%	-23.74%	-14.26%
	COCD	39.45%	2.61%	12.17%
	CAP	-1.05%	-0.45%	-0.28%
15-Feb	EFSW	50.01%	0.04%	0.02%
	ESD	80.44%	5.93%	8.48%
	SPSS	-52.60%	-26.69%	-26.75%
	COCD	0.23%	0.27%	1.01%
	CAP	0.06%	-0.30%	0.18%
Average Change		19.27%	-3.91%	-0.47%

Table 4.1: Changes in summations of mixing ratios across comma-head precipitation systems for each of the 3 events considered, compared to CTRL.

The results of the sensitivity experiments presented in this study show that subtle changes to either the collection or collision efficiencies between snow and cloud water can result in a nontrivial increase in q_c , not only along the cross-section, but also across the entire volume of the comma-head region. However, the subtle change in collection efficiency had a nearly negligible effect on the snow budget, and a minor effect on the total hydrometeor budget. Similar tendencies were apparent when the snow density was set to a constant and the cloud droplet concentration increased to a value consistent with observations (Martin et al. 1994; Nygaard et al. 2011). However, changing the snow shape to a spherical function had a converse effect on the cloud water budget. Correspondingly, the total hydrometeor budget was also negatively affected through the volume of the comma-head region for each event. The experiment

that tested the capacitance of aggregates had little effect on the other cloud water, snow, and hydrometeor balance within the parameterization. The results of these sensitivities indicate that some of the changes may be useful for counteracting the TSON bias of under-forecasting SLW as previously described by Thompson et al. (2008) and Nygaard et al. (2011), but more case studies would be necessary to draw firm conclusions on whether changes to the scheme would be reasonable for operational employment.

Chapter 5

Conclusions

This study provided a comprehensive comparison of the relationships between the choice of microphysical parameterization and forecasts of SLW. Four microphysical parameterizations were compared for three comma-head snow events to assess how the change in scheme affects NWP forecasts of aircraft icing. The experiments were run using the Advanced Research Weather and Forecasting Model (WRF-ARW), and included two partially-double moment schemes and two fully-moment schemes. The Thompson (TSON) scheme was partially-double moment only for rain and ice while MORR was single-moment with respect to only cloud water. Meanwhile, NSSL and Milbrandt-Yau (MY) were fully-double moment schemes. The forecast parameters considered for each parameterization included maximum column reflectivity, column-integrated precipitation hydrometeors (P_i), total liquid-equivalent precipitation accumulation, and individual hydrometeor mixing ratios. The areas of particular interests pertained to only the comma-head regions within each cyclone.

The NSSL experiment had lower reflectivities for all three events, most likely owing to the use of a volume-based assumed snow size distribution (opposed to diameter-based). Despite the deviations in reflectivity, the forecasts of liquid equivalent precipitation were remarkably similar from scheme-to-scheme. Additional investigations of synoptic-scale setups and thermodynamic and kinematic fields revealed only trivial discrepancies between the parameterizations. However, a significant forecast spread, both storm-to-storm and scheme-to-scheme, was evident for

cloud water mixing ratio (q_c). The TSON parameterization consistently produced lower quantities of SLW, both spatially and quantitatively. This trend was noted in all three events, but was most apparent in the colder environments. We theorize that this q_c deficiency was a result of scavenging by snow, which is common in cold, shallow systems (Thompson et al. 2008; Nygaard et al. 2011). The parameterization forecasts were then evaluated with PIREPs in 6-h intervals for each case. Multiple skill scores and scoring parameters were compared on a scheme-by-scheme basis. Only in the 26 Jan event did TSON have the highest average skill scores or highest accuracy. For the 6 Feb and 15 Feb events, the accuracy, probability of detection (POD), and false alarm ratio (FAR) were inferior in TSON, compared to those of the other schemes. Not only was the overall underprediction of SLW by the models consistent with the results found by Reisner et al. (1998), Guan et al. (2001), and Vaillancourt et al. (2002), the underprediction of SLW in TSON was in line with the findings of Nygaard et al. (2011), who investigated terrain-influenced events and found that for a 3-km spacing, TSON underpredicted SLWC, with respect to MORR and observations. Conversely, unlike Reisner et al. (1998), our results did not show that an increase in the number of moments for cloud water resulted in higher values of q_c . In fact, the fully-double moment schemes generally produced less SLW compared to the partially-double moment MORR, which agreed with results from Milbrandt et al (2010) that an increase in the number of moments can have an inverse effect on the cloud water. Therefore, it cannot be explicitly concluded that an increase in the number of moments better represented key microphysical processes relating to cloud water, contradicting the findings by Molthan and Colle (2012). The pattern of under-forecasting of SLW by the

partially-double moment TSON subsequently led to an investigation on the processes and parameters responsible for q_c production and maintenance within the TSON scheme.

To quantify the SLW discrepancies seen between TSON and the fully-double moment schemes, and to assess whether TSON is a superior or equally-sufficient scheme for icing forecasts, modifications to the TSON scheme were performed and run for each of the events. Due to the suspected depletion of q_c by snow, and the established sensitivity between snow and cloud water with the TSON scheme (Thompson et al. 2008; Nygaard et al. 2011), these sensitivities were designed to test a variety of snow parameters that had an impact on the q_c for each event. Each case was run with a lessened variable collection efficiency of snow from cloud water. This adjustment resulted in a substantial increase in q_c across the comma-head region for all three events, while maintaining a comparable snow and total hydrometeor mixing ratio. The test of a reduced collection efficiency confirmed the sensitivity between the snow and cloud water fields, as well as the tendency for the snow to over-scavenge the cloud water, which has long been established in the TSON scheme (Thompson et al. 2004; Thompson et al. 2008; Nygaard et al. 2011). A separate experiment was executed involving testing the snow density, in which the diameter-dependent effective snow density was made a constant, which, in theory, would tend to overestimate (underestimate) the density for large (small) snowflakes. This experiment had a nontrivial impact on the maintenance of q_c in the comma-head regions of the cyclone. However, changing the snow shape from a non-spherical function to spherical function had a contrasting effect. The P_i was notably lessened, which was expected, due to the

decrease in surface area of the snow, which reduces the snow growth processes. Thus, theoretically, a spherical snow should result in higher concentrations of SLW, but there was very little change in the SLW in the comma-head region. These results were in line with the experiments by Thompson et al. (2008). Conversely, lowering the capacitance of snow spheres, and consequently better representation of the evaporation of snowflakes, resulted in a slight enhancement of q_c . This alteration did not have significant effects on P_i or snow mixing ratios for any event. Lastly, an alteration was made to the control run of TSON that tested the effect of a prescribed cloud droplet concentration on the forecast of q_c . Because of the dependencies between cloud droplet number and mean size of droplets, the concentration was modified from that characteristic of a clean and/or maritime environment, to one typical of a “dirty”/continental environment (Miles et al. 2000). The increase in number concentration resulted in more SLW maintenance for each event, which is consistent with the findings of Thompson et al. (2008) and Nygaard et al. (2011).

While the prevailing forecasts for each parameterization are similar in many ways, there are some differences that cannot be overlooked. Because the FAA employs use of the Rapid Refresh model, which utilizes the partially-double moment Thompson scheme, it was logical to test the scheme in terms of the SLW forecasts. It is speculated that a forecast as precise as location and timing of SLW by a double-moment scheme may be preferential for aircraft icing. However, evaluation of q_c forecasts with PIREPs revealed a greater storm-dependency than scheme-dependency. While the double-moment schemes did have better general skill scores, the variability was too pronounced to draw firm conclusions on the specific choice of parameterization.

Nevertheless, the tendency for the TSON scheme to scavenge out too much q_c at the expense of snow in cold cloud systems that was found by Thompson et al. (2008) and Nygaard et al. (2011), was also apparent in our experiments. A lessening of the variable collection efficiency in TSON may counteract depletion of SLW by snow, without having detrimental effects on q_s or the total precipitation. Perhaps employment of such a function would reduce the degree of under-forecasting SLW and allow for better aircraft icing forecasts. Such a speculation, however, may only be valid for specific types of cold-season cyclones, and should not be universally applied without further research. Additional investigations of comma-head snow events, and other events, would provide a more sound foundation for altering the collection efficiency in TSON. Similarly, an increase in the prescribed cloud droplet concentration may improve SLW forecasts without significantly altering the other hydrometeor fields. Such an application could be applied for continental environments, but further research is necessary before considering a complete operational substitution. Even though a more complete event dataset would be necessary in order to draw firm conclusions on whether one particular microphysical parameterization is preferential for operational employment, it is clear that the choice of scheme does have an affect on aircraft icing forecasts.

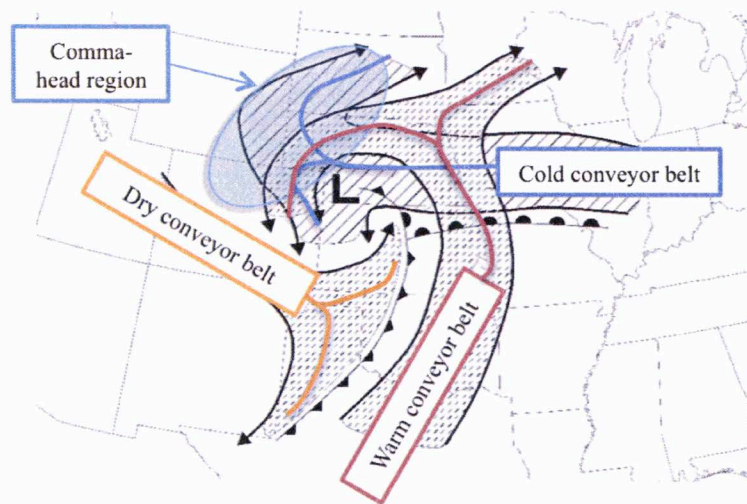


Figure 1.1 Conveyor belts associated with mid-latitude extratropical cyclogenesis. [Taken from Moore et al. (2004)]. The three conveyor belts identified here (warm, cold, dry) have long been established during cyclogenesis, using relative-wind analysis (Harold 1973; Carlson 1980; Danielsen 1964). A conveyor belt refers specifically to an ensemble of parcels with similar thermodynamic characteristics and narrow ranges of potential temperature and wet-bulb temperatures (Browning 1990; Carlson 1991).

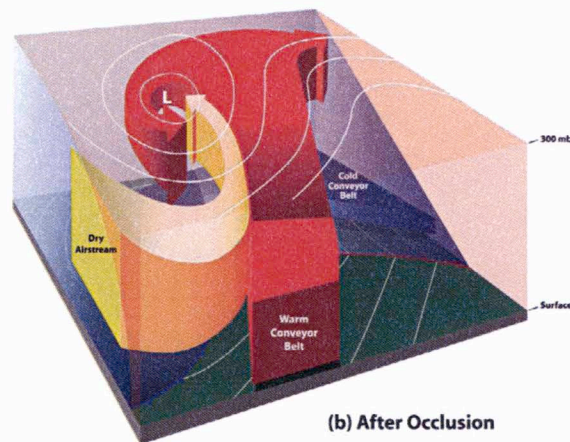
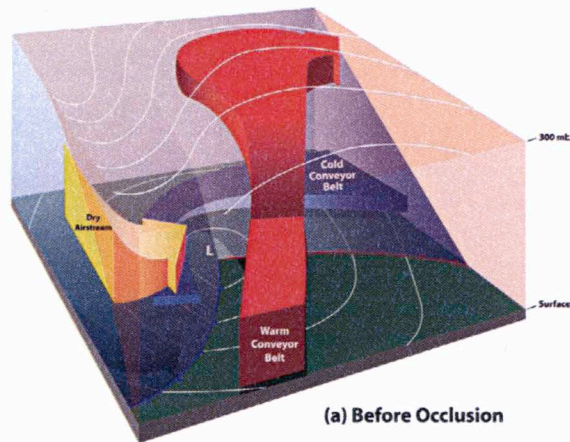


Figure 2.1: Cyclone model showing the warm conveyor belt (red), cold conveyor belt (blue), and dry airstream (yellow): (a) before and (b) after occlusion. [Taken from Schultz and Vaughan (2011)]. Conveyor belt schematic stems from the findings by Danielsen (1964), Harold (1973), and Carlson (1980), who first identified conveyor belts as ensembles of parcels with similar thermodynamic characteristics.

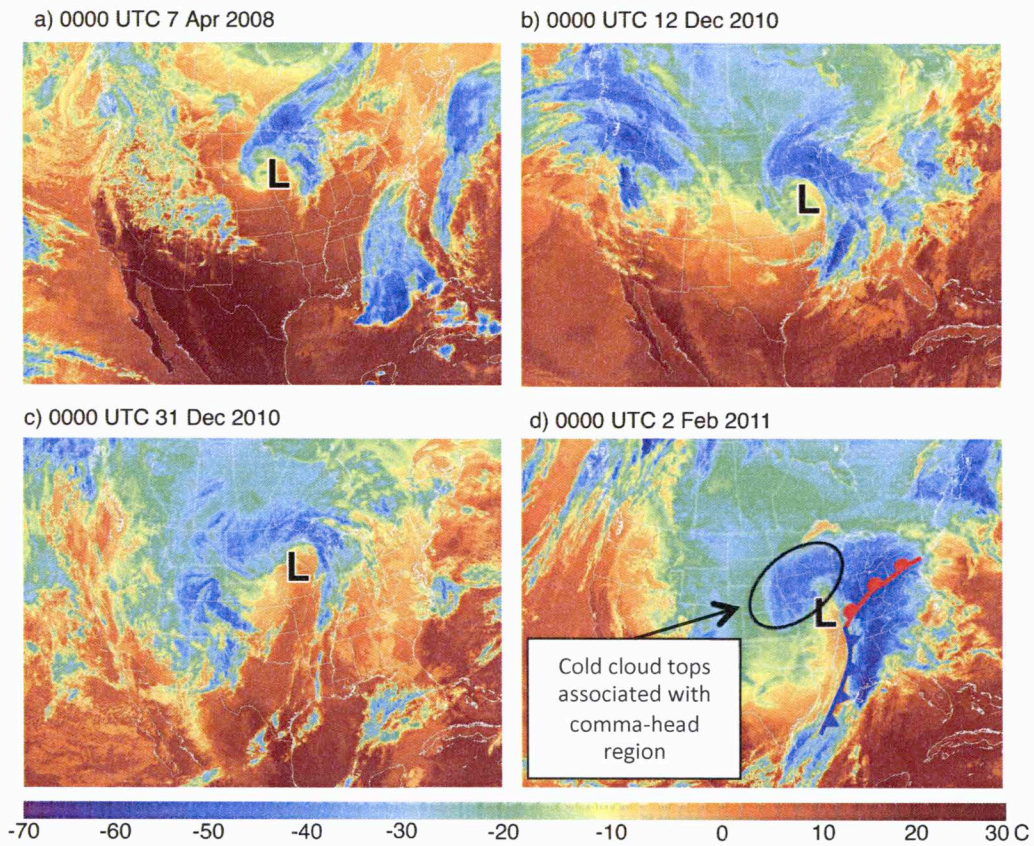


Figure 2.2: GOES infrared satellite image (degrees C; shaded) and approximate surface-low position for (a) 0000 UTC 7 Apr 2008, (b) 0000 UTC 12 Dec 2010, (c) 0000 UTC 31 Dec 2010, and (d) 0000 UTC 2 Feb 2011. In (d), colder cloud tops, identified in green and blue, are collocated along or ahead the surface fronts and to the north-northwest of the approximate surface-low positions.

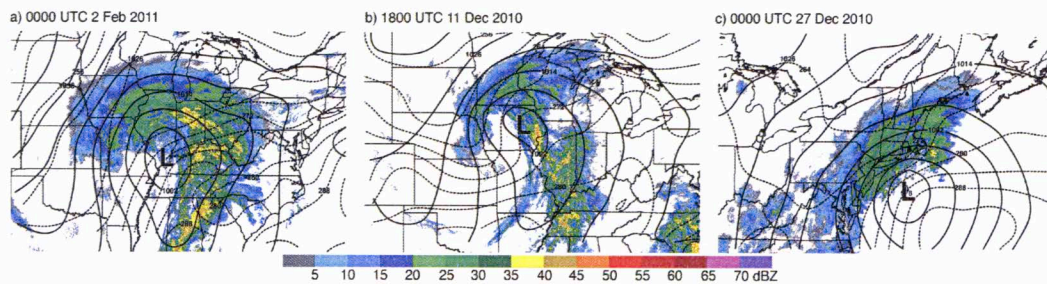


Figure 2.3: Mosaics of Weather Surveillance Radar-1988 Doppler (WSR-88D) composite reflectivity and RUC- (a,c) and NAM-analyzed (b) mean sea-level pressure (mb; solid) and 2-m temperatures (K; dashed) for (a) 2 Feb 2011, (b) 11 Dec 2010, and (c) 27 Dec 2010. The mosaics are derived from the National Mosaic and Multisensor Quantitative Precipitation (NMQ-2013; Vasiloff et al. 2007) Estimation project. Approximate surface-low positions indicated by L and the reflectivity scale is beneath the panels.

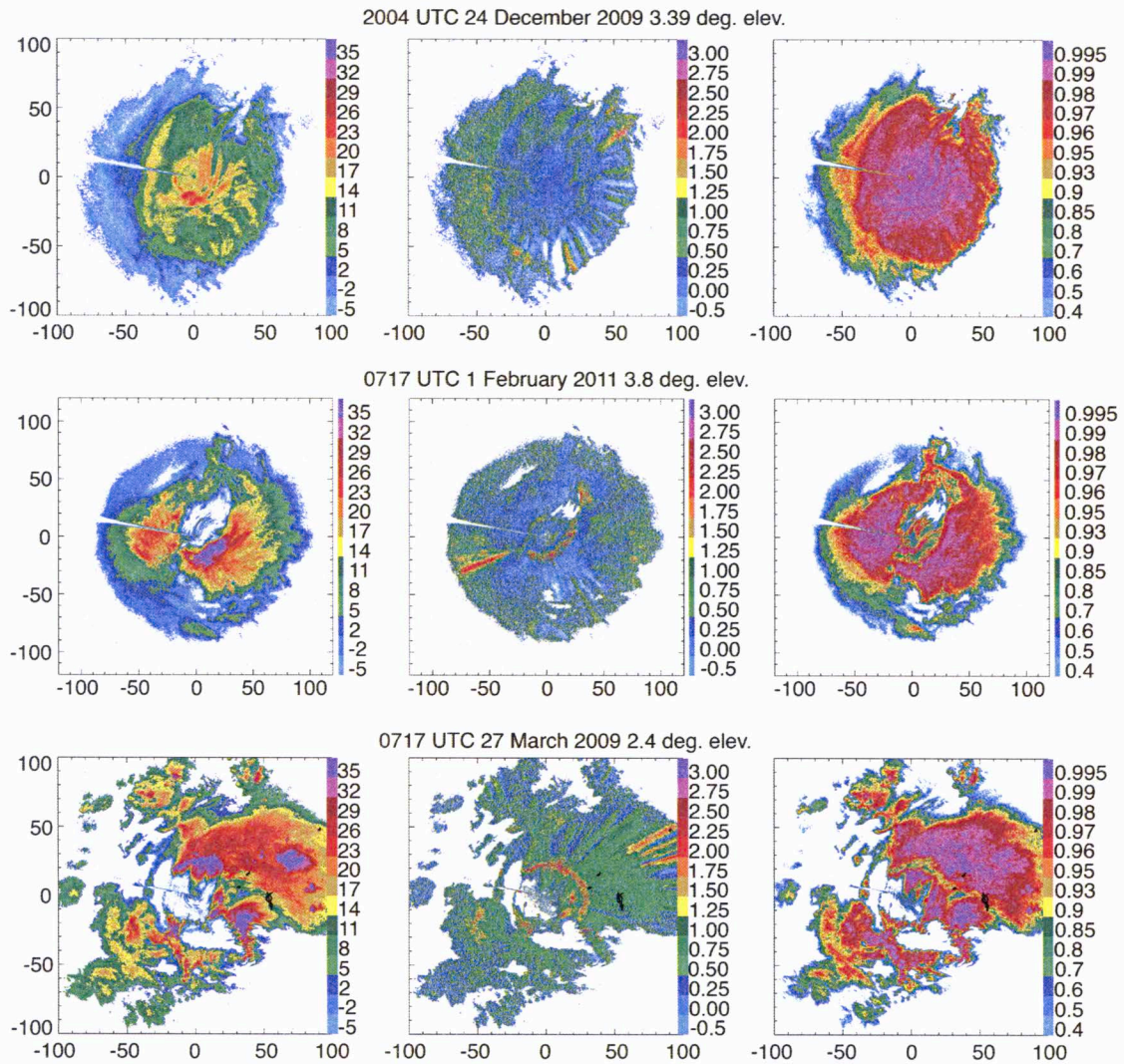


Figure 2.4: OU Prime observations showing 3 examples of radar reflectivity (dBZ; left), differential reflectivity (dB; center), and cross-correlation coefficient (right). [Taken from Dr. Heather Reeves, NSSL]. The dual-polarized radar data could be useful for nowcasting of potential icing environments.

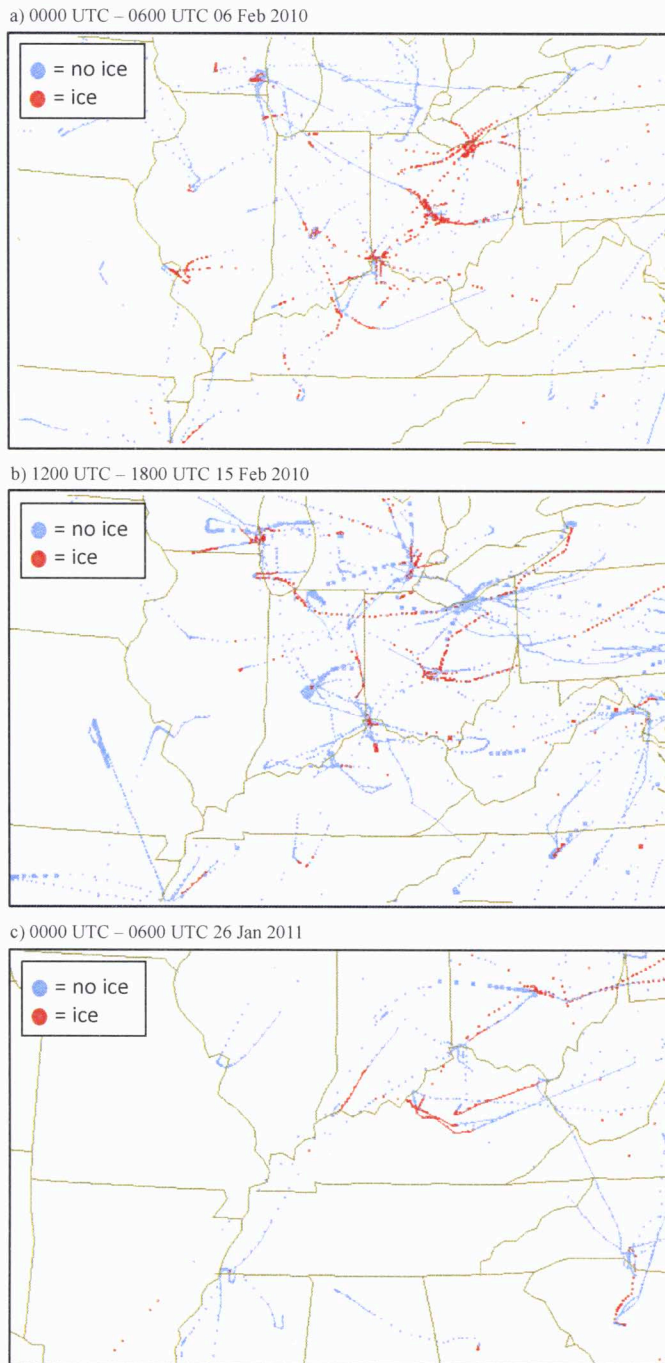
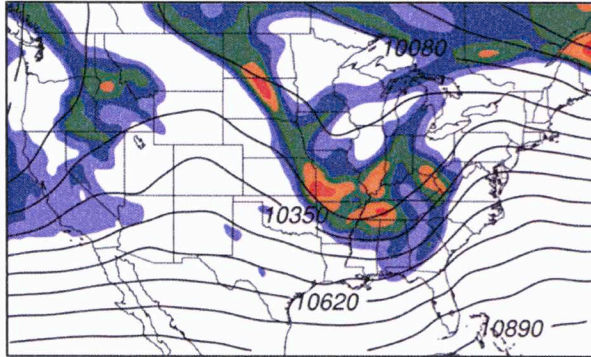
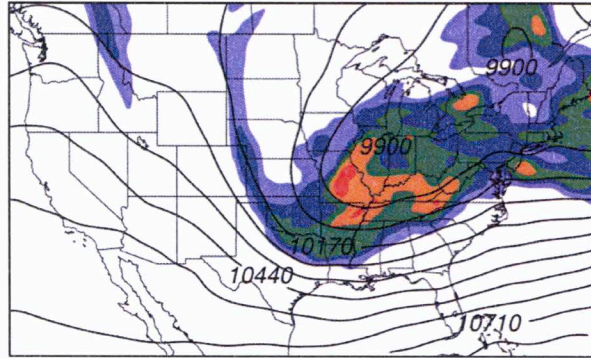


Figure 2.5: AMDAR PIREPs reports for the 6-h time periods indicated.

a) 0300 UTC 6 Feb 2010



b) 1500 UTC 15 Feb 2010



c) 0300 UTC 26 Jan 2011

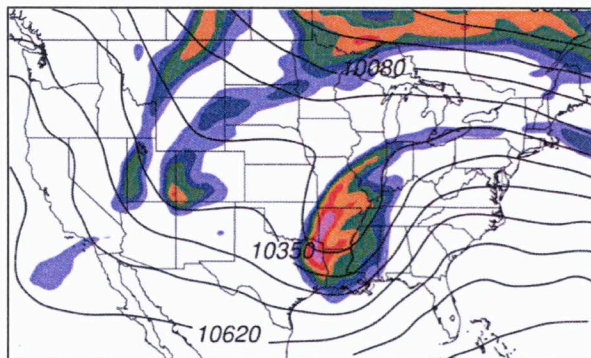
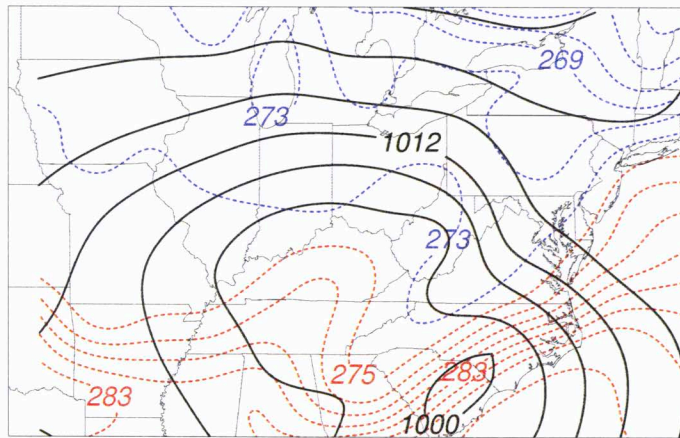
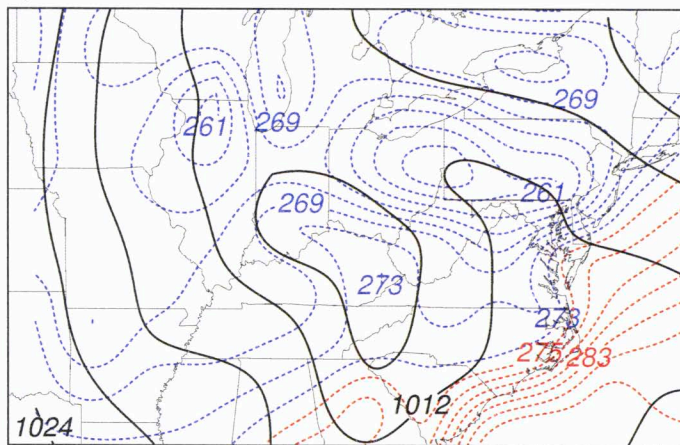


Figure 2.6: 250-hPa geopotential heights (dam; solid) and potential vorticity (potential vorticity units (PVU); shaded) in the 200 – 300 hPa layer for the times indicated above each panel. Enhanced areas of potential vorticity (greater than 4 PVU) are noted coincident along axes of the distinct shortwave troughs for each event.

a) 0000 UTC 6 Feb 2010



b) 1200 UTC 15 Feb 2010



c) 0000 UTC 26 Jan 2011

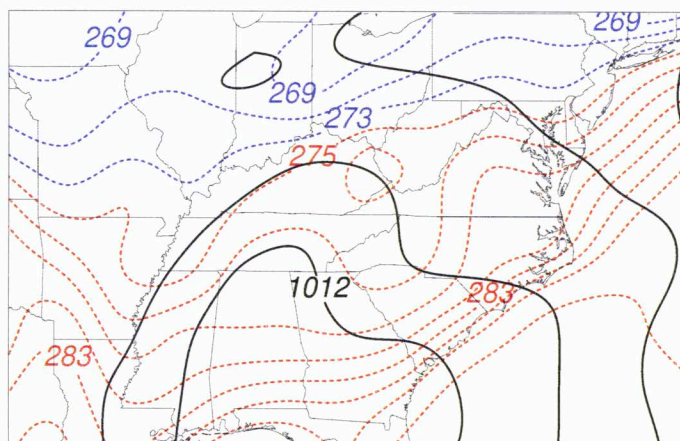
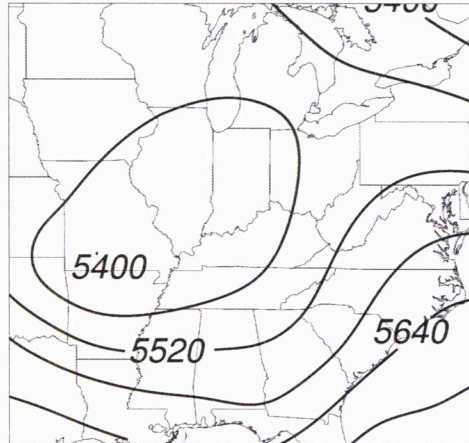
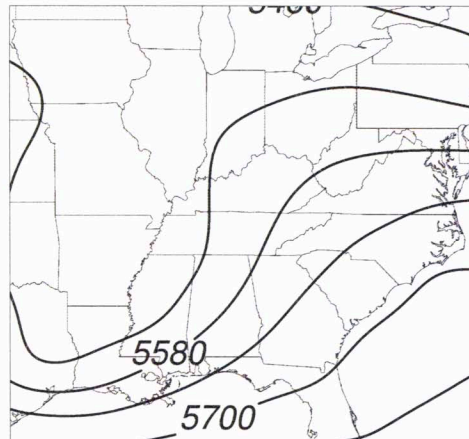


Figure 2.7: NAM-analyzed mean sea-level pressure (mb; solid) and 2-m temperatures (K; dashed) for each event. The pressure contours are in 4-mb intervals, while the temperature contours are in 2-K intervals.

a) 0000 UTC 6 Feb 2010



b) 0000 UTC 26 Jan 2011



c) 1200 UTC 15 Feb 2010

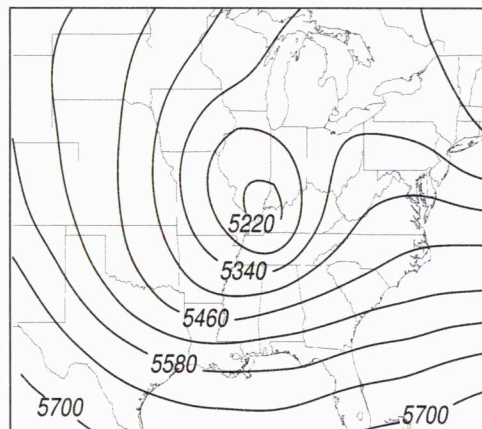


Figure 2.8: NAM-analyzed 500-hPa geopotential heights (m; solid) for each event.

Pronounced shortwave troughs are evident for each of the cases.

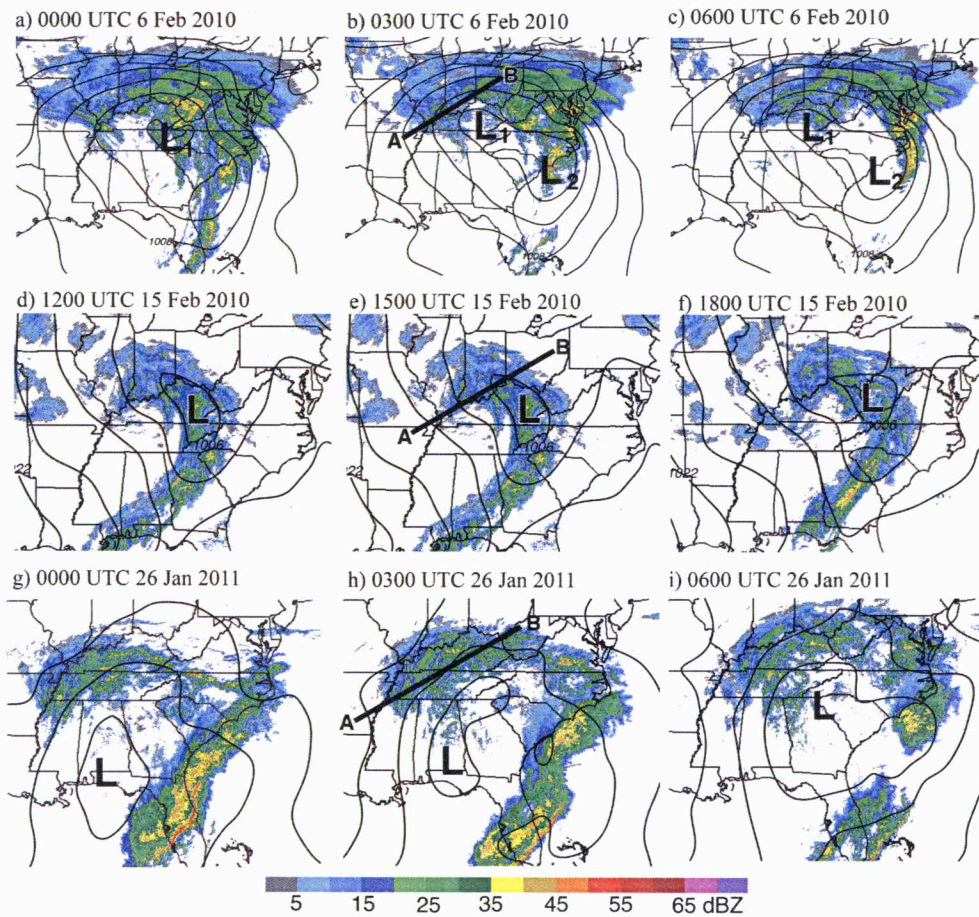


Figure 2.9: Mosaics of Weather Surveillance Radar-1988 Doppler (WSR-88D) composite reflectivity and RUC-analyzed mean sea-level pressure for (a)-(c) 6 Feb 2010, (d)-(f) 15 Feb 2010, and (g)-(i) 26 Jan 2010. The mosaics are derived from the NMQ (Vasiloff et al. 2007) Estimation project. Approximate surface-low positions indicated by L and the reflectivity scale is beneath the panels.

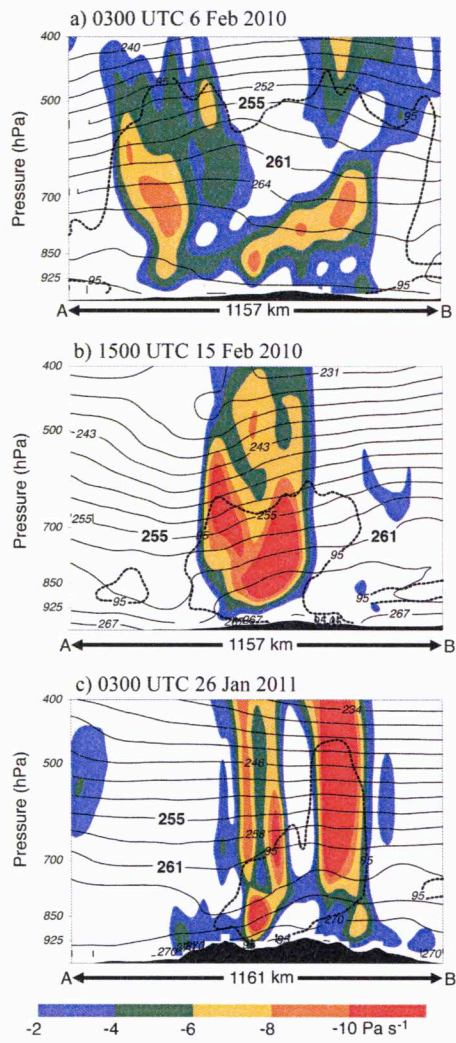


Figure 2.10: Vertical cross-sections (indicated in Fig. 3.3 (b), (e), and (h)) of temperature (K; solid), including dendrite growth zone temperature (K; heavy label), RH > 95% (%; dashed), and vertical velocities (Pa/s; shaded).

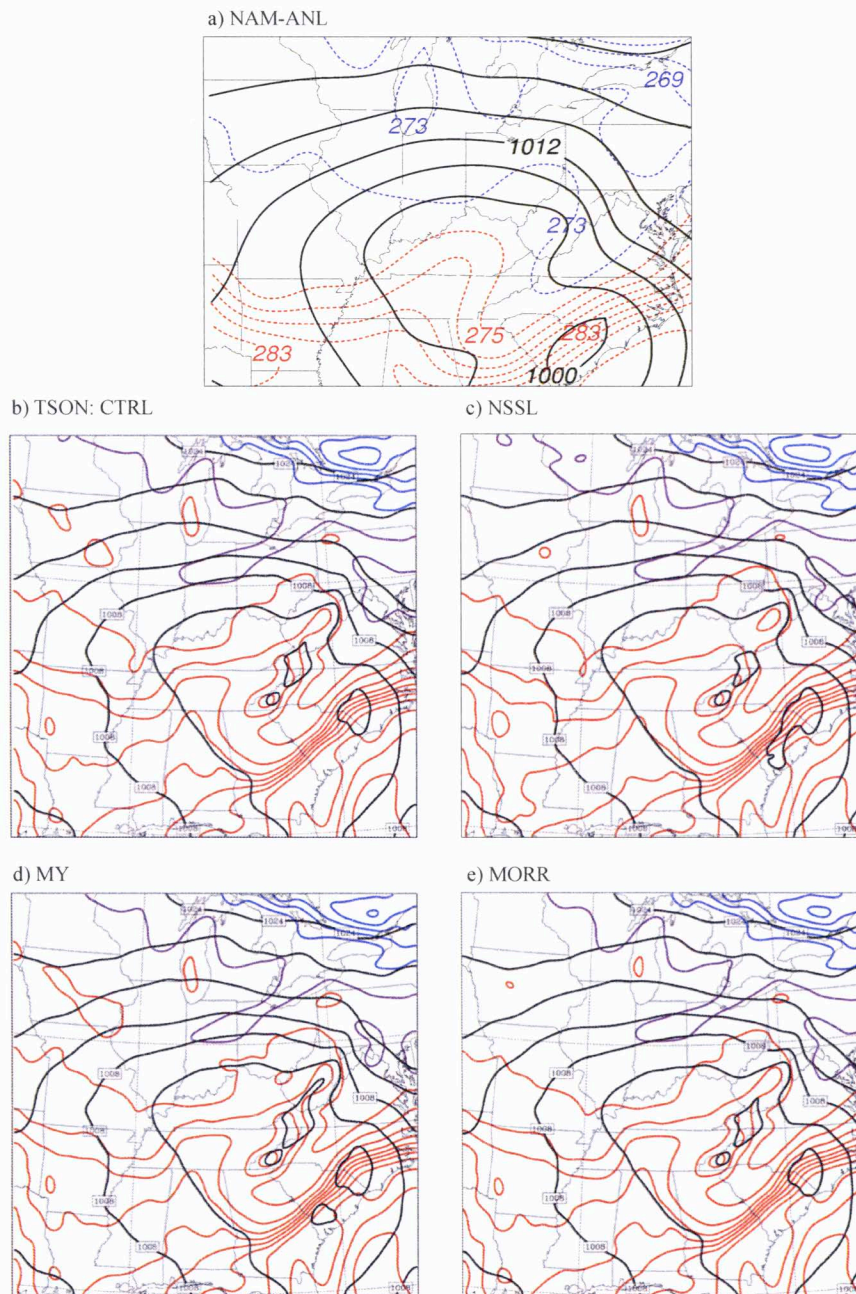


Figure 3.1: Mean sea-level pressure (mb; solid) and 2-m temperatures (K) for (a) NAM-analyzed, (b) Thompson, (c), NSSL, (d) Milbrandt-Yau, and (e) Morrison for 0000 UTC 6 Feb 2010. Mean sea-level pressure is plotted in 4-mb intervals. Temperatures are plotted in 2-K intervals, below (blue), at (purple), and above (red) 273 K

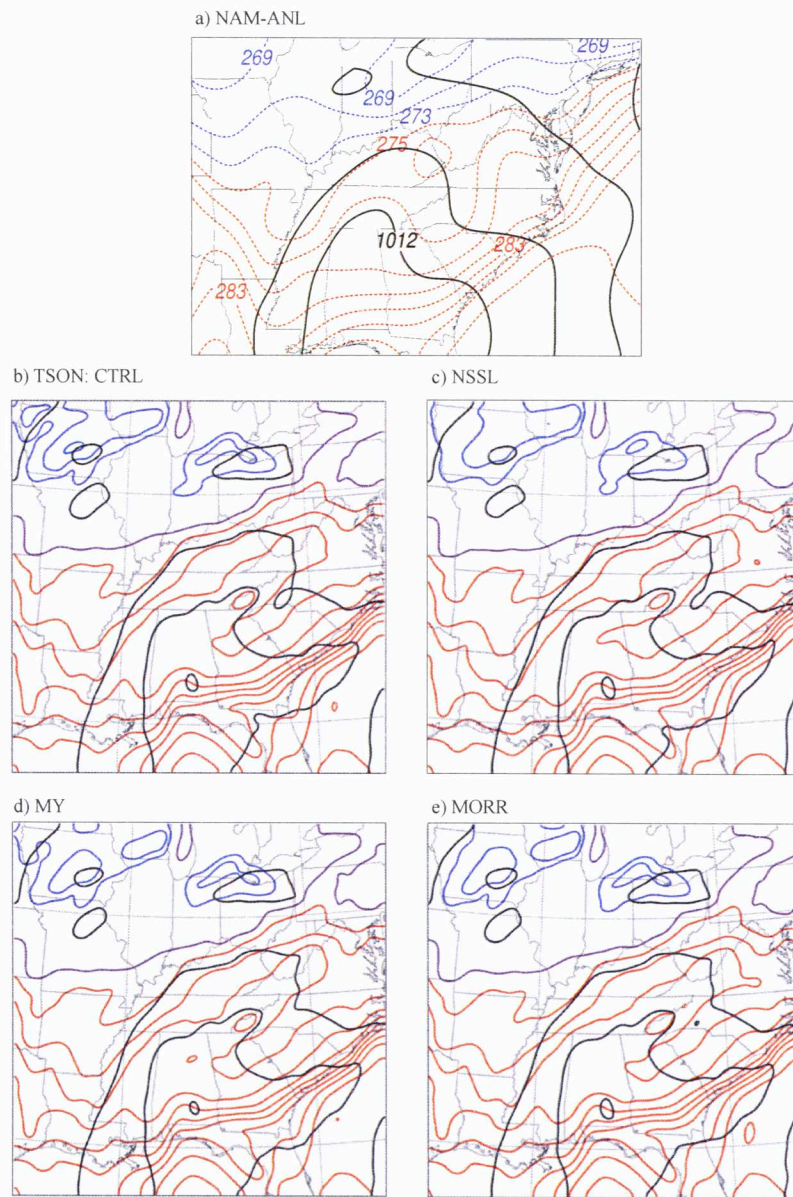


Figure 3.2: Mean sea-level pressure (mb; solid) and 2-m temperatures (K) for (a) NAM-analyzed, (b) Thompson, (c), NSSL, (d) Milbrandt-Yau, and (e) Morrison for 0000 UTC 26 Jan 2011. Mean sea-level pressure is plotted in 4-mb intervals. Temperatures are plotted in 2-K intervals, below (blue), at (purple), and above (red) 273 K.

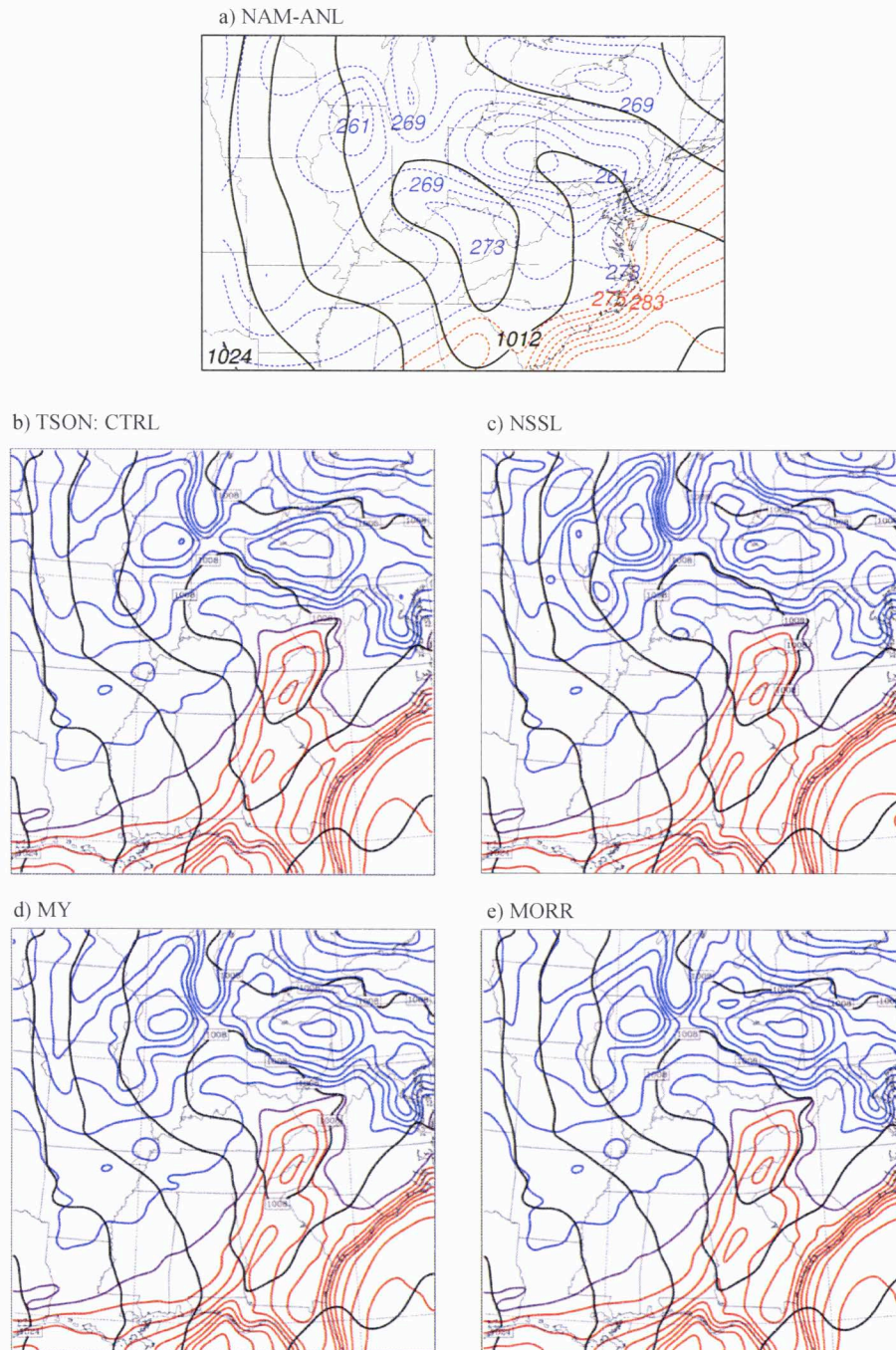


Figure 3.3: Mean sea-level pressure (mb; solid) and 2-m temperatures (K) for (a) NAM-analyzed, (b) Thompson, (c), NSSL, (d) Milbrandt-Yau, and (e) Morrison for 1200 UTC 15 Feb 2010. Mean sea-level pressure is plotted in 4-mb intervals. Temperatures are plotted in 2-K intervals, below (blue), at (purple), and above (red) 273 K.

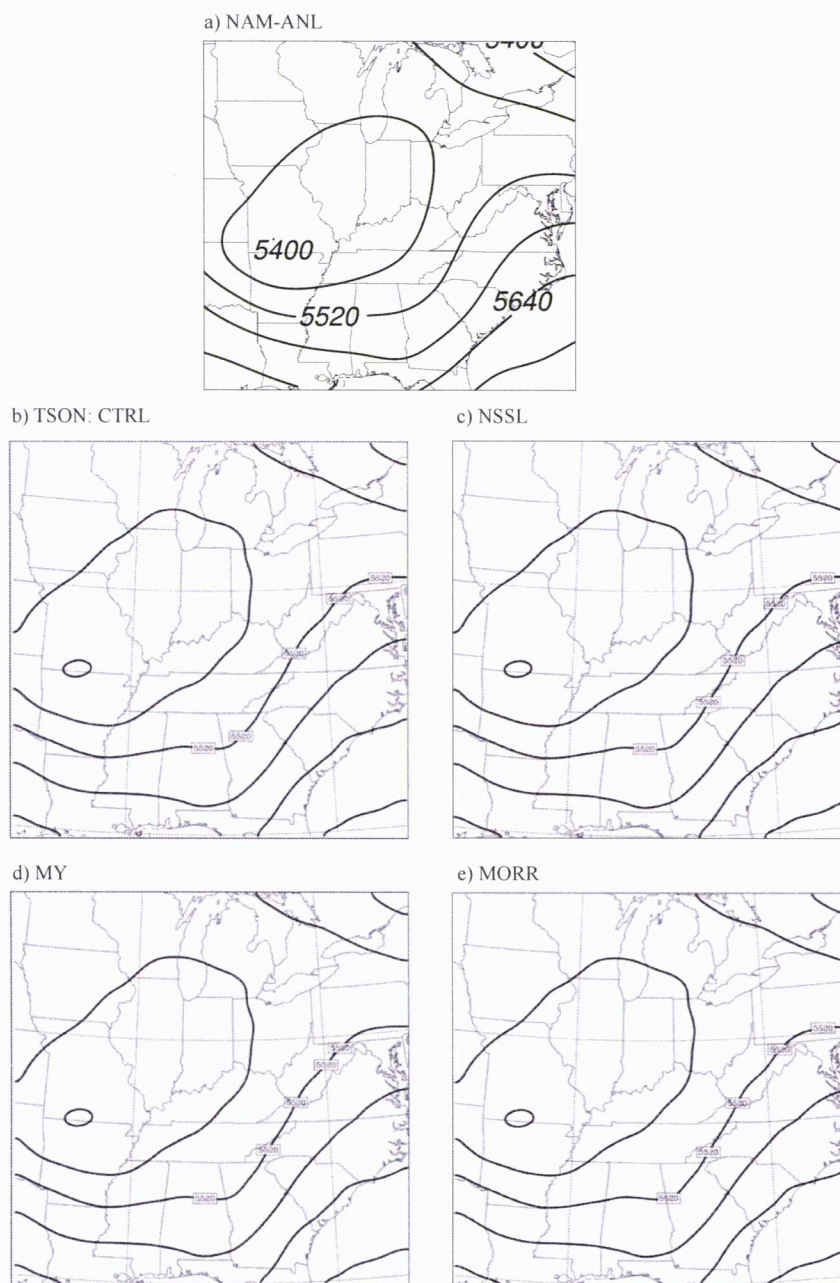


Figure 3.4: 500-hPa geopotential heights (m; solid) for (a) NAM-analyzed, (b) Thompson, (c), NSSL, (d) Milbrandt-Yau, and (e) Morrison for 0000 UTC 6 Feb 2010. Geopotential height field is plotted in 60-m intervals.

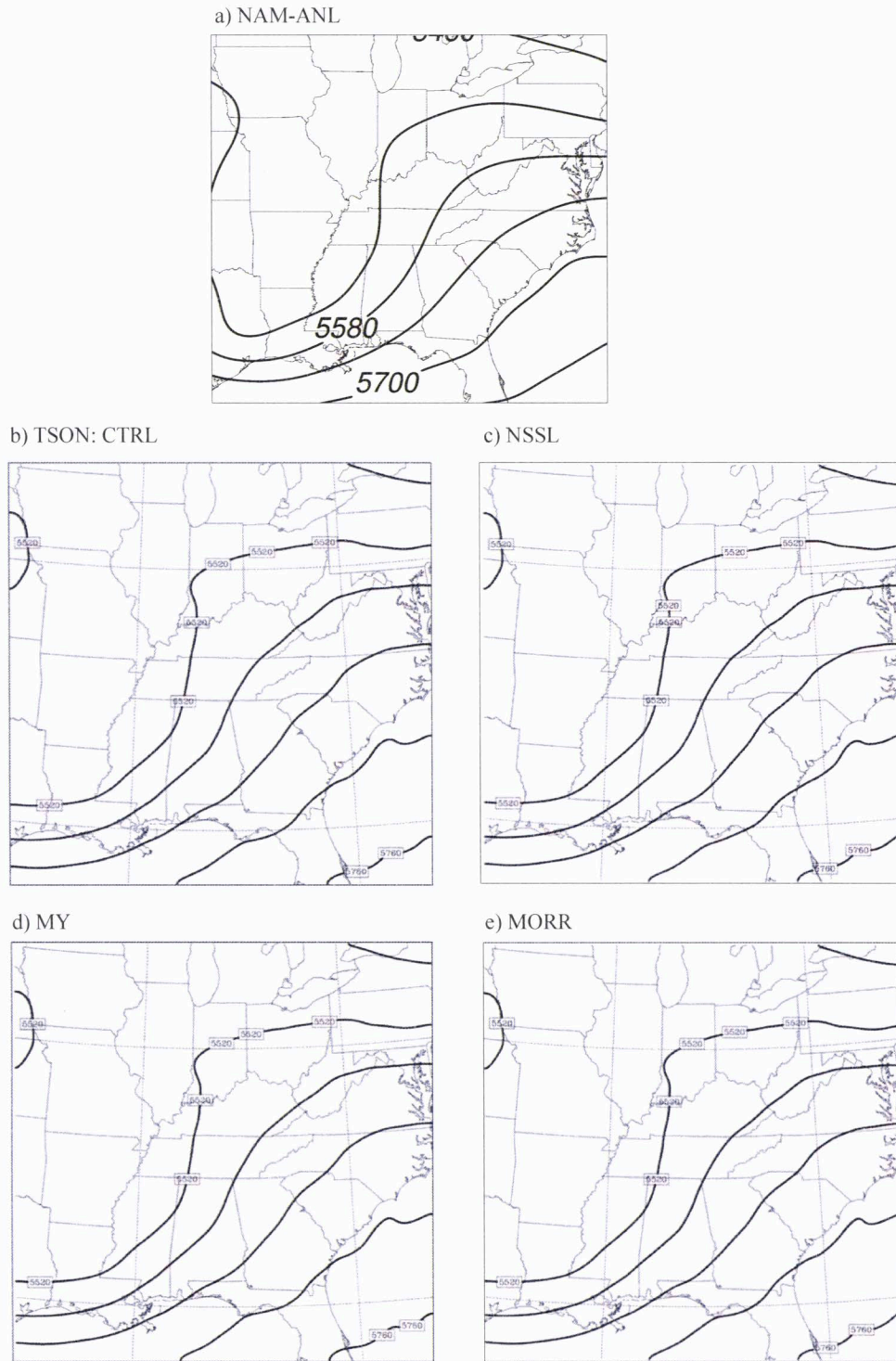


Figure 3.5: 500-hPa geopotential heights (m; solid) for (a) NAM-analyzed, (b) Thompson, (c), NSSL, (d) Milbrandt-Yau, and (e) Morrison for 0000 UTC 26 Jan 2011. Geopotential height field is plotted in 60-m intervals.

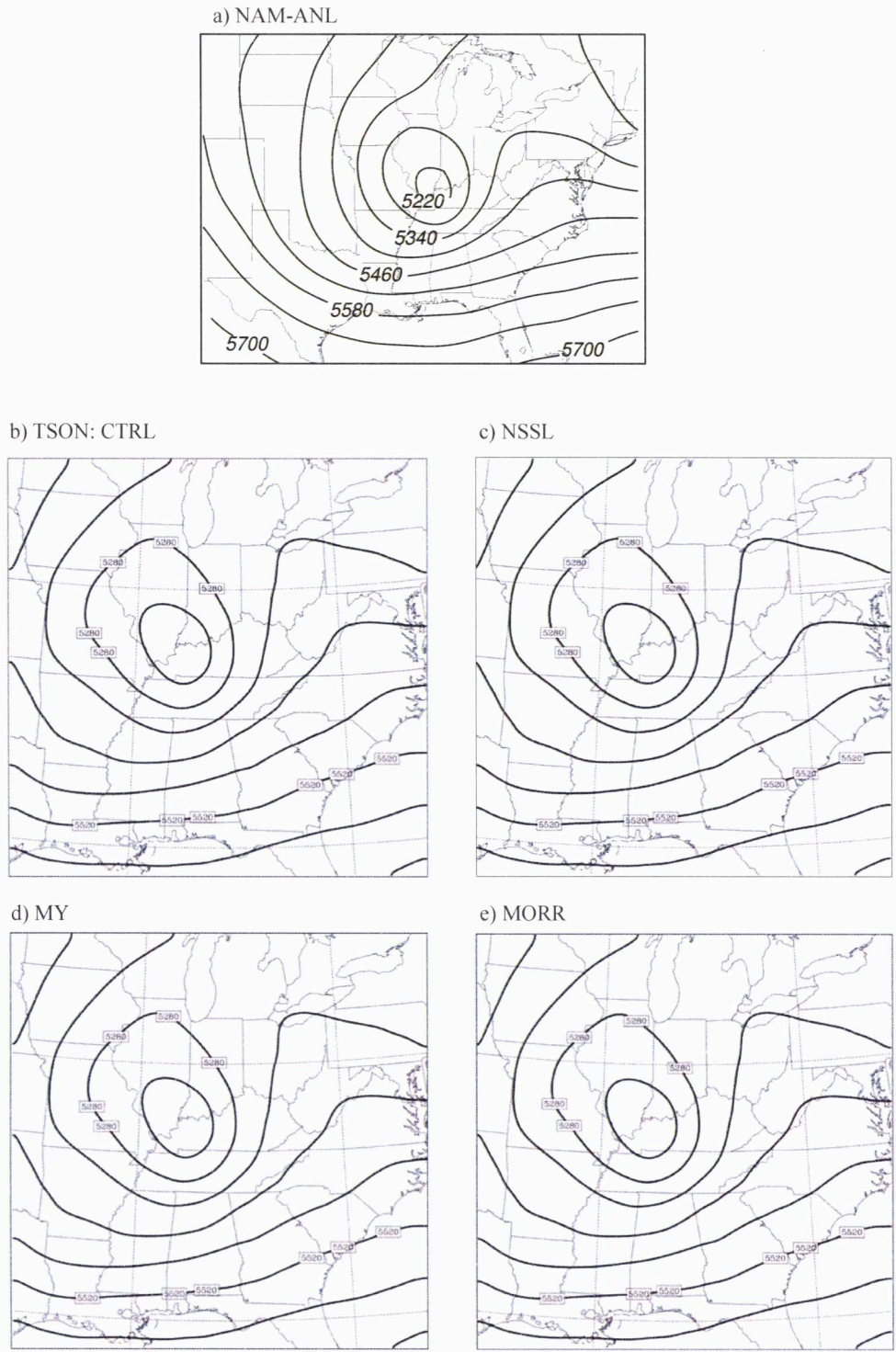


Figure 3.6: 500-hPa geopotential heights (m; solid) for (a) NAM-analyzed, (b) Thompson, (c), NSSL, (d) Milbrandt-Yau, and (e) Morrison for 1200 UTC 15 Feb 2010. Geopotential height field is plotted in 60-m intervals.

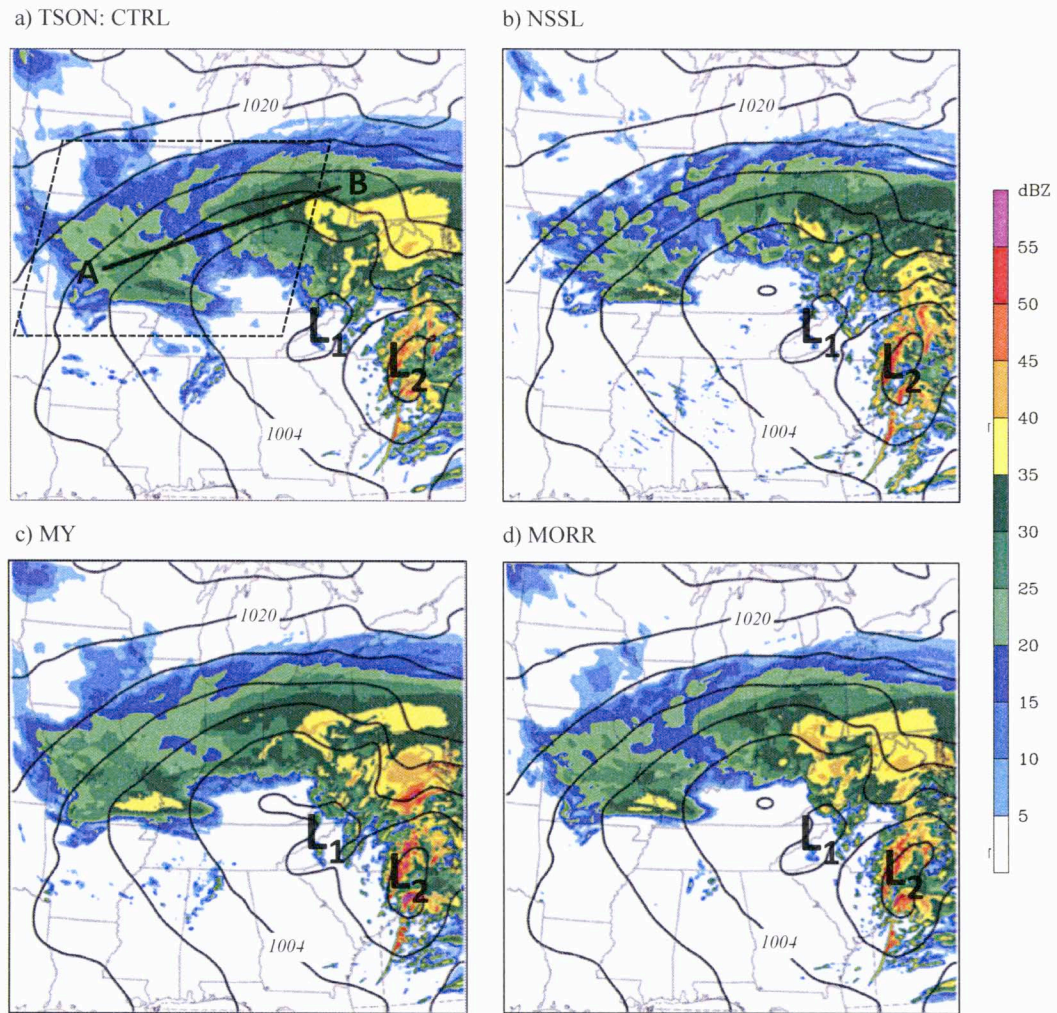


Figure 3.7: Maximum column reflectivities (shaded) and sea-level pressure (hPa; solid) at 0300 UTC on 6 Feb 2010 for (a) Thompson, (b) NSSL, (c) Milbrandt-Yau, and (d) Morrison. The pressure contours are in intervals of 4 hPa and the reflectivity scale is shown on the right. The dashed parallelogram indicates the volume-integrated area for individual hydrometeor mixing ratios.

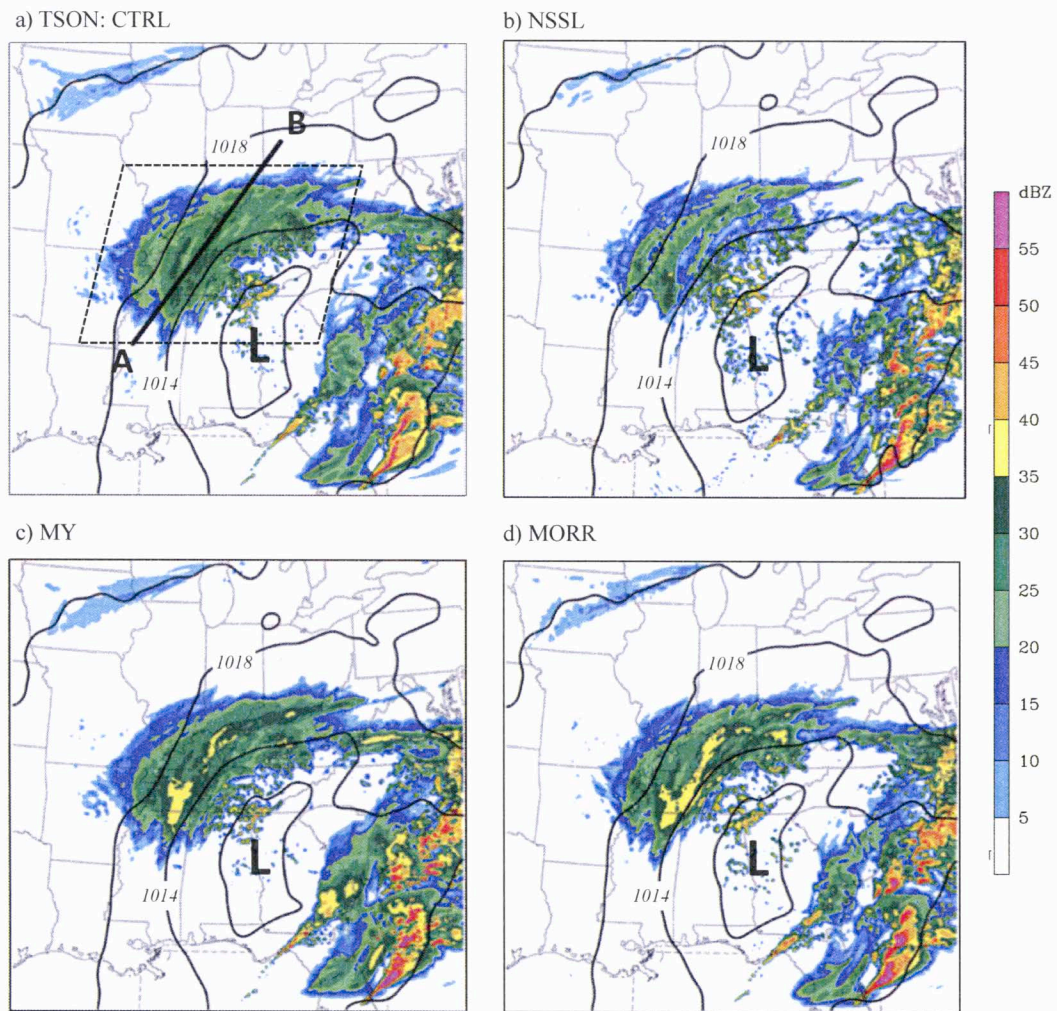


Figure 3.8: Maximum column reflectivities (shaded) and sea-level pressure (hPa; solid) at 0300 UTC on 26 Jan 2011 for (a) Thompson, (b) NSSL, (c) Milbrandt-Yau, and (d) Morrison. The pressure contours are in intervals of 4 hPa and the reflectivity scale is shown on the right. The dashed parallelogram indicates the volume-integrated area for individual hydrometeor mixing ratios.

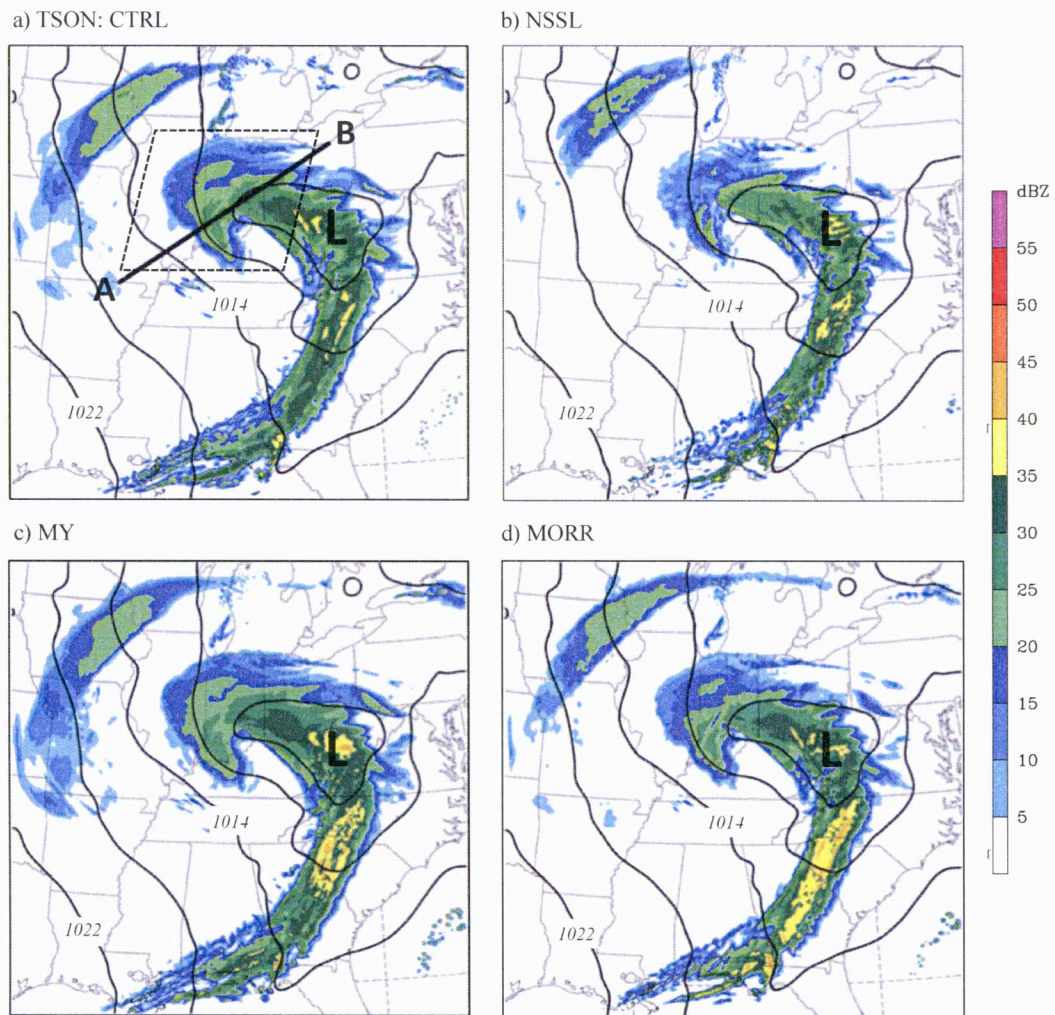


Figure 3.9: Maximum column reflectivities (shaded) and sea-level pressure (hPa; solid) at 1500 UTC on 15 Feb 2010 for (a) Thompson, (b) NSSL, (c) Milbrandt-Yau, and (d) Morrison. The pressure contours are in intervals of 4 hPa and the reflectivity scale is shown on the right. The dashed parallelogram indicates the volume-integrated area for individual hydrometeor mixing ratios.

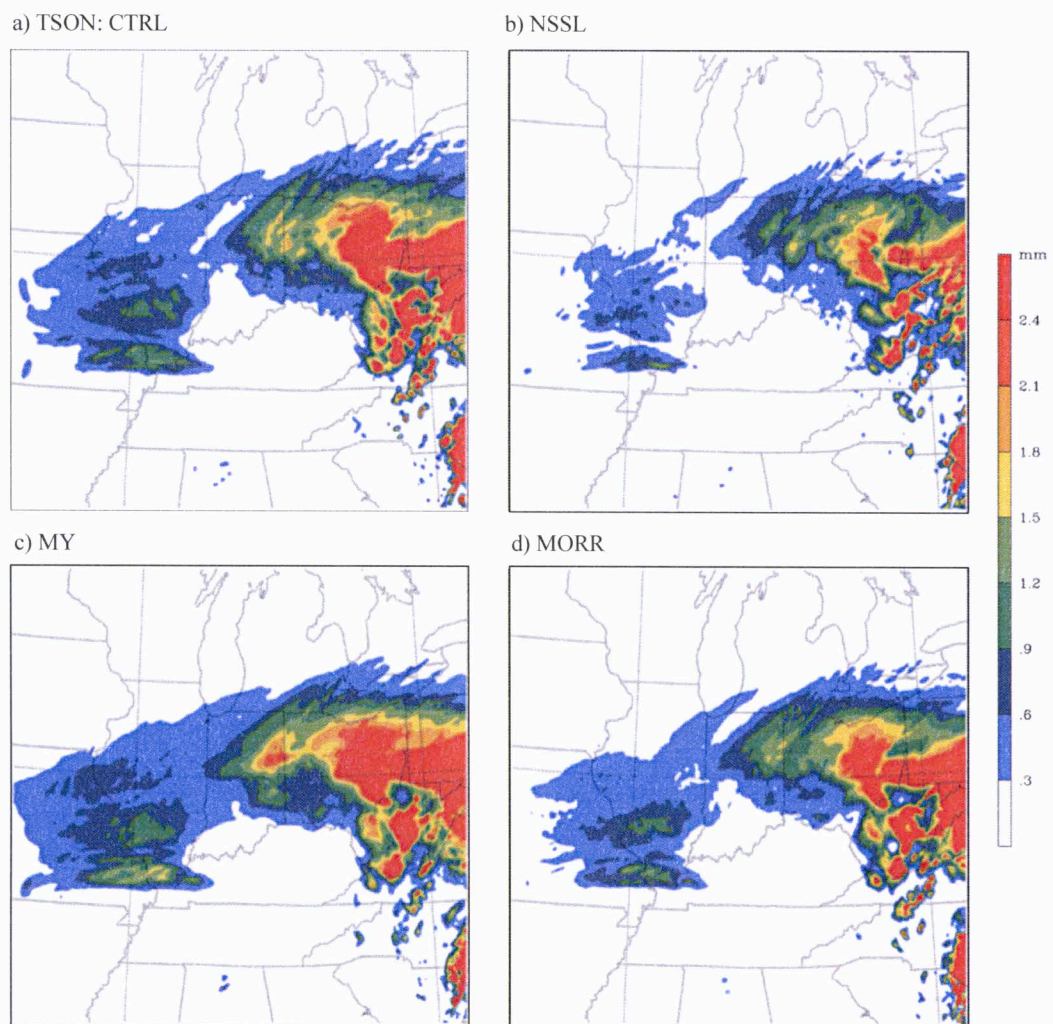


Figure 3.10: Column-integrated precipitation mass (mm; shaded) at 0300 6 Feb 2010 for (a) Thompson, (b) NSSL, (c) Milbrandt-Yau, and (d) Morrison.

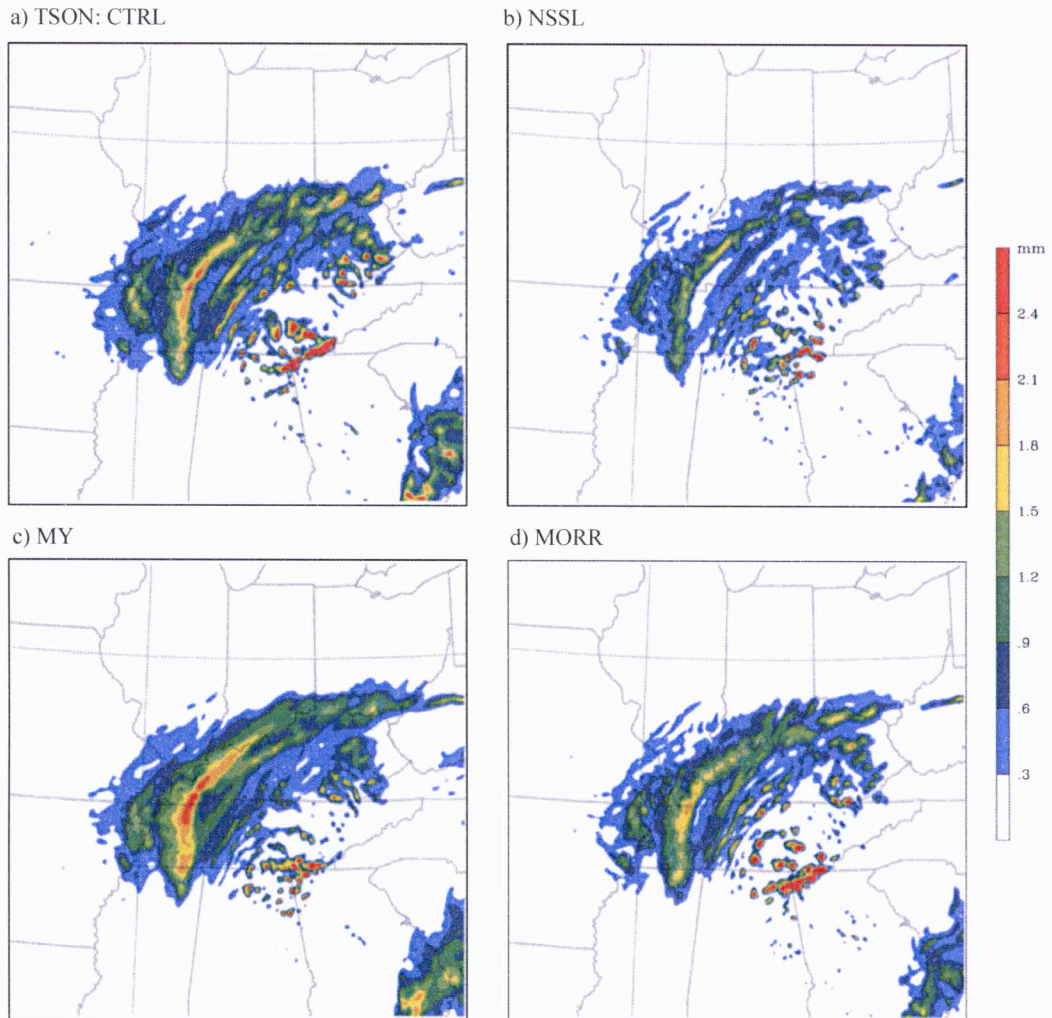


Figure 3.11: Column-integrated precipitation mass (mm; shaded) at 0300 26 Jan 2011 for (a) Thompson, (b) NSSL, (c) Milbrandt-Yau, and (d) Morrison.

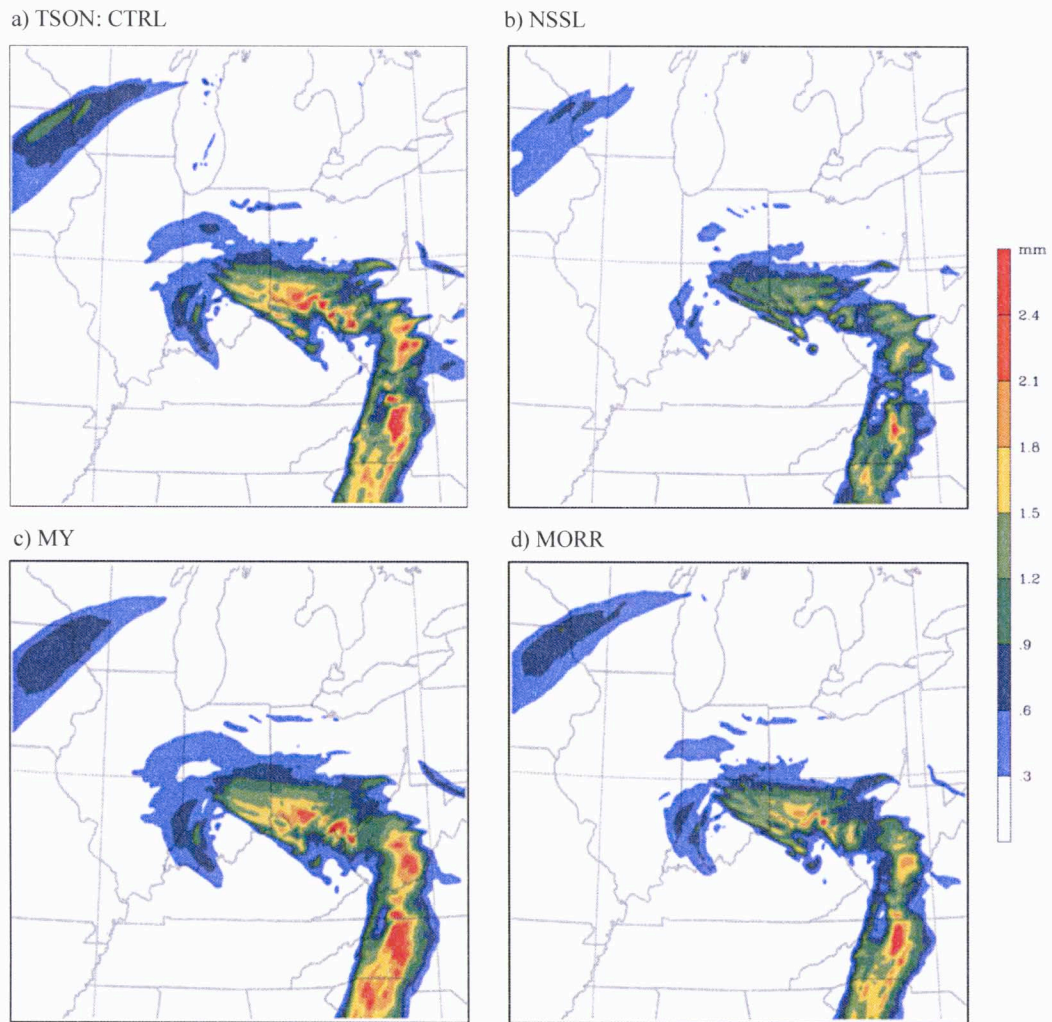


Figure 3.12: Column-integrated precipitation mass (mm; shaded) at 1500 15 Feb 2010 for (a) Thompson, (b) NSSL, (c) Milbrandt-Yau, and (d) Morrison.

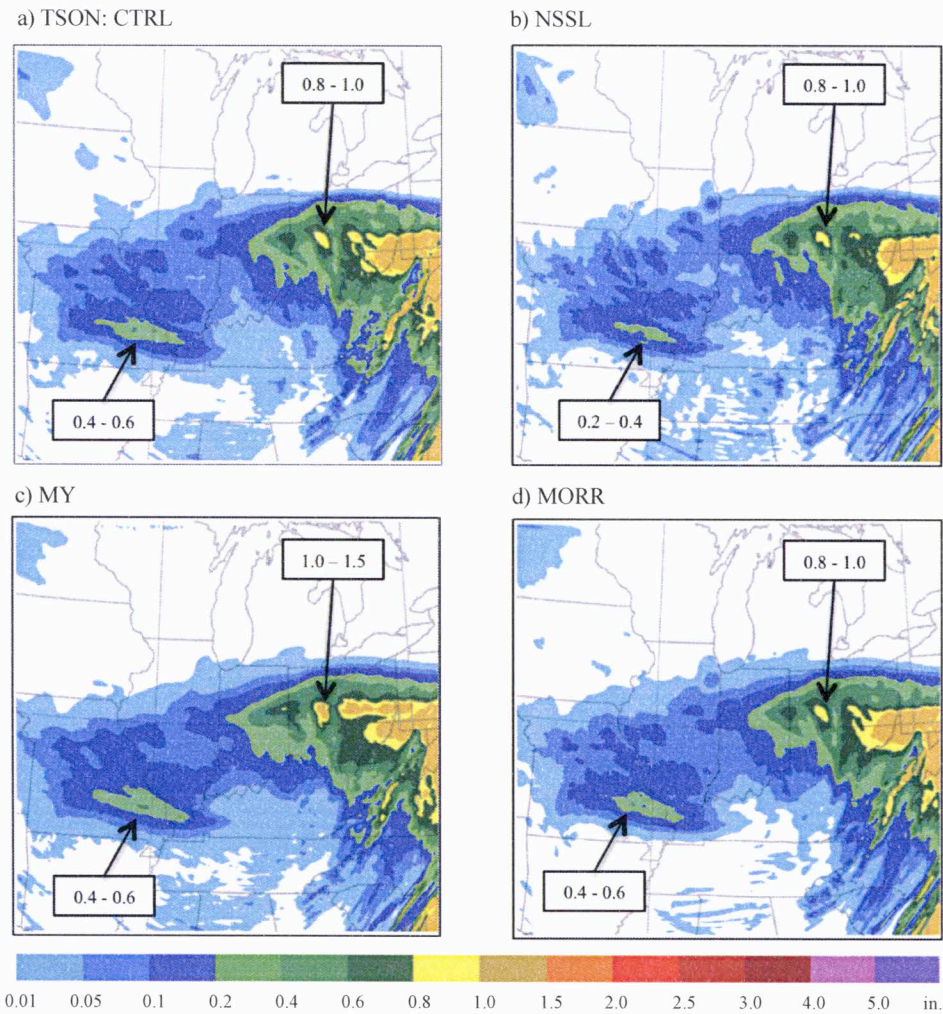


Figure 3.13: Total 6-h accumulated liquid equivalent precipitation (in; shaded) ending at 0600 6 Feb 2010 for (a) Thompson, (b) NSSL, (c) Milbrandt-Yau, and (d) Morrison. Local maxima in comma-head region is indicated for each scheme.

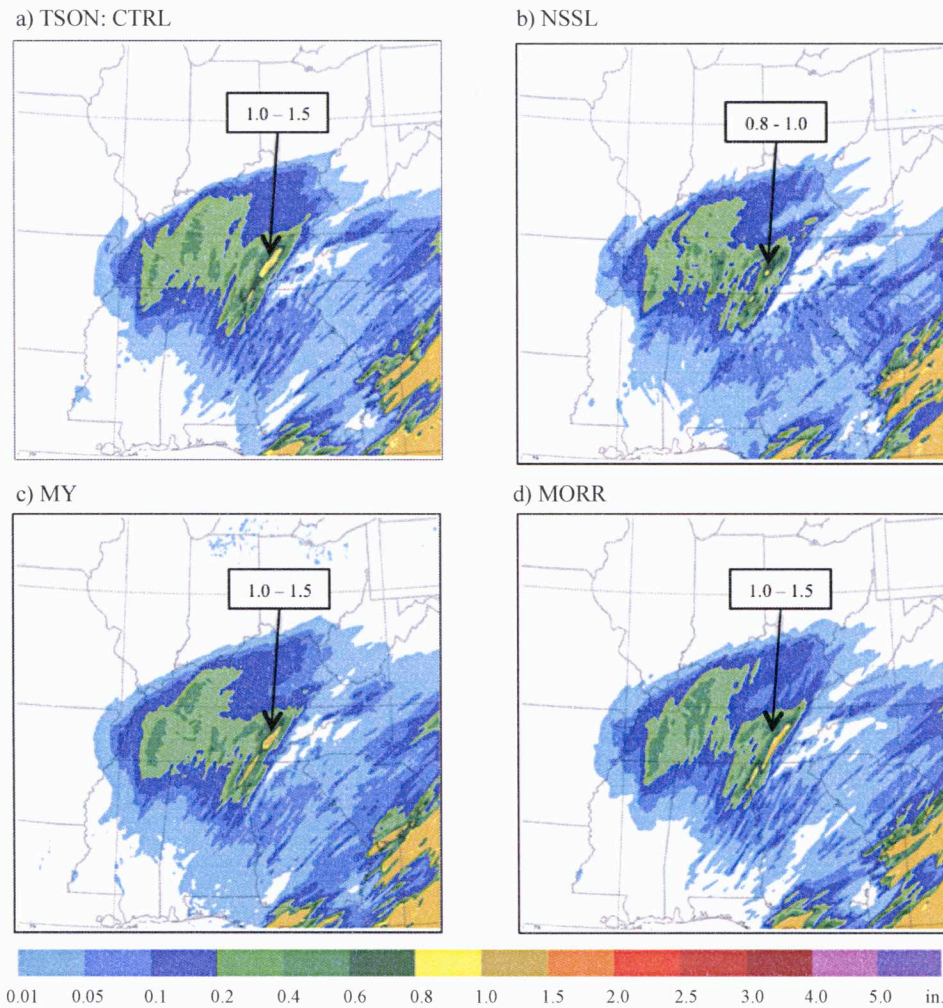


Figure 3.14: Total 6-h accumulated liquid equivalent precipitation (in; shaded) ending at 0600 26 Jan 2011 for (a) Thompson, (b) NSSL, (c) Milbrandt-Yau, and (d) Morrison. Local maxima in comma-head region is indicated for each scheme.

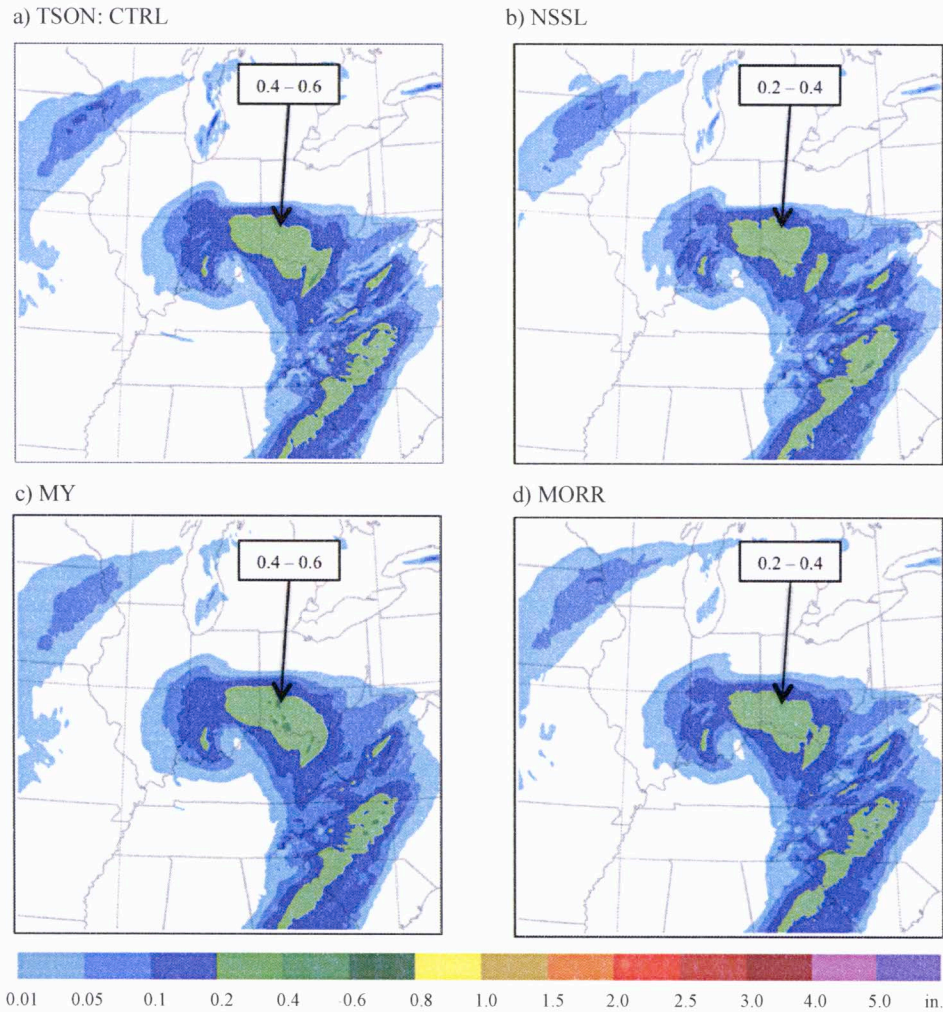


Figure 3.15: Total 6-h accumulated liquid equivalent precipitation (in; shaded) ending at 1800 15 Feb 2010 for (a) Thompson, (b) NSSL, (c) Milbrandt-Yau, and (d) Morrison. Local maxima in comma-head region is indicated for each scheme.

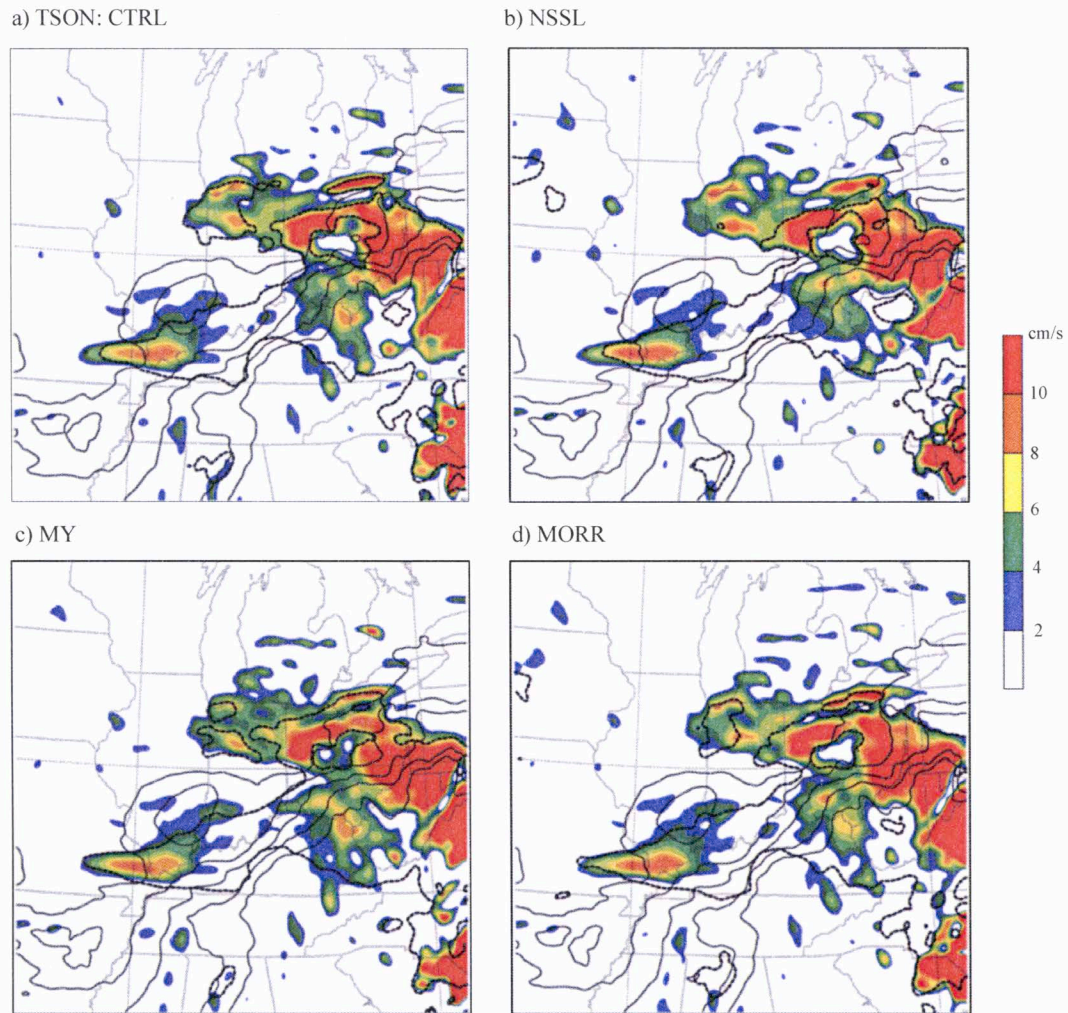


Figure 3.16: Vertical velocities (cm/s; shaded), temperature ranging from 264.5 to 269 (K; solid), and RH > 95% (%; dashed) at the 700-hPa geopotential level at 0300 UTC 6 Feb 2010 for (a) Thompson, (b) NSSL, (c) Milbrandt-Yau, and (d) Morrison. Temperature range between 264.5 and 269 K (1.5 K interval) is prime for hazardous icing conditions.

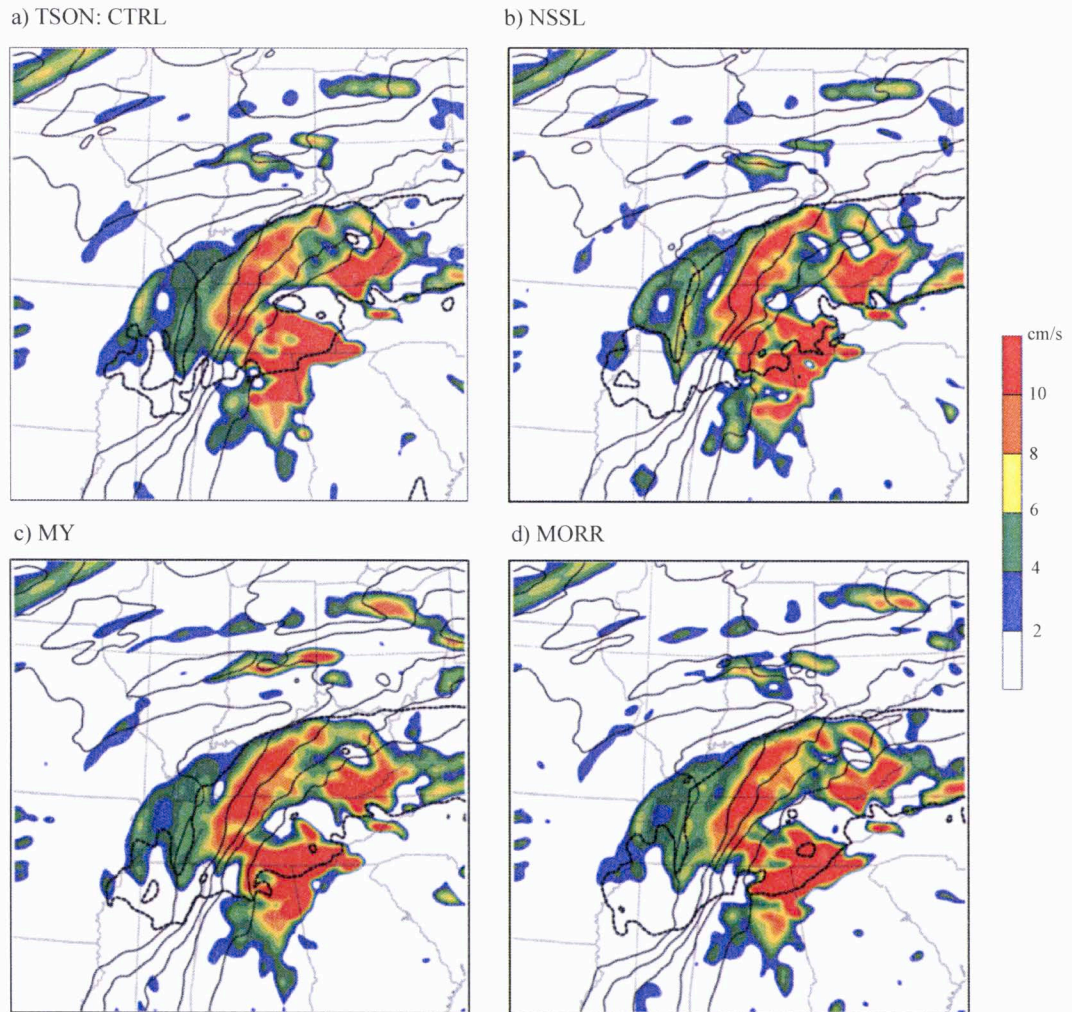


Figure 3.17: As in Fig. 3.16, but for 0300 UTC 26 Jan 2011.

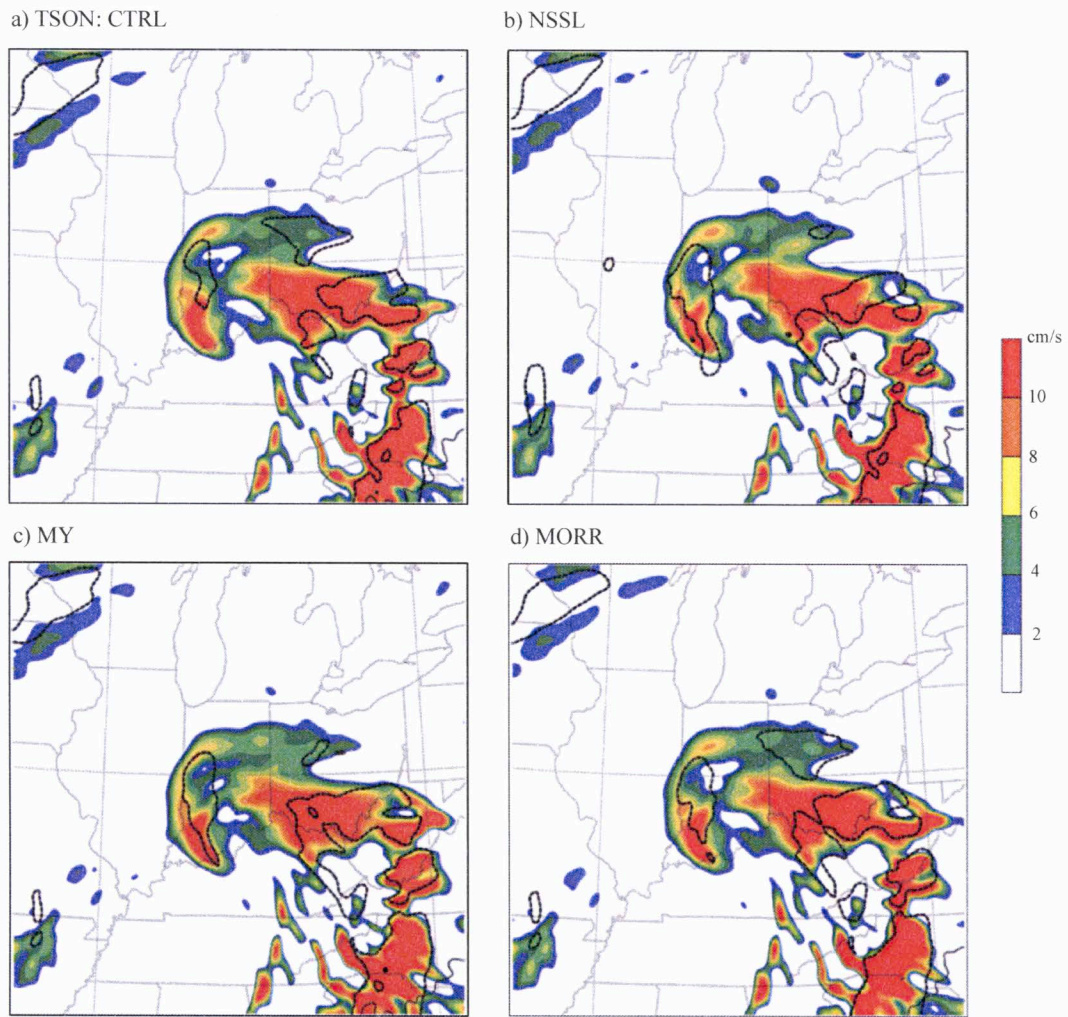


Figure 3.18: As in Fig. 3.16, but for 1500 UTC 15 Feb 2010.

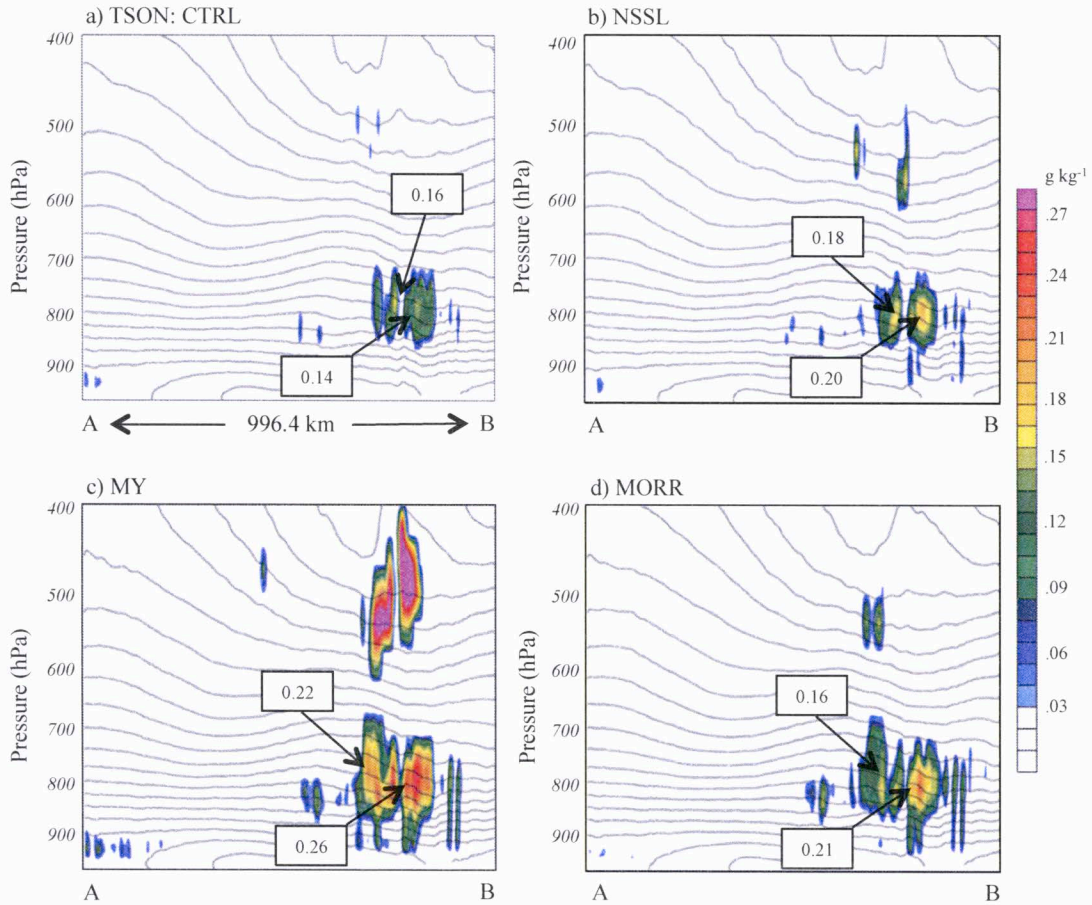


Figure 3.19: Vertical cross-sections (indicated in Fig 3.1a) of theta-e (K; solid) and cloud water mixing ratio (g/kg; shaded) at 0300 UTC on 6 Feb 2010 for (a) Thompson, (b) NSSL, (c) Milbrandt-Yau, and (d) Morrison.

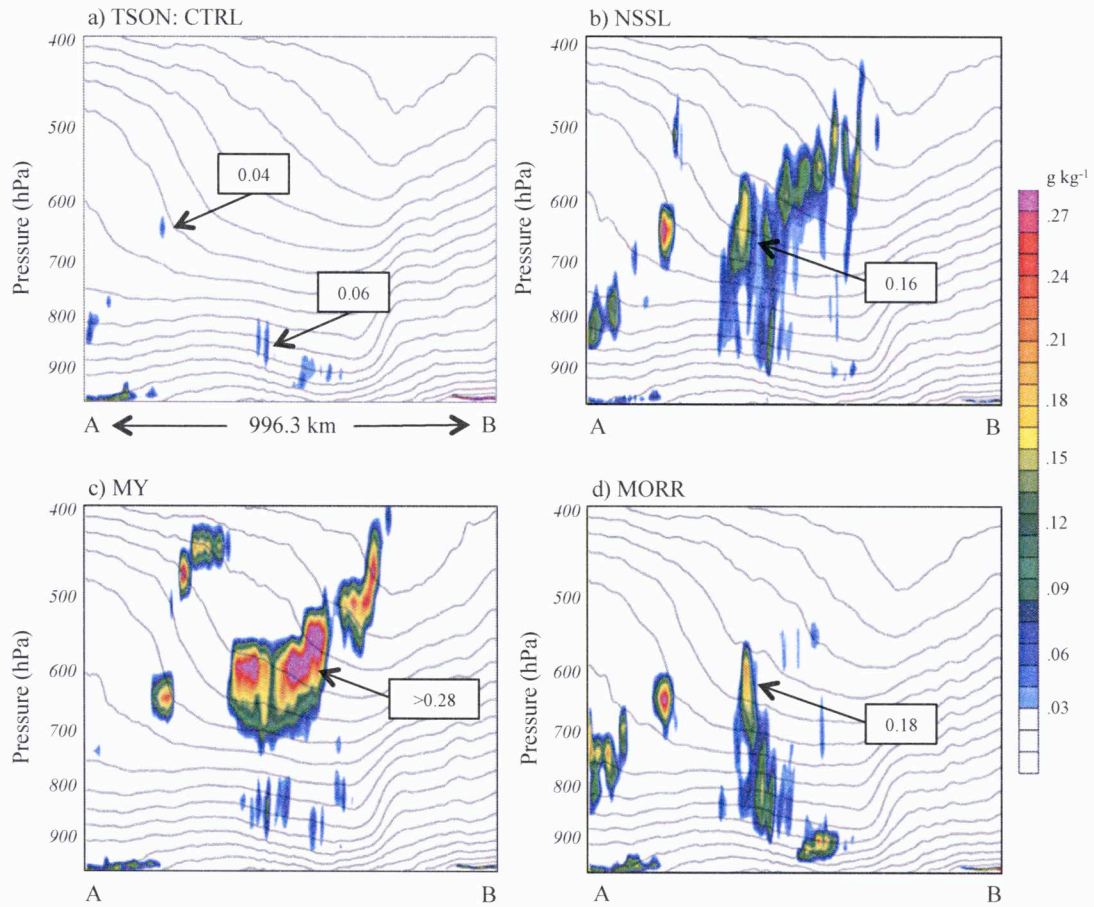


Figure 3.20: Vertical cross-sections (indicated in Fig 3.2a) of theta-e (K; solid) and cloud water mixing ratio (g/kg ; shaded) at 0300 UTC on 26 Jan 2011 for (a) Thompson, (b) NSSL, (c) Milbrandt-Yau, and (d) Morrison.

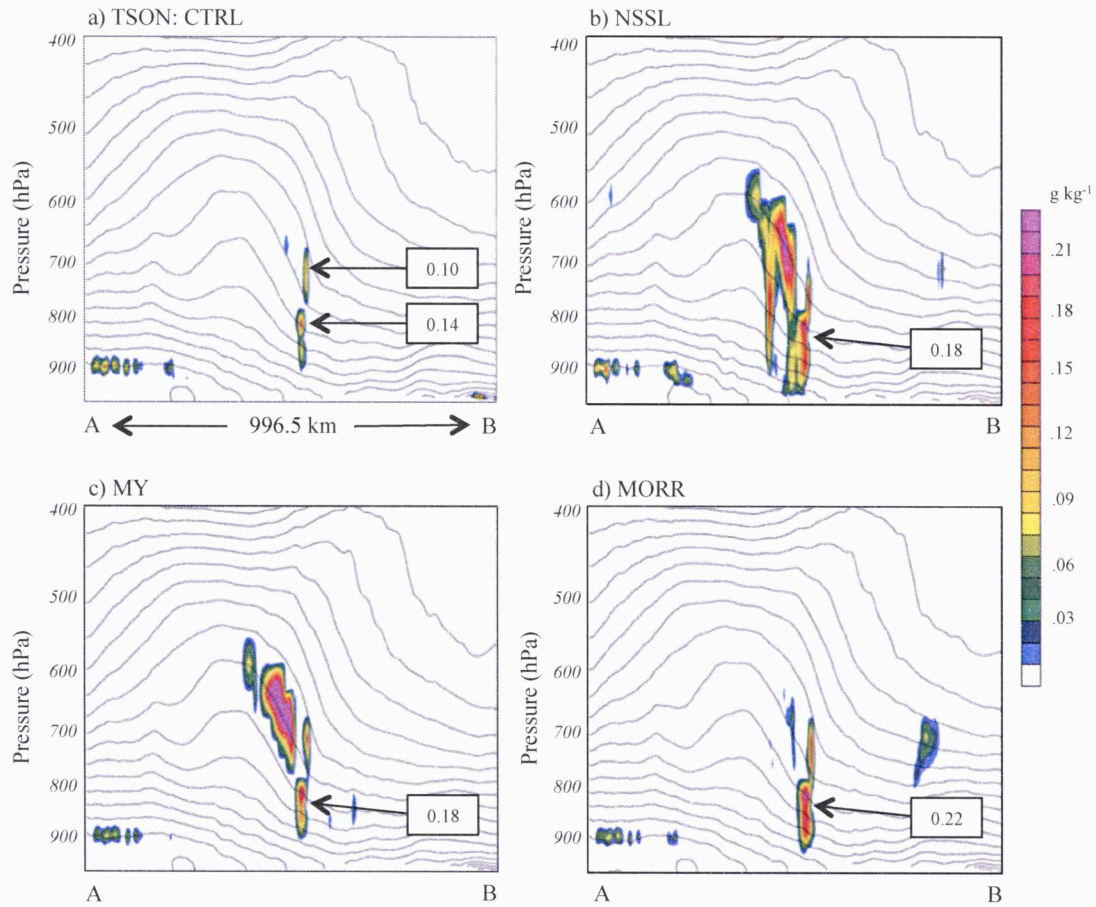
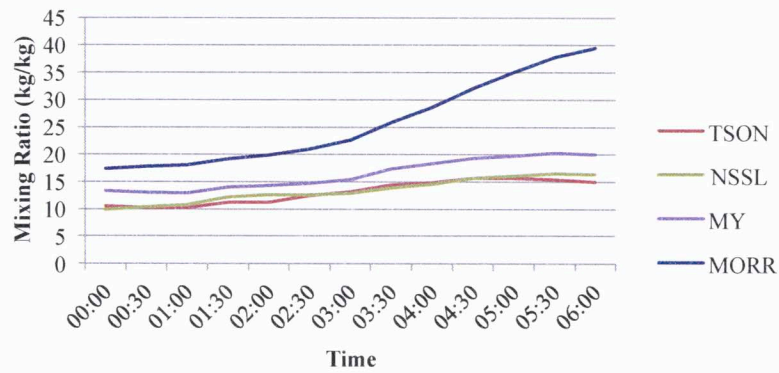
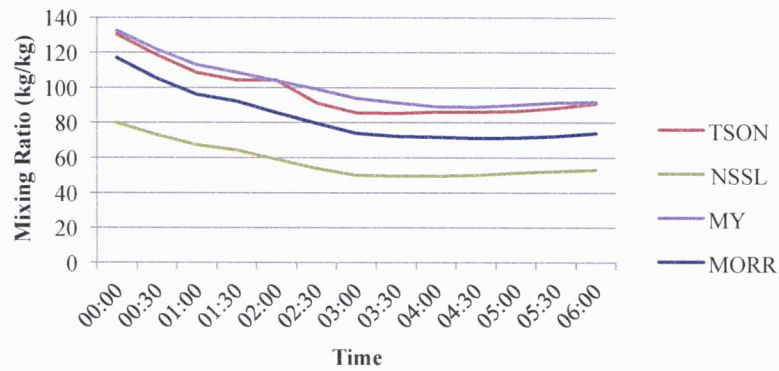


Figure 3.21: Vertical cross-sections (indicated in Fig 3.3a) of theta-e (K; solid) and cloud water mixing ratio (g/kg; shaded) at 1500 UTC on 15 Feb 2010 for (a) Thompson, (b) NSSL, (c) Milbrandt-Yau, and (d) Morrison.

a) Cloud Water Mixing Ratio (kg/kg)



b) Snow Mixing Ratio (kg/kg)



c) Total Hydrometeor Mixing Ratio (kg/kg)

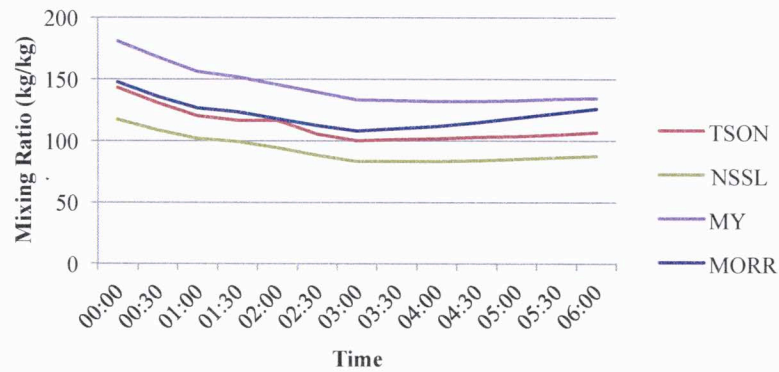
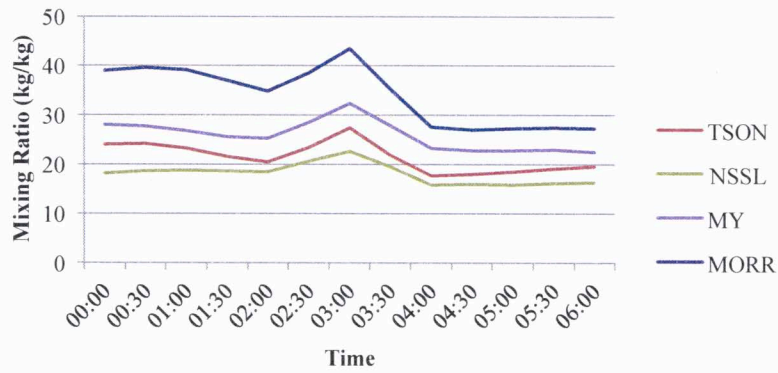
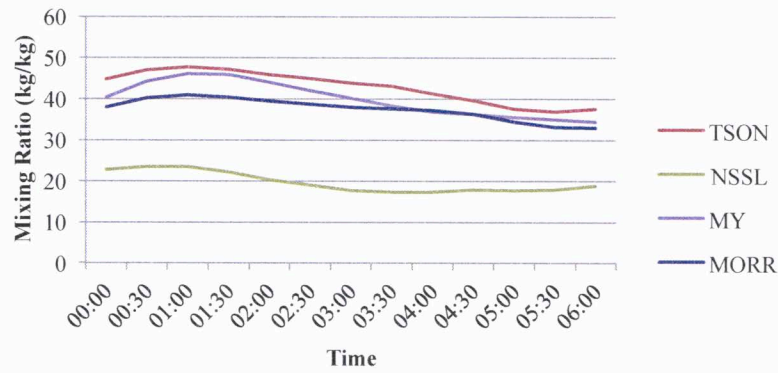


Figure 3.22: Sums of (a) cloud water, (b) snow, and (c) total hydrometeor mixing ratios (kg/kg) in the comma-head region for February 6, 2010 for the times indicated (in UTC).

a) Cloud Water Mixing Ratio (kg/kg)



b) Snow Mixing Ratio (kg/kg)



c) Total Hydrometeor Mixing Ratio (kg/kg)

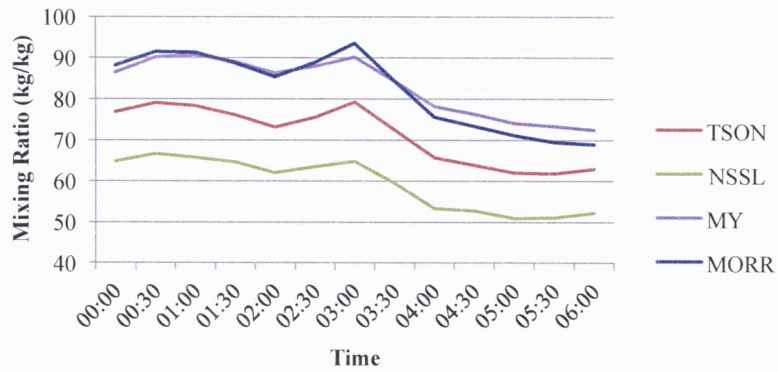
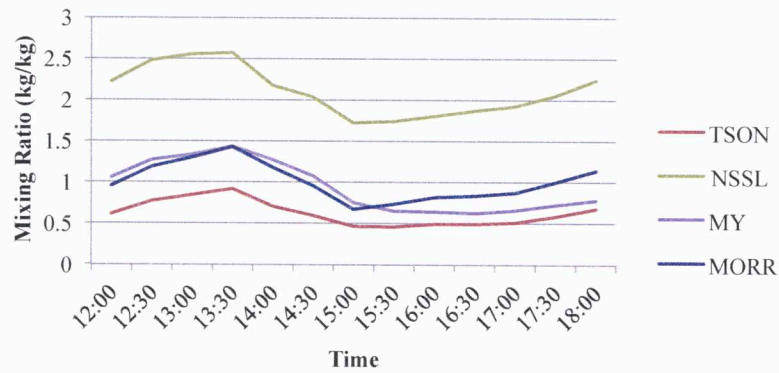
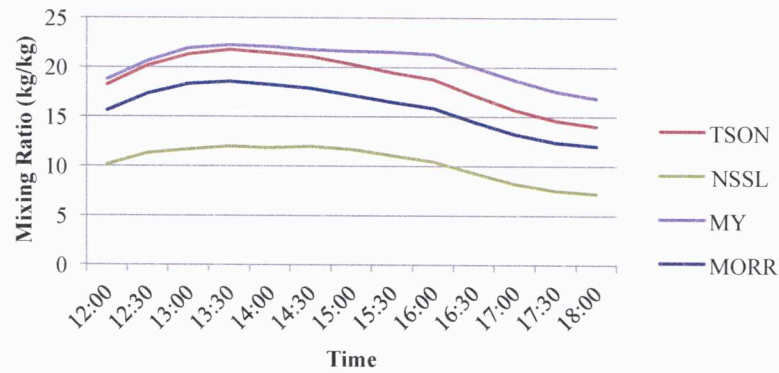


Figure 3.23: Sums of (a) cloud water, (b) snow, and (c) total hydrometeor mixing ratios (kg/kg) in the comma-head region for January 26, 2011 for the times indicated (in UTC).

a) Cloud Water Mixing Ratio (kg/kg)



b) Snow Mixing Ratio (kg/kg)



c) Total Hydrometeor Mixing Ratio (kg/kg)

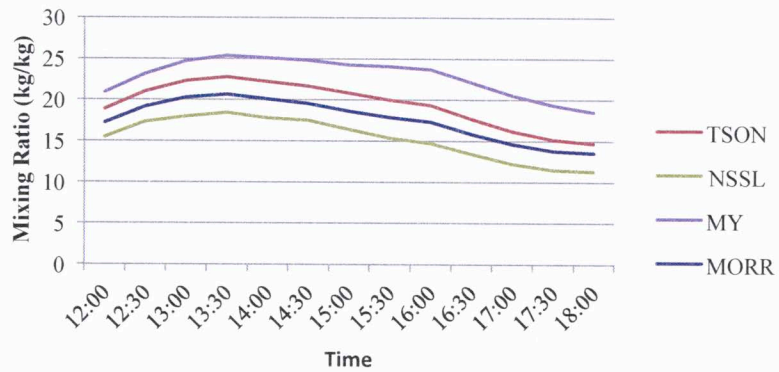


Figure 3.24: Sums of (a) cloud water, (b) snow, and (c) total hydrometeor mixing ratios (kg/kg) in the comma-head region for February 15, 2010 for the times indicated (in UTC).

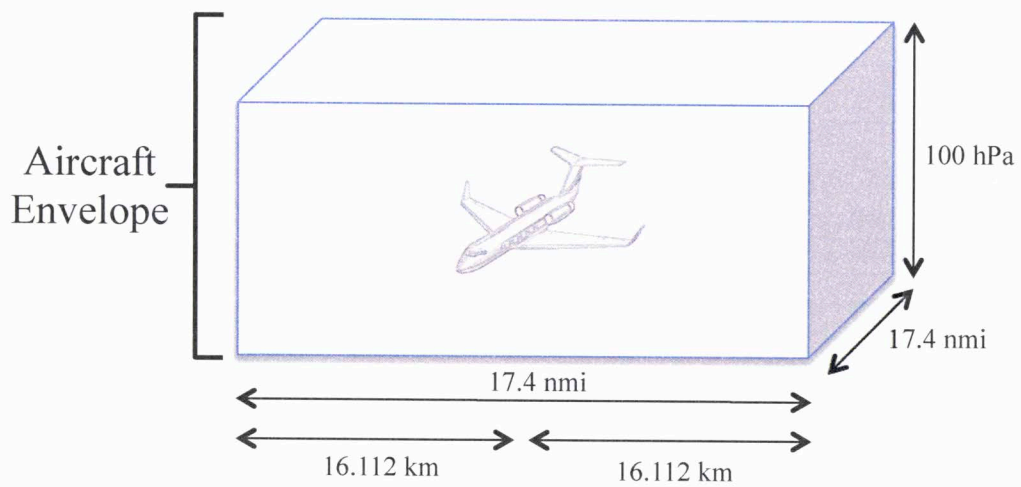


Figure 3.25: Aircraft envelope dimensions, per specifications from the FAA Airport and Aircraft Safety / Research and Development Icing Design Envelope Specification Final Report (April 2002).

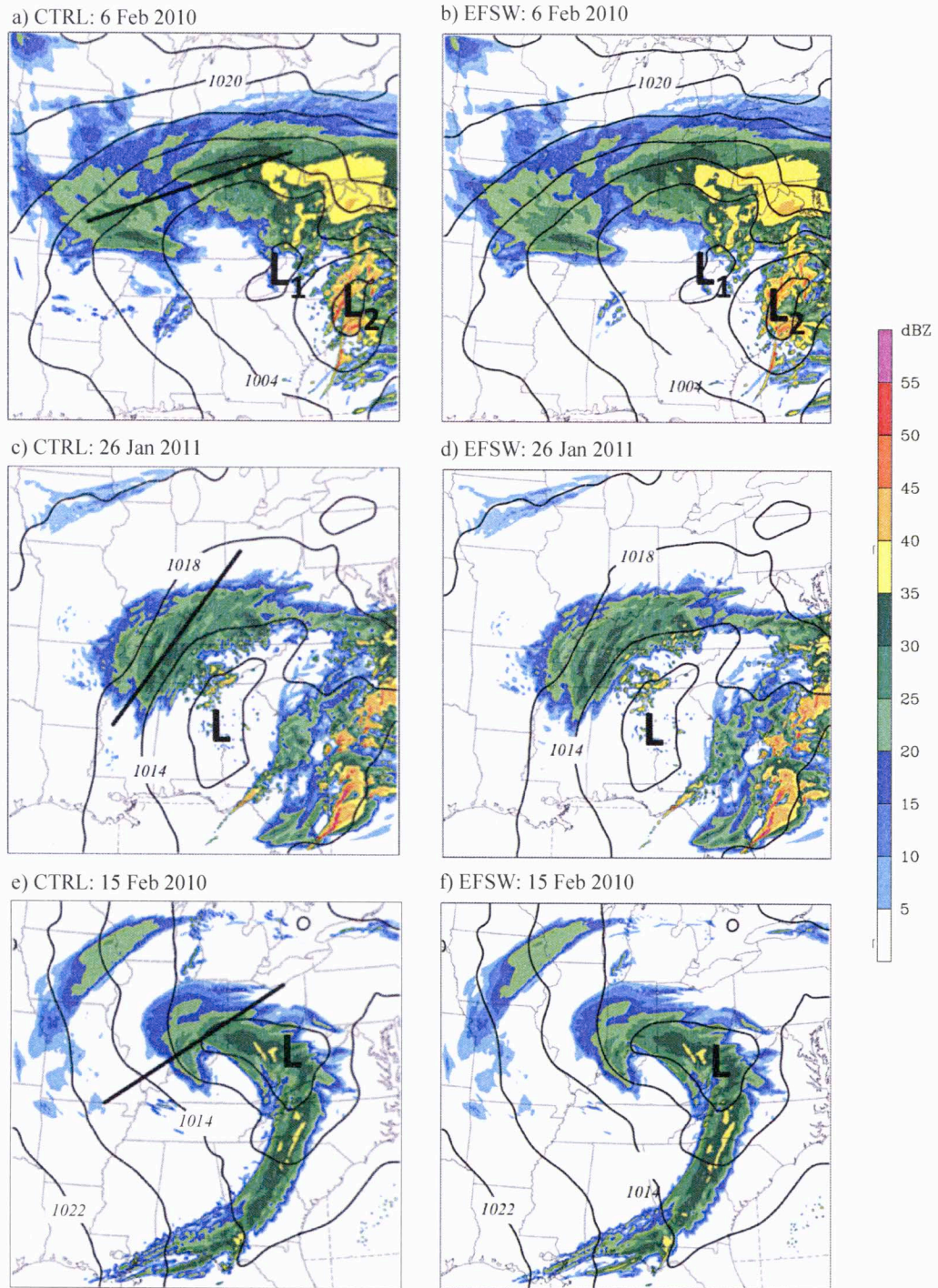


Figure 4.1: Maximum column reflectivities (shaded) and sea-level pressure (hPa; solid) at 0300 UTC 6 Feb 2010 for (a) CTRL, and (b) EFSW, at 0300 UTC 26 Jan 2011 for (c) CTRL, and (d) EFSW, and at 1500 UTC Feb 15 2010 for (e) CTRL, and (f) EFSW.

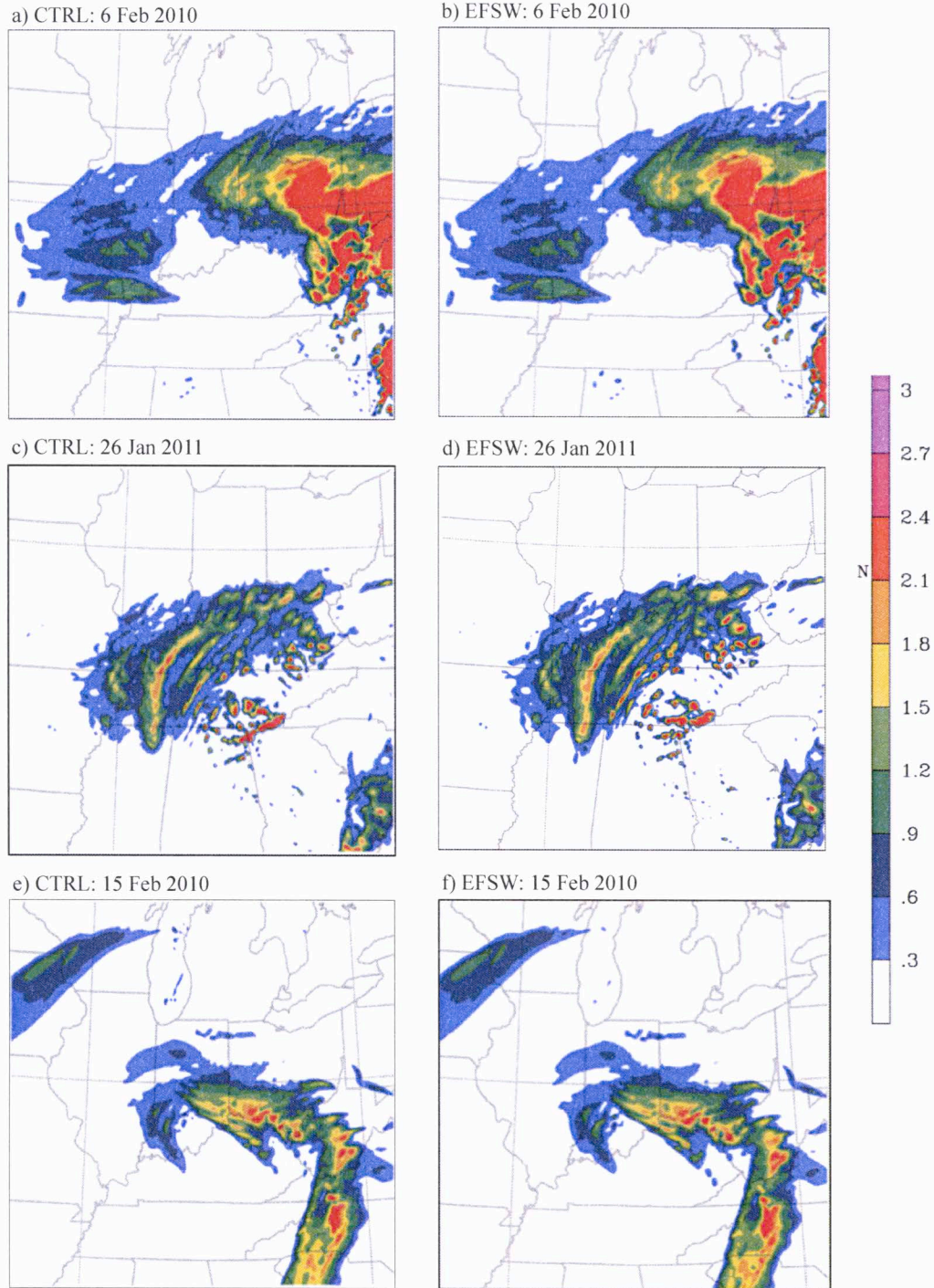


Figure 4.2: Column-integrated precipitation hydrometeors (mm; shaded) at 0300 UTC 6 Feb 2010 for (a) CTRL, and (b) EFSW, at 0300 UTC 26 Jan 2011 for (c) CTRL, and (d) EFSW, and at 1500 UTC Feb 15 2010 for (e) CTRL, and (f) EFSW.

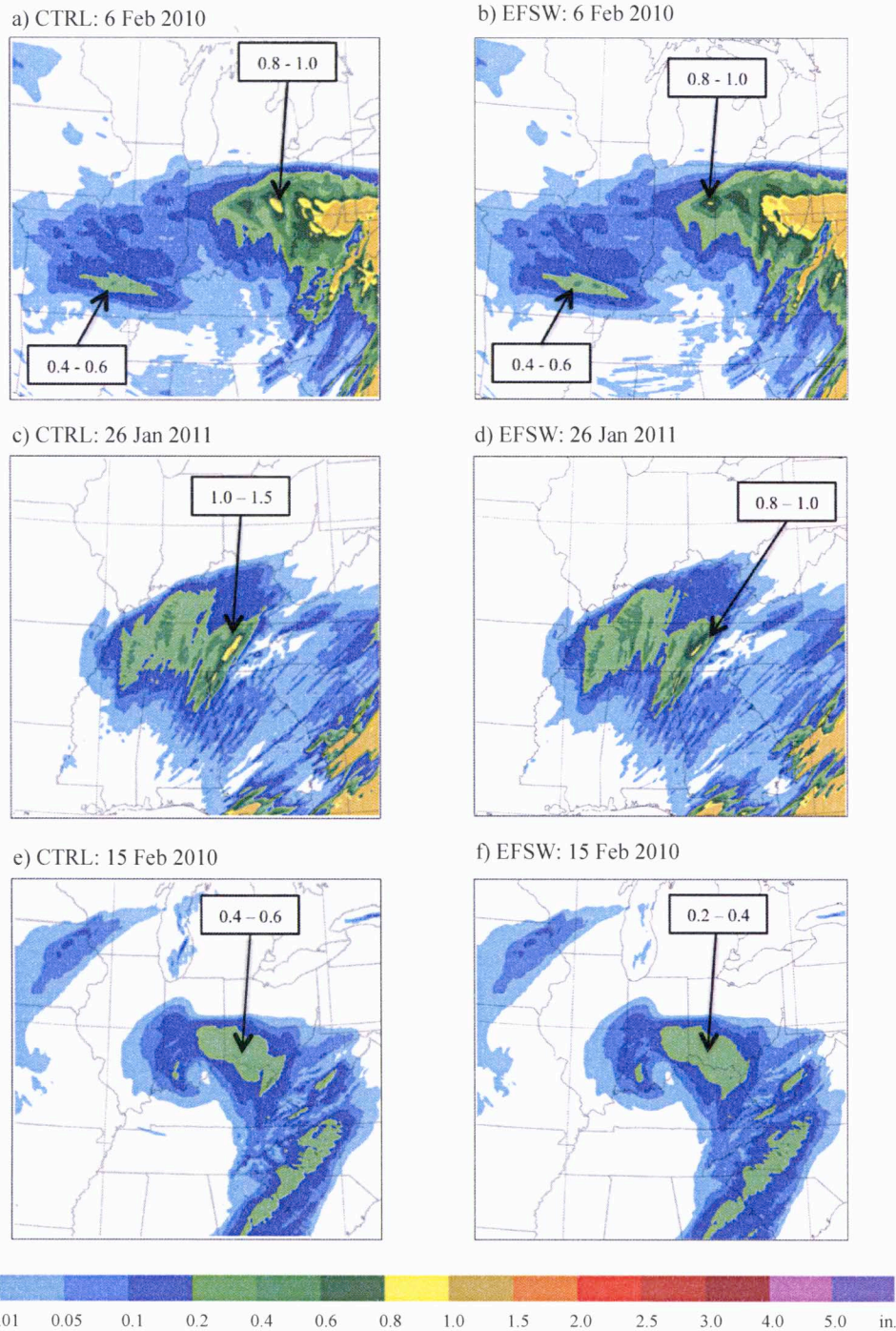


Figure 4.3: Total 6-h accumulated liquid equivalent precipitation (in; shaded) ending at 0600 UTC 6 Feb 2010 for (a) CTRL, and (b) EFSW, at 0600 UTC 26 Jan 2011 for (c) CTRL, and (d) EFSW, and at 1800 UTC Feb 15 2010 for (e) CTRL, and (f) EFSW.

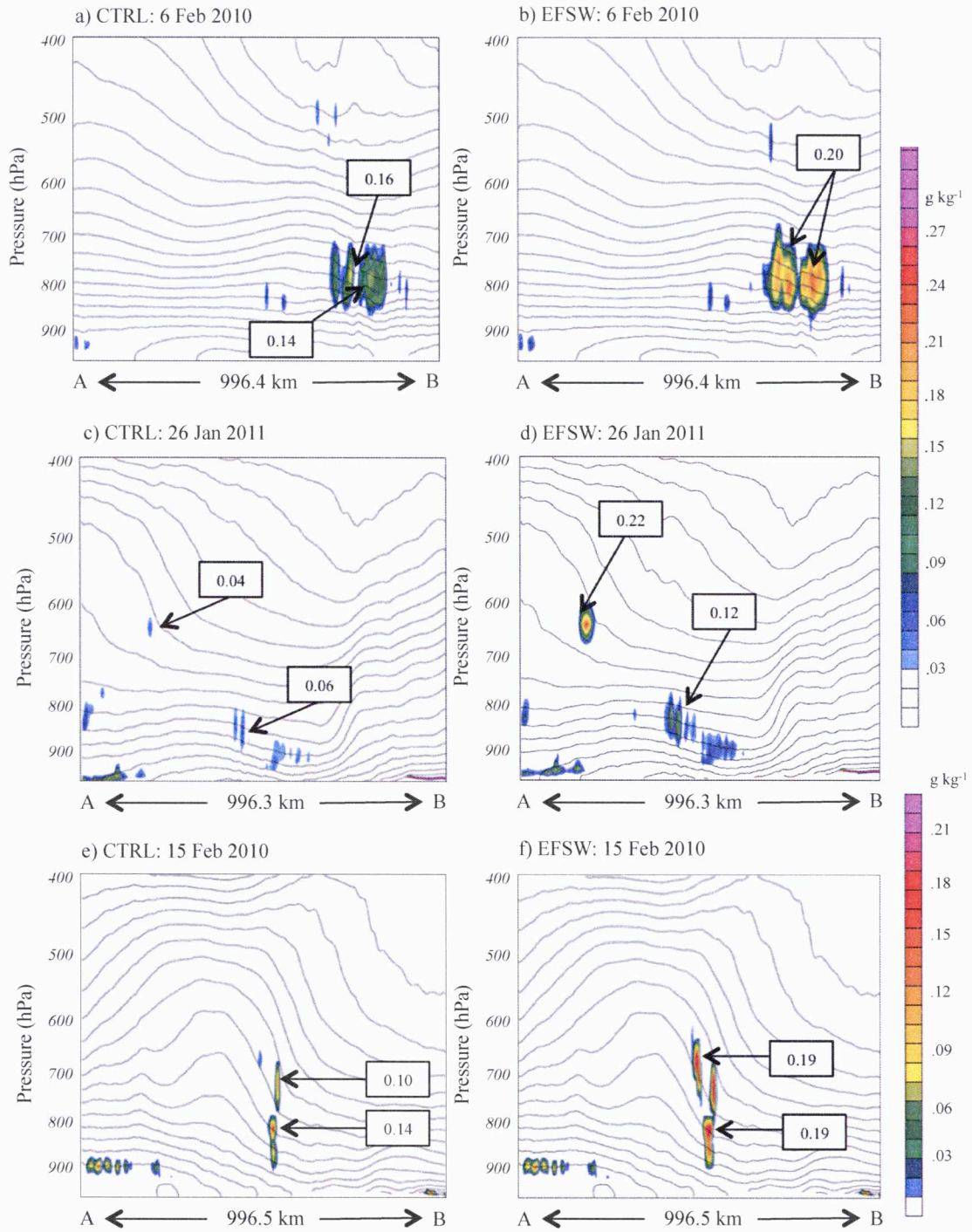


Figure 4.4: EFSW vertical cross-sections of θ_e (K; solid) and cloud water mixing ratio (g/kg; shaded) at 0300 UTC 6 Feb 2010 for (a) CTRL, and (b) EFSW, at 0300 UTC 26 Jan 2011 for (c) CTRL, and (d) EFSW, and at 1500 UTC Feb 15 2010 for (e) CTRL, and (f) EFSW.

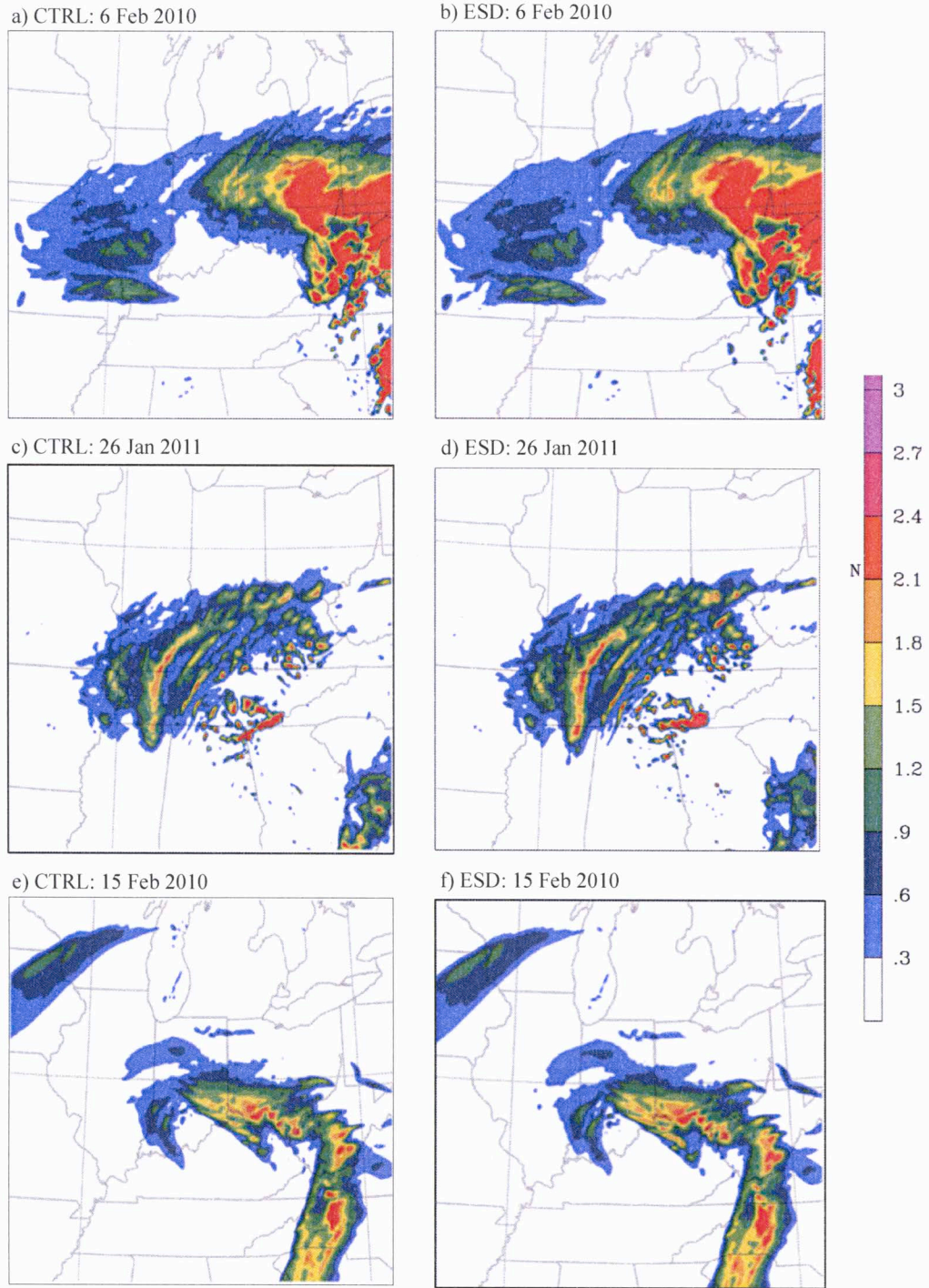


Figure 4.5: Column-integrated precipitation hydrometeors (mm; shaded) at 0300 UTC 6 Feb 2010 for (a) CTRL, and (b) ESD, at 0300 UTC 26 Jan 2011 for (c) CTRL, and (d) ESD, and at 1500 UTC Feb 15 2010 for (e) CTRL, and (f) ESD.

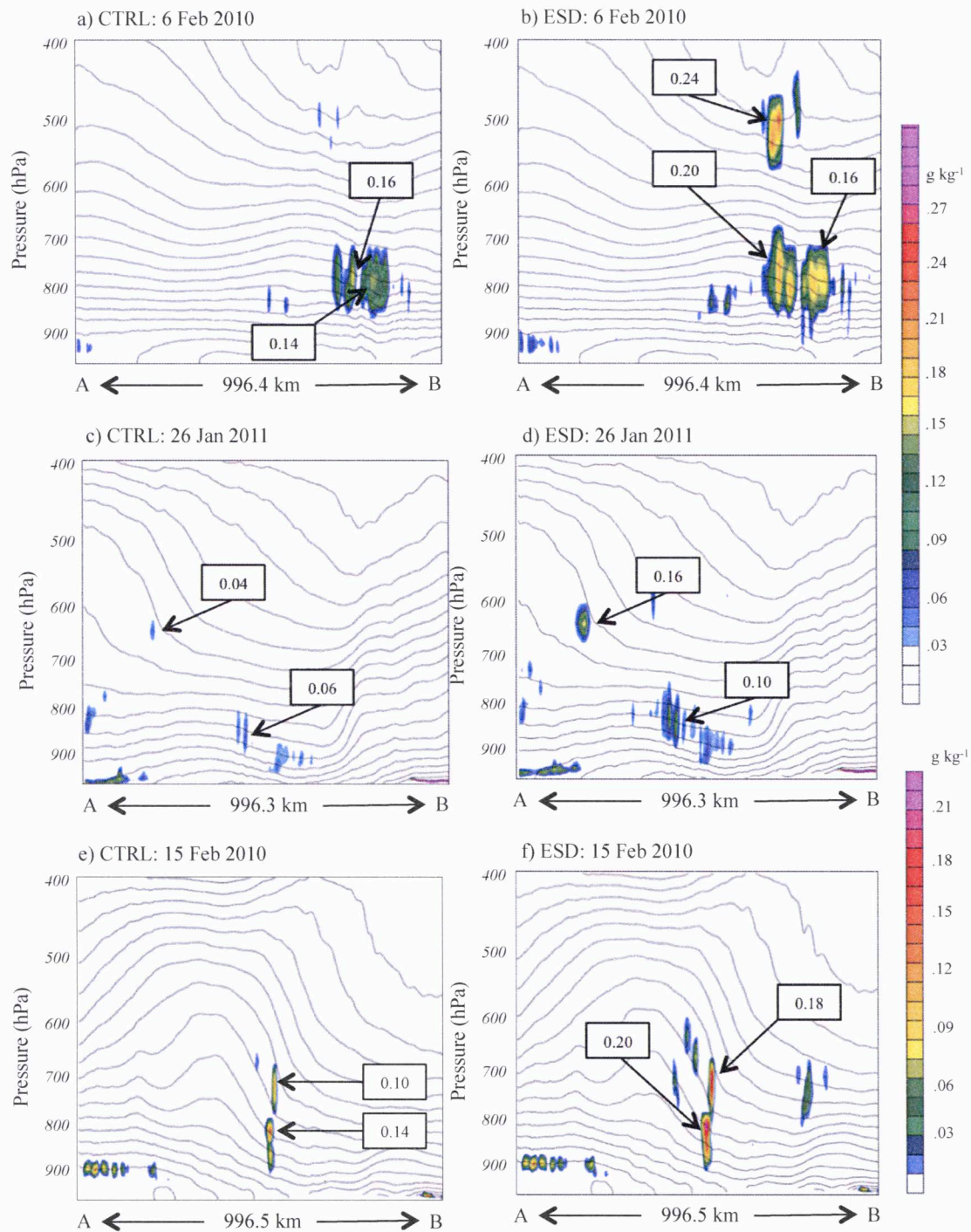


Figure 4.6: ESD vertical cross-sections of θ_e (K; solid) and cloud water mixing ratio (g/kg ; shaded) at 0300 UTC 6 Feb 2010 for (a) CTRL, and (b) ESD, at 0300 UTC 26 Jan 2011 for (c) CTRL, and (d) ESD, and at 1500 UTC Feb 15 2010 for (e) CTRL, and (f) ESD.

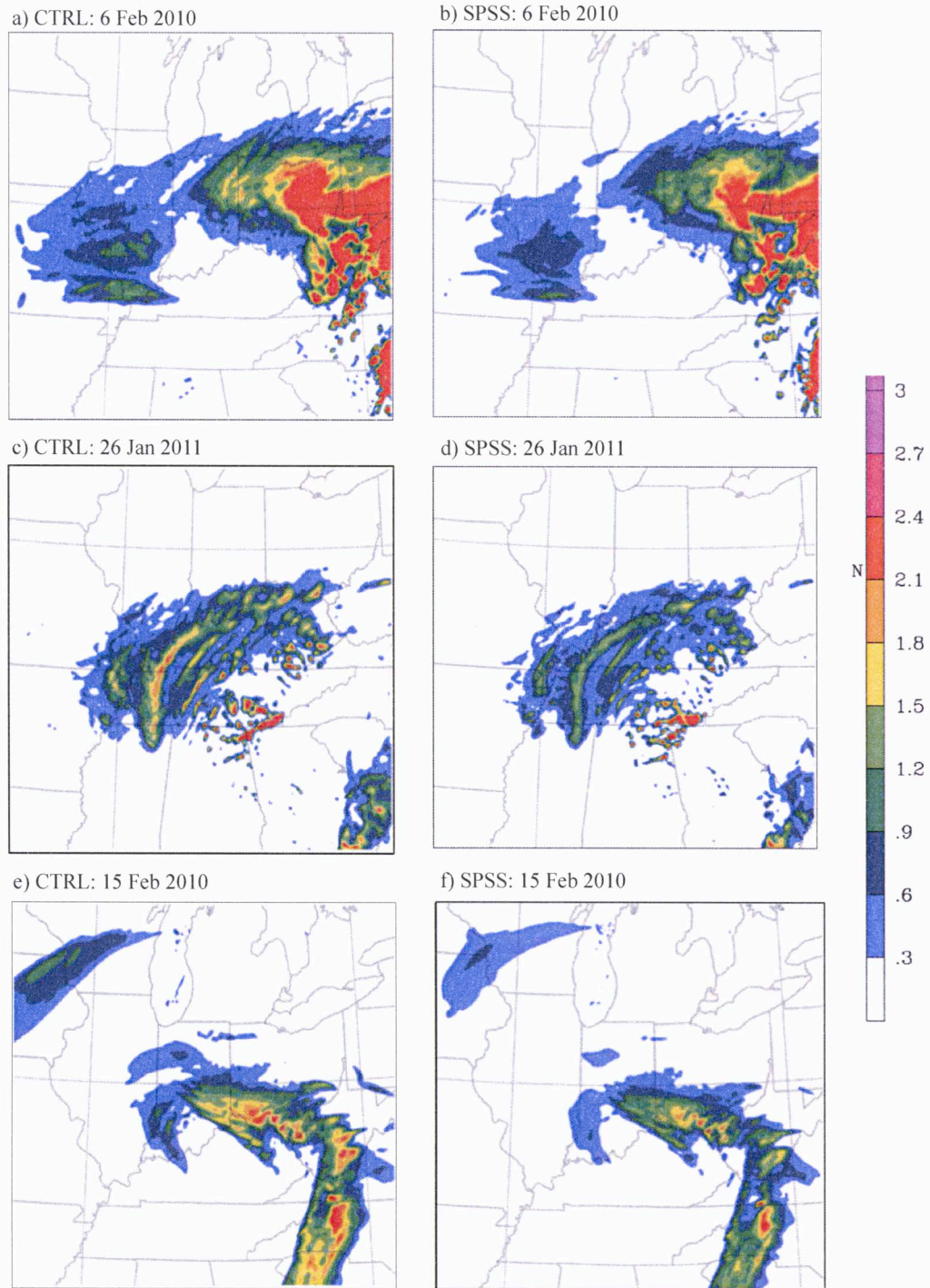


Figure 4.7: Column-integrated precipitation hydrometeors (mm; shaded) at 0300 UTC 6 Feb 2010 for (a) CTRL, and (b) SPSS, at 0300 UTC 26 Jan 2011 for (c) CTRL, and (d) SPSS, and at 1500 UTC Feb 15 2010 for (e) CTRL, and (f) SPSS.

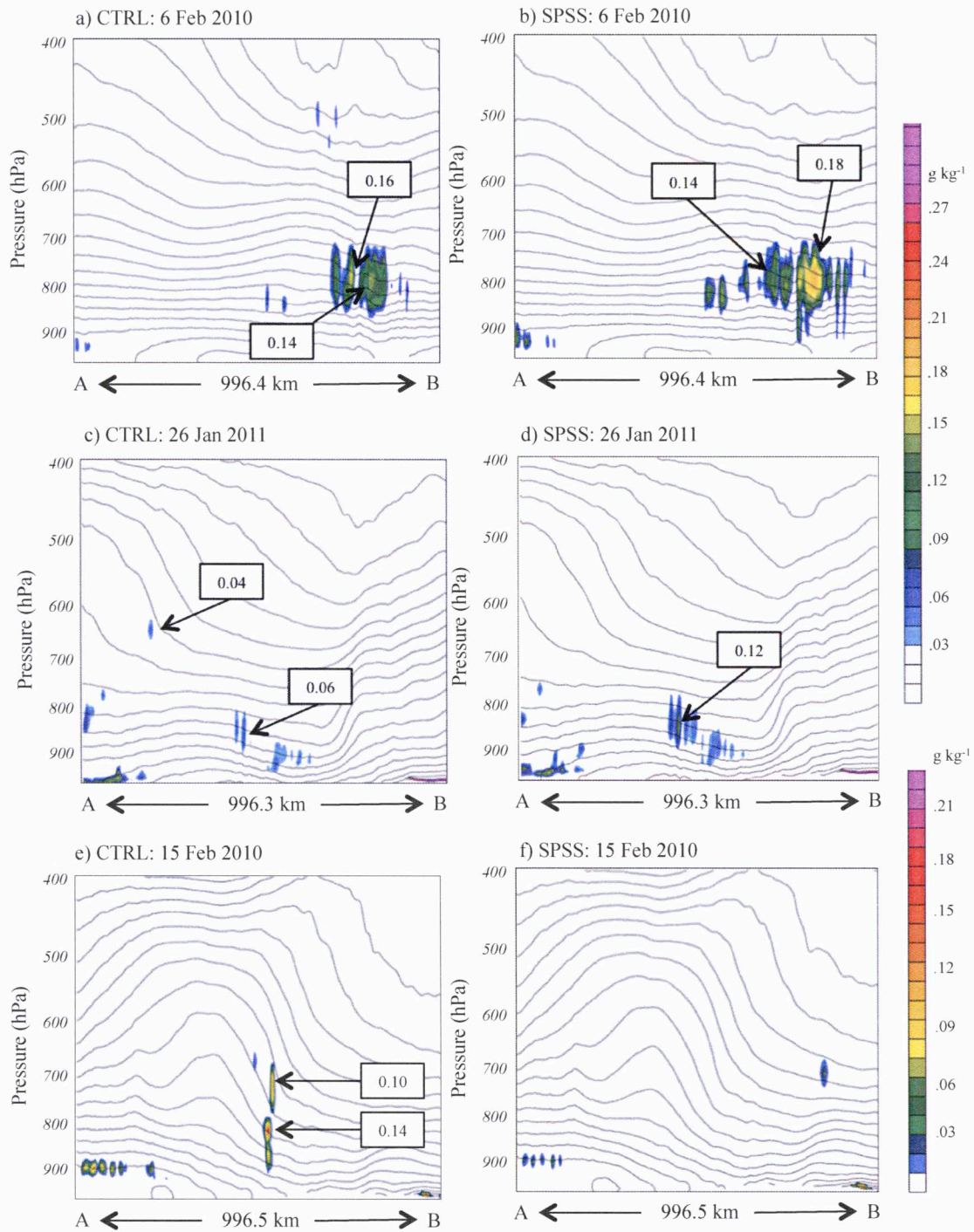


Figure 4.8: SPSS vertical cross-sections of θ_e (K; solid) and cloud water mixing ratio (g/kg; shaded) at 0300 UTC 6 Feb 2010 for (a) CTRL, and (b) SPSS, at 0300 UTC 26 Jan 2011 for (c) CTRL, and (d) SPSS, and at 1500 UTC Feb 15 2010 for (e) CTRL, and (f) SPSS.

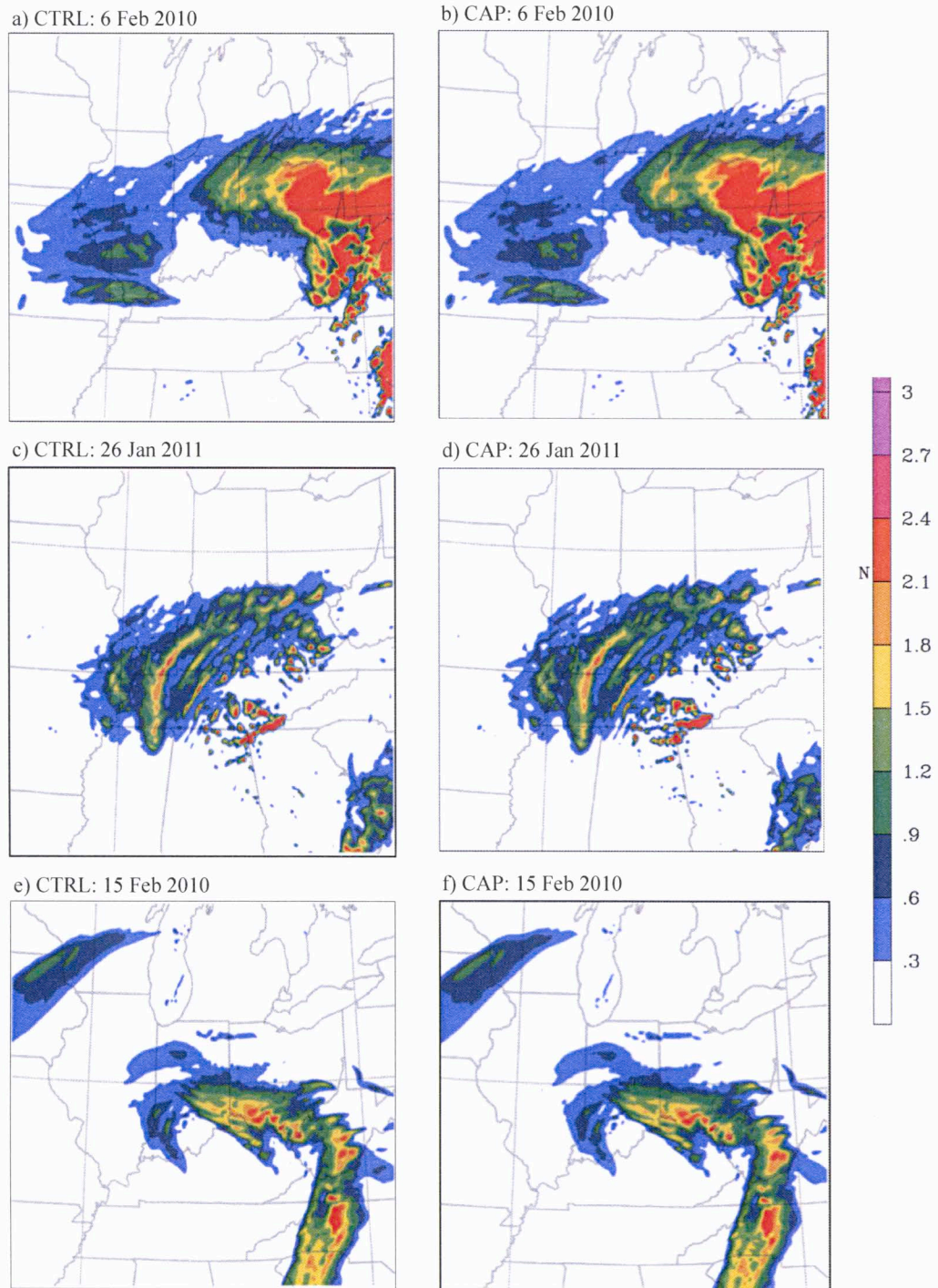


Figure 4.9: Column-integrated precipitation hydrometeors (mm; shaded) at 0300 UTC 6 Feb 2010 for (a) CTRL, and (b) CAP, at 0300 UTC 26 Jan 2011 for (c) CTRL, and (d) CAP, and at 1500 UTC Feb 15 2010 for (e) CTRL, and (f) CAP.

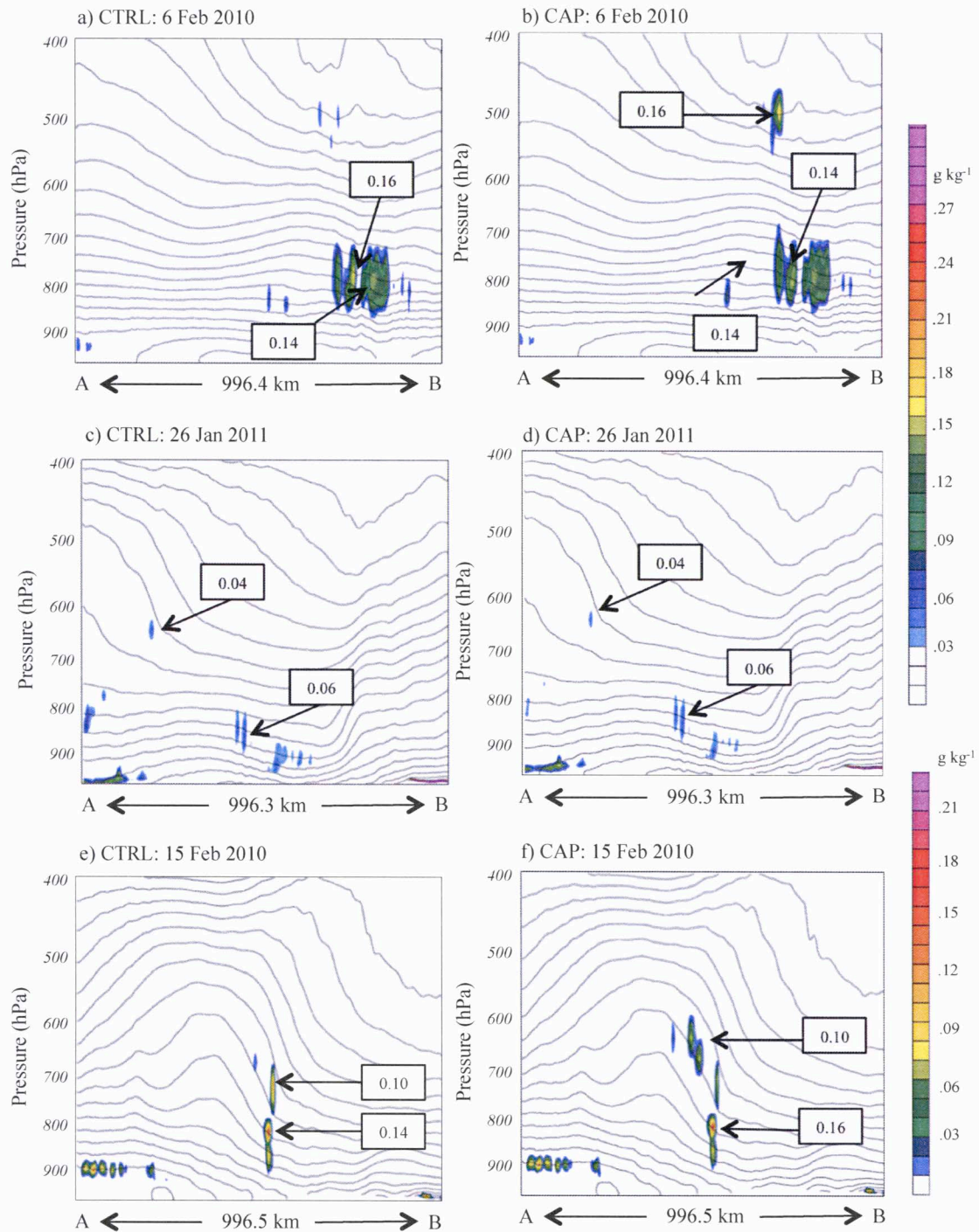


Figure 4.10: CAP vertical cross-sections of θ_e (K; solid) and cloud water mixing ratio (g/kg; shaded) at 0300 UTC 6 Feb 2010 for (a) CTRL, and (b) CAP, at 0300 UTC 26 Jan 2011 for (c) CTRL, and (d) CAP, and at 1500 UTC Feb 15 2010 for (e) CTRL, and (f) CAP.

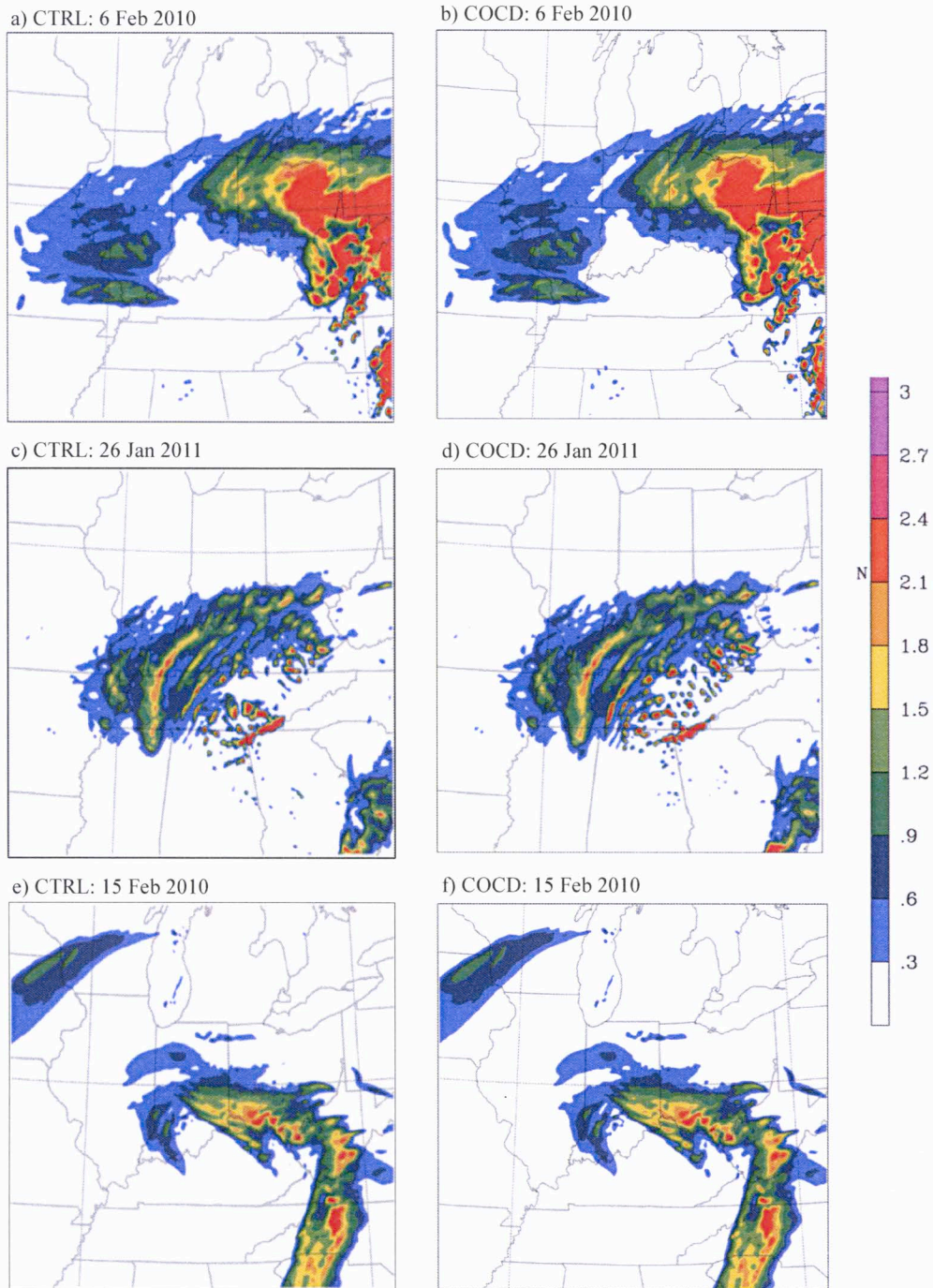


Figure 4.11: Column-integrated precipitation hydrometeors (mm; shaded) at 0300 UTC 6 Feb 2010 for (a) CTRL, and (b) COCD, at 0300 UTC 26 Jan 2011 for (c) CTRL, and (d) COCD, and at 1500 UTC Feb 15 2010 for (e) CTRL, and (f) COCD.

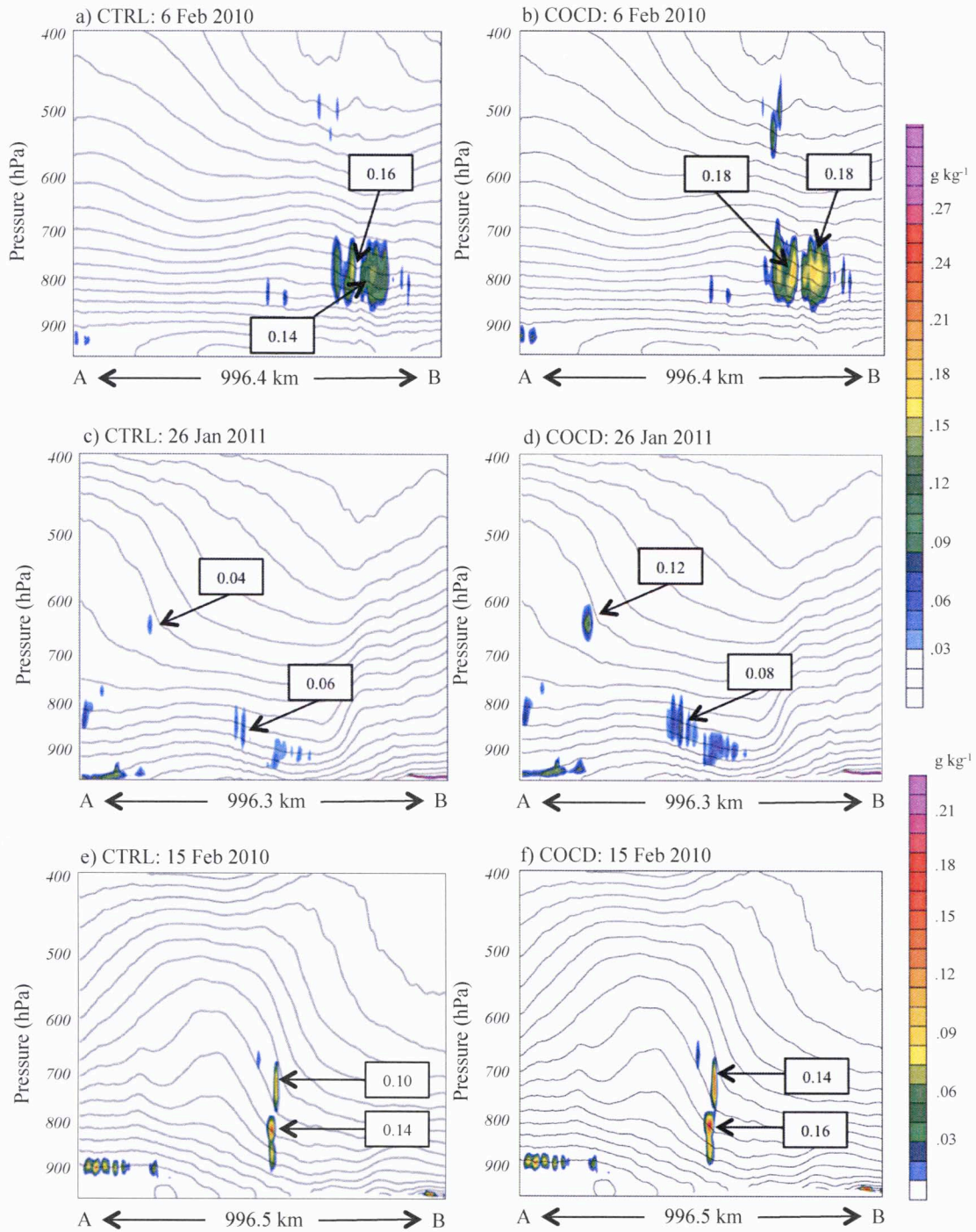
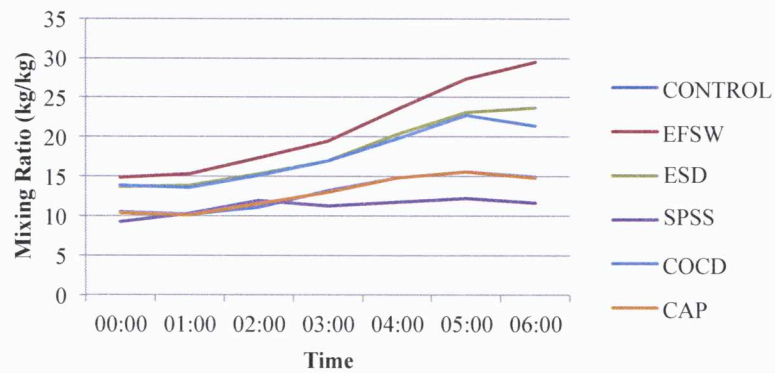
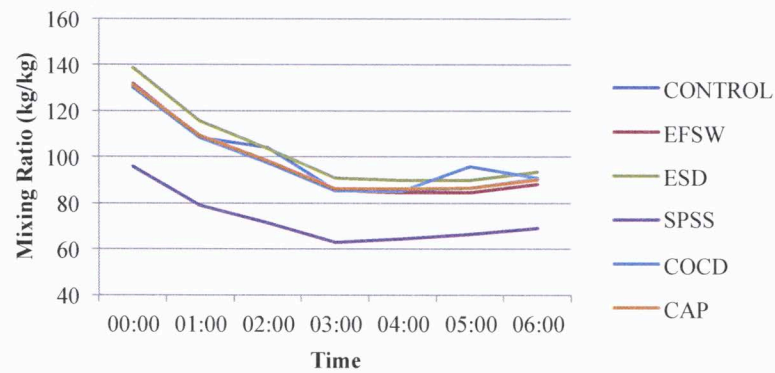


Figure 4.12: COCD vertical cross-sections of θ_e (K; solid) and cloud water mixing ratio (g/kg; shaded) at 0300 UTC 6 Feb 2010 for (a) CTRL, and (b) COCD, at 0300 UTC 26 Jan 2011 for (c) CTRL, and (d) COCD, and at 1500 UTC Feb 15 2010 for (e) CTRL, and (f) COCD.

a) Cloud Water Mixing Ratio (kg/kg)



b) Snow Mixing Ratio (kg/kg)



c) Total Hydrometeor Mixing Ratio (kg/kg)

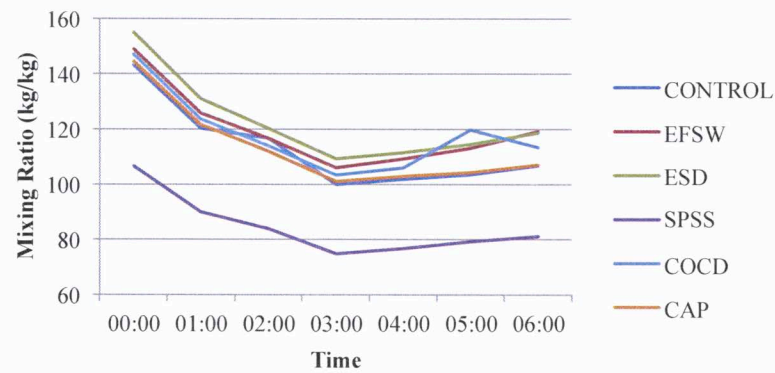
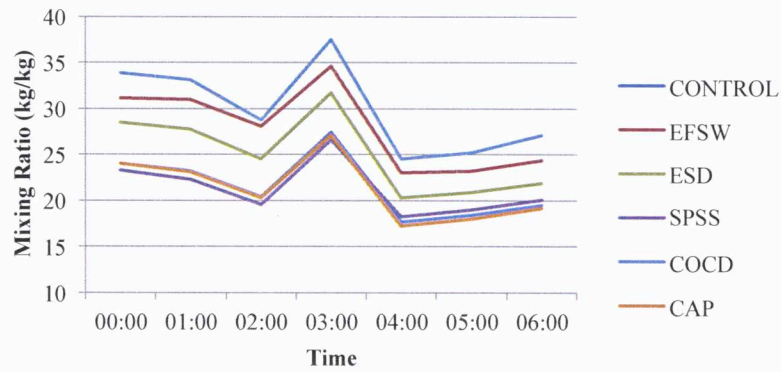
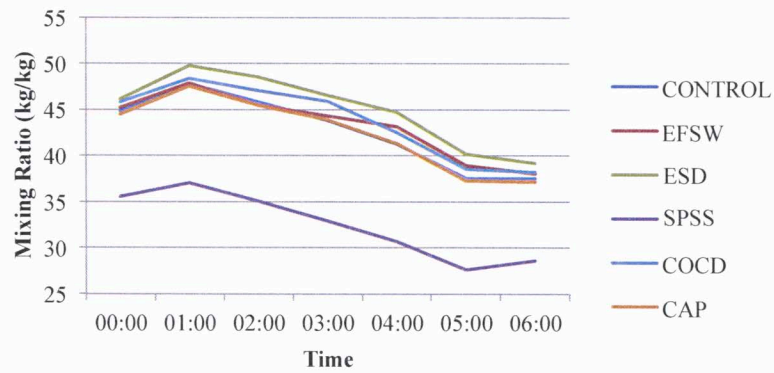


Figure 4.13: Sums of (a) cloud water, (b) snow, and (c) total hydrometeor mixing ratios (kg/kg) in the comma-head region for February 6, 2010 for the times indicated (in UTC).

a) Cloud Water Mixing Ratio (kg/kg)



b) Snow Mixing Ratio (kg/kg)



c) Total Hydrometeor Mixing Ratio (kg/kg)

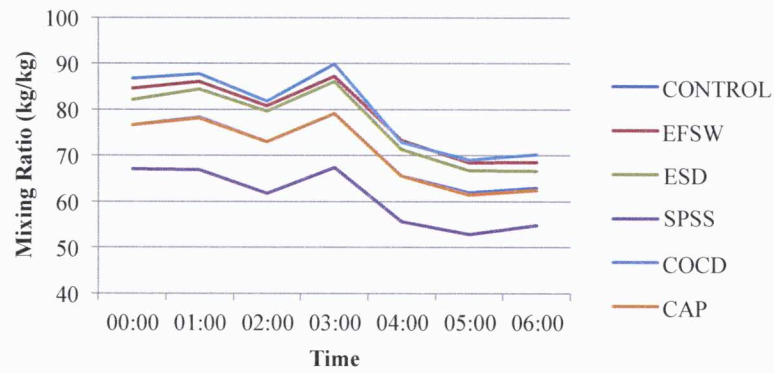
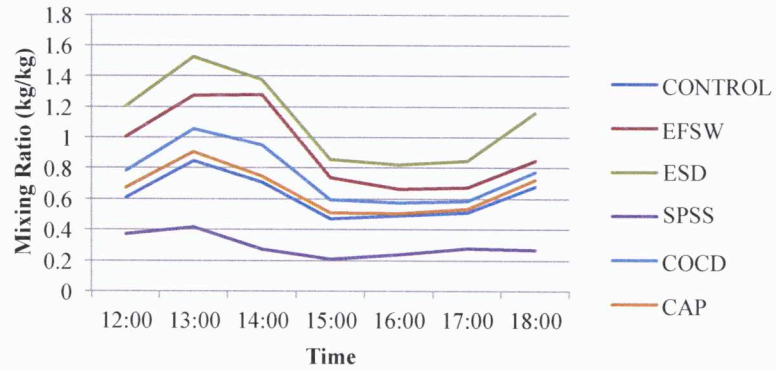
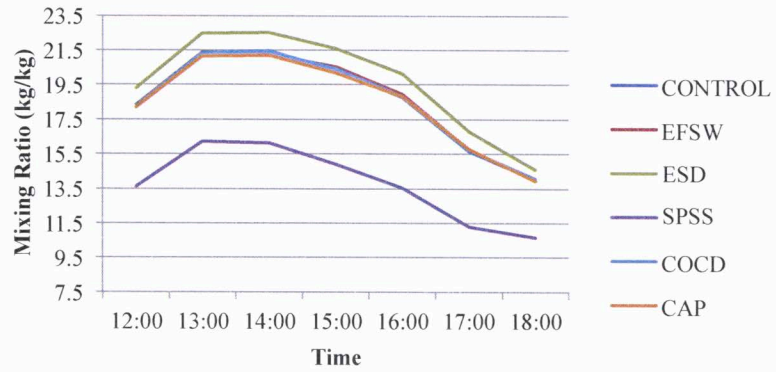


Figure 4.14: Sums of (a) cloud water, (b) snow, and (c) total hydrometeor mixing ratios (kg/kg) in the comma-head region for January 26, 2011 for the times indicated (in UTC).

a) Cloud Water Mixing Ratio (kg/kg)



b) Snow Mixing Ratio (kg/kg)



c) Total Hydrometeor Mixing Ratio (kg/kg)

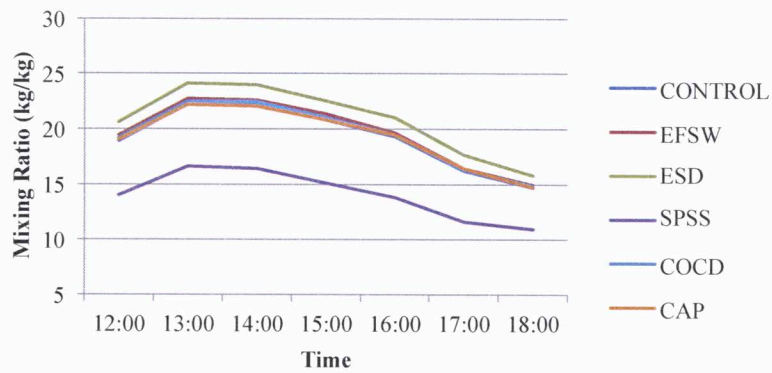


Figure 4.15: Sums of (a) cloud water, (b) snow, and (c) total hydrometeor mixing ratios (kg/kg) in the comma-head region for February 15, 2010 for the times indicated (in UTC).

Bibliography

- Air Weather Service, 1980: "Forecaster's Guide on Aircraft Icing." Air Weather Service Rep. AWS/TR-80/001, 1-52. [Available from U.S. Air Force, Scott AFB, IL 62225.]
- Anthes, R. A., E. Y. Hsie, and Y. H. Kuo, 1987: Description of the Penn State/NCAR Mesoscale Model version 4 (MM4). NCAR Tech. Note, 66 pp.
- Benjamin, S. G., 1989: An isentropic meso- α -scale analysis system and its sensitivity to aircraft and surface observations. *Mon. Wea. Rev.*, **117**, 1586–1603.
- Bennetts, D. A., and B. J. Hoskins, 1979: Conditional symmetric instability – a possible explanation for frontal rainbands. *Quart. J. R. Meteor. Soc.*, **105**, 945-962.
- Bergeron, T., 1935: On the physics of clouds and precipitation. Procès Verbaux de l'Association de Meteorologie, Lisbon, Portugal, International Union of Geodesy and Geophysics, 156–178
- Bernstein, B. C., T. A. Omeron, F. McDonough, and M. Politovich, 1997: The relationship between aircraft icing and synoptic-scale weather conditions. *Wea. Forecasting*, **12**, 742-762.
- , F. McDonough, M. Politovich, and B. G. Brown, 2005: Current icing potential: algorithm description and comparison with aircraft observations. *J. Appl. Meteor.*, **44**, 969-986.
- Berry, E. X., and R. L. Reinhardt, 1974: An analysis of cloud droplet growth by collection. Part II: Single initial distributions. *J. Atmos. Sci.*, **31**, 2127–2135.
- Bjerknes, J., 1932: Exploration de quelques perturbations atmosphériques à l'aide de sondages rapprochés dans le temps (Exploration of some atmospheric disturbances using soundings close in time). *Geophys. Mem.*, **5**(10), 1-12 + 28 pp. of figs.
- Bluestein, H.B., 1993: Synoptic-Dynamic Meteorology in Midlatitudes: Volume II. Oxford University Press, New York, 594pp.
- Bragg, M. B., 1996: Aerodynamics of supercooled large-droplet ice accretions and the effect on aircraft control. *Proceedings of the FAA Inter. Con. Aircraft Inflight Icing*, Springfield, VA, 387-400.
- Brown, B. G., T. L. Fowler, B. C. Bernstein, and G. S. Forbes, 1993: Use of pilot reports for verification of aircraft icing diagnoses and forecasts. Preprints, *Fifth Int. Conf. on Aviation Weather Systems*, Amer. Meteor. Soc., 277–281.

- , 1996: Verification of in-flight icing forecasts: Methods and issues. *Proc., FAA Int. Conf. on In-Flight Aircraft Icing*, Springfield, VA, Department of Transportation, Federal Aviation Administration, 319–330
- , G. Thompson, R. T. Buintjes, R. Bullock, and T. Kane, 1997: Intercomparison of in-flight icing algorithms. Part II: Statistical verification results. *Wea. Forecasting*, **12**, 890-914.
- Browning, K. A., 1990: Organization of clouds and precipitation in extratropical cyclones. *Extratropical Cyclones: The Erik Palmén Memorial Volume*, C. W. Newton and E. O. Holopainen, Eds., *Amer. Meteor. Soc.*, 129-153.
- Carlson, T. N., 1980: Airflow through midlatitude cyclones and the comma cloud pattern. *Mon. Wea. Rev.*, **108**, 1498–1509.
- , 1991: *Mid-Latitude Weather Systems*. Harper-Collins Academic, 507 pp.
- Clark, T. L., 1977: A small-scale dynamic model using a terrain-following coordinate transformation. *J. Comput. Phys.*, **24**, 1986-2014.
- Cole, J., and W. Sand, 1991: Statistical study of aircraft icing accidents. AIAA 91-0558. *29th Aerospace Sciences Meeting*, Reno, Nevada, 1-11.
- Cooper, W. A., and J. D. Marwitz, 1980: Winter storms over the San Juan Mountains. Part III: Seeding potential. *J. Appl. Meteor.*, **19**, 942-949.
- , W. R. Sand, M. K. Politovich, and D. L. Veal, 1984: Effects of icing on performance of research aircraft. *J. Aircraft*, **21**, 708-715.
- Cox, G. P., 1988: Modeling precipitation in frontal rainbands. *Quart. J. Roy. Meteor. Soc.*, **114**, 115–127.
- Czernkovich, N., 2004: Understanding in-flight icing. Tech. Rep., November 2004, *Trans. Canada Avia. Safety Seminar*, 1-21. [Online]. Available: http://aerosafety.ca/sources/aircraft_icing_paper.pdf
- Danielsen, E. F., 1964: Project Springfield Report. DASA Rep. 1517, Defense Atomic Support Agency, 97 pp. [NTIS AD- 607980.]
- Dudhia, J., 1989: Numerical study of convection observed during the winter monsoon experiment using a mesoscale two-dimensional model. *J. Atmos. Sci.*, **46**, 3077–3107.
- Dunn, L., 1987: Cold air damming by the Front Range of the Colorado Rockies and its relationship to locally heavy snows. *Wea. Forecasting*, **2**, 177-189.
- Ek, M., K. E. Mitchell, Y. Lin, E. Rogers, P. Grunmann, V. Koren, G. Gayno, and J. D.

- Tarpley, 2003: Implementation of the Noah land surface model advances in the National Centers for Environmental Prediction operational mesoscale Eta model. *J. Geophys. Res.*, **108**, 8851.
- Ellrod, G. P., and A. A. Bailey, 2007: Assessment of aircraft icing potential and maximum icing altitude from geostationary meteorological satellite data. *Wea. Forecasting*, **22-1**, 160-174.
- Ferrier, B. S., 1994: A double-moment multiple-phase four-class bulk ice scheme: Part I: Description. *J. Atmos. Sci.*, **51-2**, 249-280.
- Field, P. R., R. J. Hogan, P. R. A. Brown, A. J. Illingworth, T. W. Choullarton, and R. J. Cotton, 2005: Parameterization of ice- particle size distributions for mid-latitude stratiform cloud. *Quart. J. Roy. Meteor. Soc.*, **131**, 1997–2017.
- Findeisen, W., 1938: Kolloid-meteorologische vorgänge bei Neiderschlags-Bildung. *Meteor. Z.*, **55**, 121–133.
- Forbes, G. S., Y. Hu, B. G. Brown, B. C. Bernstein, and M. K. Politovich, 1993: Examination of conditions in the proximity of pilot reports of icing during STORM-FEST. Preprints, *Fifth Int. Conf. on Aviation Weather Systems*, Vienna, VA, *Amer. Meteor. Soc.*, 282–286.
- Gilbert GK. 1884. Finley's tornado predictions. *Amer. Meteor. J.*, **1**, 166–172.
- Golding, B., 1984: A study of the structure of mid-latitude depressions in numerical model using trajectory techniques. I: Development of ideal baroclinic waves in dry and moist atmosphere. *Quart. J. R. Meteor. Soc.*, **110**, 847-879.
- Green, S., 1997: Icing problem is a serious threat for which the best solutions are years away. *ICAO Journal*, Jan./Feb. 1997, 5-26.
- Grooters, A. T. F., J. J. Strickland, and N. T. Diallo, 2003: Aircraft Meteorological Data Relay (AMDAR) Reference Manual. WMO-No. 958. Secretariat of the World Meteorological Organization, Geneva, Switzerland, 2003.
- Guan, H., S. G. Cober, and G. A. Isaac, 2001: Verification of supercooled cloud water forecasts with in situ aircraft measurements. *Wea. Forecasting*, **16**, 145-155.
- Hansman, J., 1989: The influence of ice accretion physics on the forecasting of aircraft icing conditions. Preprint, 3rd Intl. Conf. Aviation Wea. Sys., Anaheim, CA, *Amer. Meteor. Soc.*, 154-158.
- Hanssen, A.W. and W. J. A. Kuipers, 1965: On the relationship between frequency of rain and various meteorological parameters. *Meded. Vierh.*, **81**, 2-15.

- Harold, T. W., 1973: Mechanisms influencing the distribution of precipitation within baroclinic disturbances. *Quart. J. Roy. Meteor. Soc.*, **99**, 232–251.
- Heidke, P., (1926). Berechnung der erfolges und der gute der windstarkevorhersagen im sturmwarnungsdienst. *Geogr. Ann.*, **8**, 301-349.
- Heymsfield, A. J., and J. L. Parrish, 1978: A computational technique for increasing the effective sampling volume of the PMS two-dimensional particle size spectrometer. *J. Appl. Meteor.*, **17-10**, 1566-1572.
- Hobbs, P. V., 1975: The nature of winter clouds and precipitation in the Cascade Mountains and their modification by artificial seeding. Part I: Natural conditions. *J. Appl. Meteor.*, **14**, 783–804.
- , and A. L. Rangno, 1985: Ice particle concentrations in clouds. *J. Atmos. Sci.*, **23**, 2523-2355.
- Hoskins, B. J., 1974: The role of potential vorticity in symmetric stability and instability. *Quart. J. Roy. Meteor. Soc.*, **100**, 480–482.
- Iskenderian, H., 1988: Three-dimensional airflow and precipitation structures in a nondeepening cyclone. *Wea. Forecasting*, **3**, 18–32.
- Janjić, Z. I., 2002: Nonsingular implementation of the Mellor - Yamada level 2.5 scheme in the NCEP Meso Model. NCEP Office Note 437, 61 pp.
- , T. L. Black, M. E. Pyle, H.-Y. Chuang, E. Rogers, and G. J. DiMego, 2005: The NCEP WRF-NMM core. Preprints, 2005 WRF/MM5 User's Workshop, Boulder, CO, National Center for Atmospheric Research, 2.9. [Available online at <http://www.mmm.ucar.edu/wrf/users/workshops/WS2005/presentations/session2/9-Janjic.pdf>.]
- Kelsch, M., and L. Wharton, 1996: Comparing PIREPS with NAWAU turbulence and icing forecasts: issues and results. *Wea. Forecasting*, **11**, 385-390.
- Korolev, A., 2006: Limitations of the Wegener–Bergeron–Findeisen mechanism in the evolution of mixed-phase clouds. *J. Atmos. Sci.*, **64**, 3372-3375.
- Larson, V. E., and A. J. Smith, 2009: An analytic scaling law for depositional growth of snow in thin mixed-phase layer clouds. *J. Atmos. Sci.*, **66**, 2620-2639.
- Lewis, W., 1947: A flight investigation of the meteorological conditions conducive to the formation of ice on airplanes, NACA Tech Note 1393, 50 pp.
- , 1951: Meteorological aspects of aircraft icing. *Compendium of Meteorology*, T. F. Malone, Ed, *Amer. Meteor. Soc.*, 1197-1203.
- Lillo, S. P., and E. R. Mansell, 2010: Sensitivity of microphysical parameters on the evolution of a supercell. *11th Annual AMS Student Conference*, Austin, TX, Amer.

- Meteor. Soc., S152.
- Mansell, E. R., C. L. Ziegler, and E. C. Bruning, 2010: Simulated electrification of a small thunderstorm with two-moment bulk microphysics. *J. Atmos. Sci.*, **67**, 171-194.
- Martin, G. M., D. W. Johnson, and A. Spice, 1994: The measurement and parameterization of effective radius of droplets in warm stratocumulus clouds. *J. Atmos. Sci.*, **51**, 1823–1842.
- Martin J. E., 1998: The structure and evolution of a continental winter cyclone. Part II: Frontal forcing of an extreme snow event. *Mon. Wea. Rev.*, **126**, 329 – 348.
- , 1999: Quasigeostrophic forcing of ascent in the occluded sector of cyclones and the trowal airstream. *Mon. Wea. Rev.*, **127**, 70-88.
- Matrosov, S. Y., 1992: Radar reflectivity in snowfall. *IEEE: Transactions on Geoscience and Remote Sensing*, **30**, 454-461.
- McDonough, F., B.C. Bernstein, and M.K. Politovich, 2003: The forecast icing potential (FIP) technical description. *Report to the FAA Aviation Weather Technology Transfer Board*. 30 pp.
- , and C.A. Wolff, 2004: The forecast icing potential (FIP) algorithm. Preprints, *20th International Conference on Interactive Information and Processing Systems (IIPS) for Meteorology, Oceanography, and Hydrology*. Available from the American Meteorological Society.
- Milbrandt, J. A., and M. K. Yau, 2005: A multimoment bulk microphysics parameterization. Part I: Analysis of the role of the spectral shape parameter. *J. Atmos. Sci.*, **62**, 3051–3064.
- Milbrandt, J. A., M. K. Yau, J. Mailhot, S. Belair, and R. McTaggart-Cowan, 2010: Simulation of an orographic precipitation event during IMPROVE-2. Part II: Sensitivity to the number of moments in the bulk microphysics scheme. *Mon. Wea. Rev.*, **138**, 625-642.
- Miles, N. J. Verlinde, and E. Clothiaux, 2000: Cloud droplet size distributions in low-level stratiform clouds. *J. Atmos. Sci.*, **57**, 295-311.
- Mitchell, D. L., and A. J. Heymsfield, 2005: Refinements in the treatment of ice particle terminal velocities, highlighting aggregates. *J. Atmos. Sci.*, **62**, 1637–1644.
- Mlawer, E. J., S. J. Taubman, P. D. Brown, M. J. Iacono, and S. A. Clough, 1997: Radiative transfer for inhomogeneous atmosphere: RRTM, a validated correlated-k model for the longwave. *J. Geophys. Res.*, **102 (D14)**, 16663–16682.
- Modica, G. D., S. T. Heckman, and R. M. Rasmussen, 1994: An application of an explicit microphysics mesoscale model to a regional icing event. *Quart. J. R. Meteor.*

Soc., **33**, 53-64.

Molthan, A. L., B. A. Colle, 2012: Comparisons of single- and double-moment microphysics schemes in the simulation of a synoptic-scale snowfall event. *Mon. Wea. Rev.*, **140**, 2982-3001.

Moore, J. T., C. E. Graves, S. Ng, and J. L. Smith, 2004: A process-oriented methodology toward understanding the organization of an extensive mesoscale snowband: A diagnostic case study of 4-5 December 1999. *Wea. Forecasting*, **20**, 35-50.

Morrison, H., and J. O. Pinto, 2006: Intercomparison of bulk microphysics schemes in mesoscale simulations of springtime Arctic mixed-phase stratiform clouds. *Mon. Wea. Rev.*, **134**, 1880–1900.

———, and W. W. Grabowski, 2008: A novel approach for representing ice microphysics in models: description and tests using a kinematic framework. *J. Atmos. Sci.*, **65**, 1528-1548.

———, and ———, 2010: An improved representation of rimes snow and conversion to graupel in a multicomponent bin microphysics scheme. *J. Atmos. Sci.*, **67**, 1337-1360.

Namias, J., 1939: The use of isentropic analysis in short term forecasting. *J. Aeronaut. Sci.*, **6**, 295-298.

Nicosia, D. J., and R. H. Grumm, 1999: Mesoscale band formation in three major northeastern United States snowstorms. *Wea. Forecasting*, **14**, 346–368.

Novak, D., B. A. Colle, and A. R. Aiyyer, 2010: Evolution of mesoscale precipitation band environments within the comma head of northeast U.S. cyclones. *Mon. Wea. Rev.*, **138**, 2354-2374.

Nygaard, B. E. K., J. E. Kristjánsson, and L. Makkonen, 2011: Prediction of in-cloud icing conditions at ground level using the WRF model. *J. Appl. Meteor. Climatol.*, **50**, 2445-2459.

Petty, K. R., and C. D. J. Floyd, 2004: A statistical review of aviation airframe icing accidents in the U.S. Preprints, *11th Conf. on Aviation, Range and Aerospace*, Hyannis, MA, Amer. Meteor. Soc., 11.2.

Politovich, M., 1988: Aircraft icing caused by large supercooled droplets. *J. Appl. Meteor.*, **28**, 856-868.

———, 2000: Predicting glaze of rime ice growth on airfoils. *J. Aircraft*, **37**, 116-121.

———, 2003: Aircraft Icing. Elsevier Science Ltd., 68-75.

———, 2003: Predicting in-flight aircraft icing intensity. *J. Aircraft*, **40**, 639-644.

- Pruppacher, H. R., and J. D. Klett, 1997: *Microphysics of Clouds and Precipitation*. D. Reidel, 714 pp.
- Rasmussen, R., M. Politovich, J. Marwitz, W. Sand, J. McGinley, J. Smart, R. Pielke, S. Rutledge, D. Wesley, G. Stossmeister, B. Bernstein, K. Elmore, N. Powell, E. Westwater, B. B. Stankov, and D. Burrows, 1992: Winter Icing and Storms Project (WISP). *Bull. Amer. Meteor. Soc.*, **73-7**, 951-974.
- Rauber, R. M., and A. Tokay, 1991: An explanation for the existence of supercooled water at the top of cold clouds. *J. Atmos. Sci.*, **48**, 1005–1023.
- Reeves, H. D., and D. T. Dawson II, 2013: The dependence of QPF on the choice of microphysical parameterization for lake-effect snowstorms. *J. Appl. Meteor. Climatol.*, **52**, 363-377.
- Reisner, J., R. M. Rasmussen, and R. T. Bruintjes, 1998: Explicit forecasting of supercooled liquid water in winter storms using the MM5 mesoscale model. *Quart. J. R. Meteor. Soc.*, **124**, 1071-1107.
- Rogers, R. R., and M. K. Yau., 1996: *A Short Course in Cloud Physics*. Butterworth-Heinemann Publications, 290 pp.
- Rogers, E., T. Black, B. Ferrier, Y. Lin, D. Parrish, and D. GiMego, 2001: Changes to the NCEP Meso Eta Analysis and Forecast System: Increase in resolution, new cloud microphysics, modified precipitation assimilation, modified 3DVAR analysis. *NWS Tech. Procedures Bull.*, **488**, 15pp.
- Rosenfeld, D., and I. M. Lensky, 1998: Satellite-based insights into precipitation formation processes in continental and maritime convective clouds. *Bull. Amer. Meteor. Soc.*, **79**, 2457–2476.
- Ryzhkov, A. V., D. S. Zrnić, and B. Gordon, 1998: Polarimetric method for ice water content determination. *J. Appl. Meteor.*, **37**, 125– 134.
- , and ———, 2007: Depolarization in ice crystals and its effect on radar polarimetric measurements. *J. Atmos. Ocean. Tech.*, **24**, 1256-1267.
- Sand, W. R., 1985: Aircraft icing conditions- “Normal and unusual.” *19th Annual Air Law Symposium*, Dallas, *J. Air Law and Commerce*, 3-17.
- Schultz P., and M. Politovich, 1992: Toward the improvement of aircraft-icing forecasts for the continental United States. *Wea. Forecasting*, **7**, 491-500.
- Schultz, D. M., and P. N. Schumacher, 1999: The Use and Misuse of Conditional Symmetric Instability. *Amer. Meteor. Soc.*, **127**, 2709-2729.

- , and J. A. Knox, 2007: Banded convection caused by frontogenesis in a conditionally, symmetrically, and inertially unstable environment. *Mon. Wea. Rev.*, **135**, 2095-2109.
- , and G. Vaughan, 2011: Occluded fronts and the occlusion process. *Bull. Amer. Meteor. Soc.*, 443-460.
- Schumacher, R. S., D. M. Schultz, and J. A. Knox, 2010: Convective snowbands downstream of the Rocky Mountains in an environment with conditional, dry-symmetric, and inertial instabilities. *Mon. Wea. Rev.*, **138**, 4416-4438.
- Seifert, A., and K. D. Beheng, 2006: A two-moment cloud microphysics parameterization for mixed-phase clouds. Part 1: Model description. *Meteor. Atmos. Phys.*, **92**, 45-66.
- Sienkiewicz, J. M., J. D. Locatelli, P. V. Hobbs, and B. Geerts, 1989: Organization and structure of clouds and precipitation on the mid-Atlantic coast of the United States. Part II: The mesoscale and microscale structures of some frontal rain-bands. *J. Atmos. Sci.*, **46**, 1349-1364.
- Skamarock, W. C., J. B. Klemp, J. Dudhia, D. O. Gill, D. M. Barker, M. G. Duda, X. Huang, W. Wang, and J. G. Powers, 2008: A description of the Advanced Research WRF Version 3, NCAR Tech. Note NCAR/ TN-475+STR, 125 pp.
- Smith, W. L. Jr., P. Minnis, and D. F. Young, 2000: An icing product derived from operational satellite data. *AMS 9th Conference on Aviation, Range, and Aerospace Meteorology*, Orlando, FL, 256-259.
- , P. Minnis, C. Fleeger, D. Spangenberg, R. Palikonda, and L. Nguyen, 2012: Determining the flight icing threat to aircraft with single-layer cloud parameters derived from operational satellite data. *J. Appl. Meteor. Climatol.*, **51-10**, 1794-1810.
- Solomon, A., M. D. Shupe, P. O. Persson, and H. Morrison, 2011: Moisture and dynamical interactions maintaining a decoupled Arctic mixed-phase stratocumulus in the presence of a humidity inversion. *Atmos. Chem. Phys.*, **11**, 10127-10148.
- Srivastava, R. C., and J. L. Coen, 1992: New explicit equations for the accurate calculation of the growth and evaporation of hydrometeors by the diffusion of water vapor. *J. Atmos. Sci.*, **49**, 1643-1651.
- Stark, D., B. A. Colle, and S. E. Yuter, 2013: Observed microphysical evolution for two east coast winter storms and the associated snow bands. *Mon. Wea. Rev.*, **141**, 2037-2057.
- Stoelinga, M. T., J. D. Locatelli, and C. P. Woods, 2007: The occurrence of “irregular” ice particles in stratiform clouds. *J. Atmos. Sci.*, **64**, 2740-2750.

- Tafferner, A., T. Hauf, C. Leiffield, T. Hafner, H. Leykauf, and U. Voight, 2003: ADWICE: Advanced Diagnosis and Warning System for Aircraft Icing Environments. *Wea. Forecasting*, **18**, 184-203.
- Thompson, G., R. M. Rasmussen, and K. Manning, 2004: Explicit forecasts of winter precipitation using an improved bulk microphysics scheme. Part I: Description and sensitivity analysis. *Mon. Wea. Rev.*, **132**, 519-542.
- , P. R. Field, R. M. Rasmussen, and W. D. Hall, 2008: Explicit forecasts of winter precipitation using an improved bulk microphysics scheme. Part II: Implementation of a new snow parameterization. *Mon. Wea. Rev.*, **136**, 5095-5115.
- Thompson, J.K.: "1954 Icing Presentation for Major Commands," WADC Tech, Note WCT 55-26, WADC April 1955 (AD-69347)
- Tremblay, A., S. G. Cober, A. Glazer, and G. Isaac, 1996: An intercomparison of mesoscale forecasts of aircraft icing using SSM/I retrievals. *Wea. Forecasting*, **11**, 66-77.
- Tripoli, G. J., and W. R. Cotton, 1982: The CSU three-dimensional cloud/mesoscale model-1982. Part I: General theoretical framework and sensitivity experiments. *J. de Rech. Atmos.*, **16**, 185-220.
- Uijlenhoet, R., M. Steiner, and J. A. Smith, 2003: Variability of raindrop size distributions in a squall line and implications for radar rainfall estimation. *J. Hydrometeor.*, **4**, 43-61.
- Vaillancourt, P. A., A. Tremblay, S. G. Cober, and G. A. Isaac, 2003: Comparison of aircraft observations with mixed-phase cloud simulations. *Mon. Wea. Rev.*, **131**, 656-671.
- Vasiloff, S. V., and Coauthors, 2007: Improving QPE and very short term QPF: An initiative for a community-wide integrated approach. *Bull. Amer. Meteor. Soc.*, **88**, 1899-1911.
- Vivekanandan, J., B. Martner, M. K. Politovich, and G. Zhang, 1999a: Retrieval of atmospheric liquid and ice characteristics using dual-wave-length radar observations. *IEEE Trans. Geosci. Remote Sens.*, **37**, 2325-2334.
- , G. Zhang, and M. K. Politovich, 2001: An assessment of droplet size and liquid water content derived from dual-wavelength radar measurements to the application of aircraft icing detection. *J. Atmos. Oceanic Tech.*, **18**, 1787-1798.
- Walko, R. L., W. R. Cotton, M. P. Meyers, and J. Y. Harrington, 1995: New RAMS cloud microphysics parameterization. Part I: The single-moment scheme. *Atmos. Res.*, **38**, 29-62.
- Wang, P. K., and W. Ji, 2000: Collision efficiencies of ice crystals at low-intermediate

Reynolds numbers colliding with supercooled cloud droplets: A numerical study. *J. Atmos. Sci.*, **57**, 1001–1009.

Wegener, A., 1911: *Thermodynamik der Atmosphäre*. J. A. Barth Verlag, 311 pp.